Ultracold Atom-Ion Systems in Hybrid Traps

DISSERTATION

zur Erlangung des akademischen Grades
doctor rerum naturalium
(Dr. rer. nat.)
im Fach Physik

eingereicht an der
Mathematisch-Naturwissenschaftlichen Fakultät
der Humboldt-Universität zu Berlin

von

M.Sc.-Phys. Onyango Stephen Okeyo

Präsident der Humboldt-Universität zu Berlin:
Prof. Dr.-Ing. Dr. Sabine Kunst

Dekan der Mathematisch-Naturwissenschaftlichen Fakultät:
Prof. Dr. Elmar Kulke

Gutachter/innen:	1. Prof. Dr. Alejandro Saenz 2. Prof. Dr. Kurt Busch 3. Dr. hab. Zbigniew Idziaszek
Tag der mündlichen Prüfung:	29.09.2017

Abstract

This thesis deals with the theoretical description of a hybrid system of an ultracold neutral atom and a single ion. These hybrid atom-ion systems have attracted significant interest in recent years. They combine the key advantages of ultracold neutral atoms and ions. In particular, neutral atoms are easily scalable and can be prepared in large numbers, while trapped ions can be stored for much longer times and are easy to control. Some of the proposed prospects of the hybrid quantum systems include sympathetic cooling of trapped ions, ultracold chemistry, quantum information processing, and atom-ion quantum simulators. These applications require extremely precise control and thus very accurate theoretical modeling. A new method that allows for a full six-dimensional treatment of two particles in spatially separated three-dimensional trapping potentials was developed. By allowing for the spatial displacement between the trapping potentials, it is possible to describe the controlled motion of a single ion through an optical-lattice potential filled with neutral atoms. The interaction between the neutral atom and the ion is modeled using realistic Born-Oppenheimer potential curves from *ab initio* quantum chemistry calculations. An application of the developed approach to the hybrid atom-ion system of $^7\mathrm{Li}_2^+$ isotope reveals avoided crossings between the molecular bound states and the unbound trap states as a function of the separation between the two traps. These avoided crossings correspond to trap-induced resonances. This finding confirms the trap-induced resonances predicted earlier based on quantum-defect-theory calculations. Also, the recently found inelastic confinement-induced resonances in ultracold neutral atoms are demonstrated to be present in atom-ion systems. These resonances arise due to the coupling between the center-of-mass and relative motions. The inelastic confinement-induced resonances could be used in coherent molecular ion formation and in the determination of atom-ion scattering properties like the scattering lengths.

Zusammenfassung

Diese Arbeit beschäftigt sich mit der theoretischen Beschreibung eines Hybridsystems eines ultrakalten neutralen Atoms und eines einzelnen Ions. Diese Hybrid-Atom-Ion-Systeme haben in den letzten Jahren großes Interesse geweckt. Sie verbinden die wichtigsten Vorteile von ultrakalten neutralen Atomen und Ionen. Neutrale Atome sind leicht skalierbar vor allem und können in großen Stückzahlen vorbereitet werden, während gefangene Ionen über längere Zeiten gelagert werden können und leicht kontrollierbar sind. Einige der vorgeschlagenen Aussichten der hybriden Quantensysteme umfassen die sympathische Kühlung von eingefangenen Ionen, die ultrakalte Chemie, das Quantum Informationsverarbeitung, und Atom-Ionen-Quantensimulatoren. Diese Anwendungen erfordern eine äußerst präzise Steuerung und damit eine sehr genaue theoretische Modellierung. Eine neue Methode, die eine vollständige sechsdimensionale Behandlung von zwei Partikeln ermöglicht In räumlich getrennten dreidimensionalen Fangpotentialen wurde entwickelt. Indem man die räumliche Verschiebung zwischen den Einfangpotentialen erlaubt, ist es möglich, die gesteuerte Bewegung eines einzelnen Ions durch ein optisches Gitterpotential zu beschreiben, das mit neutralen Atomen gefüllt ist. Die Wechselwirkung zwischen dem neutralen Atom und dem geladenen Ion wird durch eine realistische Born-Oppenheimer Potentialkurve beschrieben, die aus ab initio Berechnungen der Quantenchemie stammt. Durch die räumliche Verschiebung der Fallenpotentiale kann die kontrollierte Bewegung eines einzelnen Ions durch ein optische Gitter mit ultrakalten Atomen beschrieben werden. Eines der hier diskutierten Hybridsysteme ist ${}^7\mathrm{Li}_2^+$ Isotop, das mit der neu entwickelten Methode untersucht wird, dabei wurden vermiedene Kreuzungen im Energiespektrum zwischen molekularen Zuständen und den Schwingungszuständen des Fallenpotentials als Funktion des Abstandes zwischen den beide Fallen beobachtet. Diese vermiedenen Kreuzungen bestätigen die bereits vorhergesagten falleninduzierten Resonanzen, die mithilfe der Quantendefekttheorie bestimmt wurden. Ebenfalls werden die erst kürzlich entdeckten inelastischen falleninduzierten Resonanzen in ultrakalten Atomen auch in den Atom-Ion Systemen beobachtet. Diese Resonanzen entstehen durch die Kopplung der Relativ- und Schwerpunktsbewegung. Zudem sind sie von allgemeiner Natur und wurden auch in langreichweitiger wechselwirkenden System wie z.B dipolaren Systemen und Coulomb wechselwirkenden Systemen beobachtet. Die inelastischen falleninduzierten Resonanzen können benutzt werden um kohärent Molekulionen zu bilden und zur Bestimmung des Atom-Ion Streuverhaltens.

Dedicated

To the loving memory of my brother
Okoth Robert.

Contents

Chapter 1

Introduction

The experimental realization of a Bose-Einstein condensate (BEC)[1] in dilute alkali atomic gases [1, 2] and the observation of a Fermi-degenerate quantum gas of ^{40}K atoms [3] have been some of the key moments in the field of atomic and molecular physics. One of the interesting features of these ultracold samples is the ability to precisely manipulate them. The interactions between alkali-metal (one valence electron) atoms can be controlled via magnetic Feshbach resonances [4], and recently, an orbital Feshbach resonance [5] has been used to manipulate the interaction between atoms with two valence electrons [6, 7]. Another experimental milestone was the loading of ultracold neutral atomic gases into an optical lattice (OL) [8, 9]. An OL is an artificial defect-free crystal of light formed by superimposed counterpropagating laser beams [10]. Unlike real solids, the parameters of an OL are easily tunable via variations of the laser intensities or the wavelengths. Recently, magnetically assisted Sisyphus laser cooling, first proposed by Claude Cohen-Tannoudji[2], was used to cool strontium monohydroxid (SrOH) [11] paving the way towards the study of ultracold polyatomic molecules. Also, hundreds of neutral ^{133}Cs atoms, have been simultaneously cooled using the so-called cavity cooling [12]. The advancements in cooling of molecules could be essential in bringing them (molecules) to the same level of control like in atoms, offering a wide range of fundamental experiments and applications in quantum computing. The ability to precisely control the internal states, the external confinements, and the interatomic interactions of these ultracold atomic samples makes them ideal candidates for simulating and testing condensed matter theory models and many-body physics [13–16]. The excellent coherence properties of ultracold neutral atoms have found topical applications ranging from high precision atomic clocks [17, 18], quantum information processing [19–22], quantum simulation [23–25], precision measurements [26, 27], to gravitational sensors [28].

In parallel to the advancements of ultracold neutral atoms, trapped and laser-cooled ions [29, 30] have also experienced spectacular developments. Trapped ions provide an excellent controlled single-particle quantum system[3]. The individual addressability and longer storage times have placed cold ions at the forefront of quantum computation [31, 32], quantum simulation [33–35],

---

[1] Nobel Prize in Physics in 2001

[2] Nobel Prize in Physics in 1997

[3] Nobel Prize in Physics in 2012

and currently, the most accurate clock in the world is based on the optical frequency transitions of a single trapped $^{171}\mathrm{Yb}^+$ [36].

Even though trapped ions can be accurately controlled and manipulated, scaling them to large numbers remains a challenge [37, 38]. However, since trapped ultracold neutral atoms and ions have complementary experimental advantages, they can be combined together in to hybrid setups. Such a hybrid atom-ion system would then exploit the advantages of the two distinct systems while circumventing the limitations of each individual setup. For example, while cold ions offer longer decoherence [31] and storage times, faster gate speeds, and are easy to address and manipulate individually due to the strong Coulomb interactions, the neutral atoms on the other hand are more scalable and can be prepared in large numbers.

Since the inception of hybrid mixture of ultracold neutral atoms and ions [39–41], and the introduction of hybrid traps [42, 43], the field of simultaneously trapped ultracold neutral atoms and laser-cooled ions in hybrid traps (see Figure 1.1) has sparked much interest until recent times [44, 45] due to the aforementioned complementary properties. Theoretical studies of hybrid atom-ion systems have shown magnetic Feshbach resonances [46] and shape resonances [47]. Initial prospect to use ultracold neutral atoms to serve as a refrigerator for the sympathetic cooling of the ions [42, 48] has been realized experimentally [49–52]. Further prospects include, among others, a hybrid atom-ion quantum simulator for emulating solid-state physics [53, 54], quantum computation [55, 56], scanning-tunneling microscope for investigating local properties of ultracold atomic clouds [57, 58], and the formation of molecular ions [59], for example by radiative association of cold trapped atoms and ions [47], are relevant to astrophysics [60] and ultracold chemistry.

Despite all these prospective applications of the ultracold neutral atom and ion mixture, there are still experimental and theoretical challenges to be addressed. Experimentally, other than the difficulties in integrating the traps for the neutral atom and the ion, the micromotion of the ion in the commonly used radiofrequency (rf) Paul traps remains a big challenge. Suggestions to minimize and, or circumvent micromotion have included using linear Paul traps with longitudinal electrostatic confinement [62], or by compensating the spurious field effects using extra electrodes that generate direct-current electric fields [63], and optical trapping of the ions [64–68]. Another option put forward to reduce the effects of micromotion is to use a combination of an ion-atom pair with large mass ratio [55, 69, 70], however, a recent experiment with atom-ion species of $^{87}\mathrm{Rb}$ and $^{88}\mathrm{Sr}^+$ which have nearly equal masses [71] found that the atom-ion energy scale is determined by the force that the atom exerts on the ion as they collide and not the temperature of the ultracold atoms or micromotion. The other roadblock facing these atom-ion systems in the current experiments is the difficulty in accessing the s-wave scattering regime. This is due to the

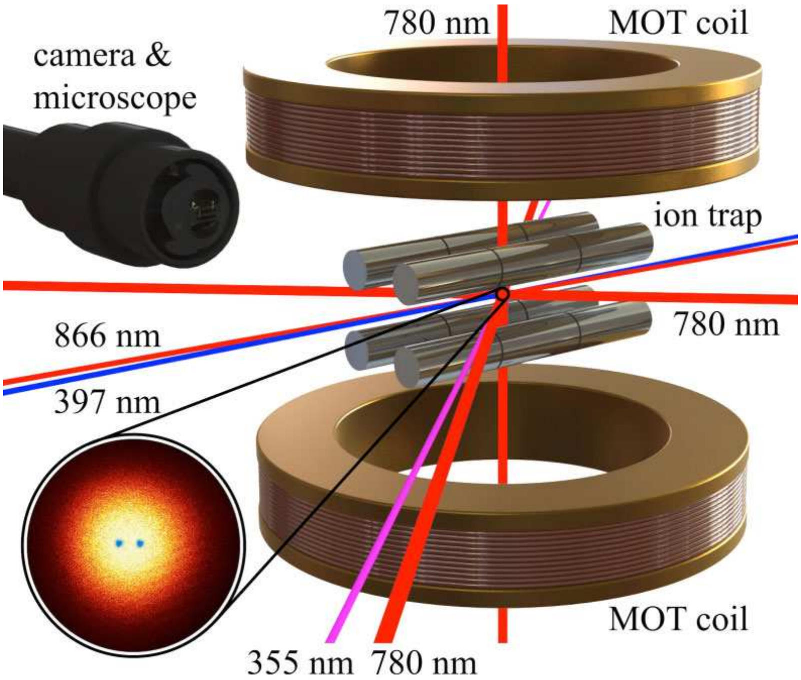

Figure 1.1: Schematic of a hybrid atom-ion trap apparatus. The setup is made of a magnetic-optical trap (MOT) that is concentric with a linear radiofrequency (rf) ion trap. The insert shows two laser-cooled $^{40}\mathrm{Ca}^{+}$ ions (blue) in a cloud of ultracold Rb atoms (red-yellow). Figure taken from [61].

high energies that arise from the long-range nature of their interactions and the large elastic cross sections [39]. It therefore means that all the application prospects that would rely on tuning the atom-ion s-wave scattering length are currently still out of reach.

The difficulty in the theoretical treatment arises from the fact that the long-range nature of atom-ion polarization potential that scales asymptotically as $1/r^4$, is comparable to or larger than the typical trap lengths, preventing the use of δ-function pseudopotential [72] to model the interaction potential like in the case of the ultracold neutral atoms. Also, the trapping frequencies for the atom and the ion are typically quite different with the atom-trap frequencies being in the order of hundreds of kHz while the ion traps are in the MHz range. This difference in the frequency leads to a coupling between the relative (rel.) and center-of-mass (c.m.) motions even within the harmonic approximation of the trap potentials complicating the theoretical description.

This thesis aims to provide an exact numerical approach for describing the interaction between a trapped ultracold neutral atom and a single laser-cooled ion. The attractive feature of the approach is that the interaction between the two particles is treated in a realistic fashion using Born-Oppenheimer potential curves. The trap potentials are modeled from the periodic form of the OL. The employed approach allows for the treatment of the trapping potentials for the atom and the ion within and beyond the harmonic approximation while taking into account the coupling between the center-of-mass and the relative motions degree of freedom by means of configuration interaction. Also provided in this thesis is a method for treating two interacting particles trapped in spatially separated potentials. The numerical procedure used in the present case extends the model developed earlier in [73] to study two ultracold neutral atoms confined in spatially separated three-dimensional optical traps and interacting via central interatomic interaction potentials.

The remainder of this thesis is organized as follows:

- Chapter 2 reviews the theoretical concepts essential for the understanding of low-energy collisions.
- Chapter 3 contains the review of the method originally reported in [73] together with the descriptions of the programs used in the numerical calculations.
- Chapter 4 contains the extension of the original method to incorporate the spatial separation between the trap potentials. This is one of the key achievements of the thesis.
- Chapter 5 is devoted to the construction of the *ab initio* atom-ion potential curves and the procedure for manipulating the atom-ion interactions.
- Chapter 6 provides the theoretical description of an atom-ion system confined in spatially separated quasi 1D- and 3D- harmonic traps and interacting via realistic central potential. The analysis of the energy spectrum as a function of the separation distance between the traps of the neutral atom and the single ion reveals the expected trap-induced shape resonances. The findings are in agreement with earlier theoretical studies based on the quantum defect theory and is part of the main results of the study.
- Chapter 7 contains the other result showing that the so-called inelastic confinement-induced resonances are present in atom-ion systems. This type of resonance occurs whenever the center-of-mass and relative motions are coupled. They had been predicted to occur in ultracold neutral atoms and also confirmed experimentally. Finding them in atom-ion systems further confirms the universality of these type of resonances which have also been predicted in dipolar quantum gases and Coulomb interacting systems. The coupling of the center-of-mass and relative motions is achieved by considering both harmonic and anharmonic trapping potentials.
- Chapter 8 provides the summary of the thesis findings and an outlook.

Chapter 2

Theoretical Background

In this chapter, a brief review of the basic theoretical background essential for the understanding of low-energy collisions is presented. The chapter begins with a description of adiabatic and Born-Oppenheimer (BO) approximations. In section 2.2, optical lattice (OL) trapping potentials are discussed. The basic scattering theory is given in section 2.3 and the procedure for determining the scattering length from the asymptotic wavefunction is described in section 2.3.1. The δ-function pseudopotential routinely used to describe interatomic interaction in ultracold neutral atoms is found in section 2.3.2. The phenomena of Feshbach resonances is illustrated in section 2.4 and the interaction between a neutral atom and a single ion is discussed in section 2.5. The quantum defect theory (QDT) which was the only method used before to describe a system of a trapped atom-ion pair is briefly described at the end of the chapter.

2.1 Born-Oppenheimer approximation

The total spin-independent, non-relativistic Hamiltonian operator $\hat{\mathrm{H}}$ governing the motion of n electrons and N nuclei in a molecule can be written as

$$\begin{aligned}\hat{\mathrm{H}} &= -\frac{1}{2}\sum_{i=1}^{n}\nabla_i^2 - \frac{1}{2M_\alpha}\sum_{\alpha=1}^{N}\nabla_\alpha^2 - \sum_{i=1}^{n}\sum_{\alpha=1}^{N}\frac{Z_\alpha}{\mathbf{r}_{i\alpha}} + \sum_{i=1}^{n-1}\sum_{j>i}^{n}\frac{1}{\mathbf{r}_{ij}} + \sum_{\alpha=1}^{N-1}\sum_{\beta>\alpha}^{N}\frac{Z_\alpha Z_\beta}{\mathbf{R}_{\alpha\beta}} \\ &= \hat{\mathrm{T}}_{\mathrm{el}} + \hat{\mathrm{T}}_{\mathrm{nuc}} + \hat{\mathrm{V}}_{\mathrm{el,nuc}} + \hat{\mathrm{V}}_{\mathrm{el,el}} + \hat{\mathrm{V}}_{\mathrm{nuc,nuc}} \qquad (2.1)\end{aligned}$$

where the indices $\{i, j\}$ refer to the electrons and $\{\alpha, \beta\}$ refer to the nuclei. The first two terms represent the kinetic energy operators of the electrons and the nuclei, respectively. The third term is the electrostatic interaction between the electrons and the nuclei, the fourth term is the electron-electron repulsion and the last term is the Coulomb repulsion between the nuclei. The notation $\mathbf{r}_{i\alpha} \equiv |\mathbf{r}_i - \mathbf{R}_\alpha|$ denotes the distance between electron i and nucleus α. Same definition is true for $\mathbf{r}_{ij}$ and $\mathbf{R}_{\alpha\beta}$. The charge on nucleus α (β) is denoted by Z_α (Z_β).

Except for the very simplest cases involving only a few particles, the Schrödinger equation (SE) associated with the general many-body Hamiltonian (2.1) cannot be solved analytically even for a two-electron system like the helium atom because of the nonseparable pairwise attraction and repulsion terms. To overcome this difficulty, the BO approximation is often adopted. The physical basis for the BO approximation is the large disparity between the masses of the nuclei and the electrons. Since electrons are much lighter compared to nuclei, they move much more rapidly than the nuclei. Therefore, for the coupled motion of the electron-nuclear system which has significantly different speeds, it is possible to treat the motion of the electron as if it depends only on the fixed nuclear geometry. The total wavefunction Ψ_{tot} for the system can then be written formally as a product of the electronic wavefunction Ψ_{el} which depends parametrically on the nuclear position and the nuclear wavefunction ψ_{nuc}, i. e., $\Psi_{\text{tot}} = \Psi_{\text{el}}\, \psi_{\text{nuc}}$. Moreover, the electronic wavefunction must take care of the particle indistinguishability. To this effect, since the relativistic contributions and the spin-orbit couplings have been ignored, the total electronic wavefunction factorizes into spatial and spin wavefunctions, i. e., $|\Psi_{\text{el}}\rangle = |\psi_{\text{el}}\rangle\, |\chi_{\text{el}}\rangle$.

Thus, the Hamiltonian (2.1) for a system composed of an atom and a single ion with masses m_1 and m_2, respectively, after the separation of the center-of-mass motion[1] of the system can be expressed by

$$\hat{\mathrm{H}} \;=\; \hat{\mathrm{T}}_{\text{nuc}} + \hat{\mathrm{T}}_{\text{mp}} + \hat{\mathrm{T}}_{\text{el}} + \hat{\mathrm{V}}(\mathbf{r};\mathbf{R}) \tag{2.2}$$

where

$$\hat{\mathrm{T}}_{\text{nuc}} \;=\; -\frac{1}{2\mu}\,\nabla^2_{\mathrm{R}} \tag{2.3}$$

is the kinetic energy operator for the relative motion of the nuclei with reduced mass $\mu = m_1 m_2\,/M_{\text{tot}}$, and the total mass $M_{\text{tot}} = m_1 + m_2$. The second term is the mass polarization[2] given by

$$\hat{\mathrm{T}}_{\text{mp}} \;=\; -\frac{1}{2\,M_{\text{tot}}} \sum_{i\neq j}^{n} \nabla_i \cdot \nabla_j \;, \tag{2.4}$$

and the third term is the electron kinetic energy operator defined by

$$\hat{\mathrm{T}}_{\text{el}} \;=\; -\frac{1}{2}\sum_{i=1}^{n} \nabla^2_i \,. \tag{2.5}$$

$\mathbf{R}$ denotes the vector between the nuclei of the atom-ion pair and $\mathbf{r}$ defines the coordinates of the electrons in the center of nucleus mass frame. The last part $\hat{\mathrm{V}}(\mathbf{r};\mathbf{R}) \equiv \hat{\mathrm{V}}_{\text{el,nuc}} + \hat{\mathrm{V}}_{\text{el,el}} + \hat{\mathrm{V}}_{\text{nuc,nuc}}$ is essentially the last three terms of equation (2.1).

---

[1] See derivation in Appendix A.

[2] The mass polarization arises from the correlation between electronic momenta when the motion of the nucleus is considered [74] and can be neglected for low-energy collisions [75, 76].

Therefore, combining $\hat{\mathrm{T}}_{\mathrm{el}}$ and $\hat{\mathrm{V}}(\mathbf{r};\mathbf{R})$, the time-independent Schrödinger equation (TISE) for the nonrelativistic BO electronic Hamiltonian can be written as

$$\hat{\mathrm{H}}_{\mathrm{el}}(\mathbf{r};\mathbf{R})\,|\psi_{\mathrm{el},\,i}(\mathbf{r};\mathbf{R})\rangle = E_{\mathrm{el},\,i}\,|\psi_{\mathrm{el},\,i}(\mathbf{r};\mathbf{R})\rangle \qquad i = 1, 2, \dots, \tag{2.6}$$

where $\hat{\mathrm{H}}_{\mathrm{el}}(\mathbf{r};\mathbf{R}) = \hat{\mathrm{T}}_{\mathrm{el}} + \hat{\mathrm{V}}(\mathbf{r};\mathbf{R})$. For static geometry, the nuclear-nuclear potential term $\hat{\mathrm{V}}_{\mathrm{nuc,nuc}}$ reduces to a constant. The electronic energy of the i-th electronic state is therefore the total energy with fixed nuclei less the nuclear-nuclear repulsion potential $\hat{\mathrm{V}}_{\mathrm{nuc,nuc}}$.

Once the solutions of the electronic Schrödinger equation (SE) (2.6) are found for a number of different static nuclear configurations, the SE for the nuclear motion can be obtained as follows. Since the electronic Hamiltonian $\hat{\mathrm{H}}_{\mathrm{el}}$ is self-adjoint, its eigenfunctions form a complete orthonormal set. The total wavefunction can therefore be expanded in the following way

$$|\,\Psi_{\mathrm{tot}}(\mathbf{r},\mathbf{R})\,\rangle = \sum_{i=1}^{n} |\,\psi_{\mathrm{nuc},\,i}(\mathbf{R})\,\psi_{\mathrm{el},\,i}(\mathbf{r};\mathbf{R})\,\rangle\,. \tag{2.7}$$

Inserting the total wavefunction (2.7) into the SE with the full Hamiltonian (2.2) (without the mass polarization term) leads to

$$\sum_{i=1}^{n}\left(\hat{\mathrm{T}}_{\mathrm{nuc}} + \hat{\mathrm{H}}_{\mathrm{el}}\right)|\,\psi_{\mathrm{nuc},\,i}\,\psi_{\mathrm{el},\,i}\,\rangle = E_{\mathrm{tot}}\sum_{i=1}^{n}|\,\psi_{\mathrm{nuc},\,i}\,\psi_{\mathrm{el},\,i}\,\rangle \tag{2.8}$$

where the arguments $\mathbf{r}$ and $\mathbf{R}$ have been dropped for brevity. Multiplying equation (2.8) from the left by $\langle\psi_{\mathrm{el},\,j}|$ and integrating over the electronic coordinates yields the coupled differential equations

$$\left(\hat{\mathrm{T}}_{\mathrm{nuc}}+E_{\mathrm{el},\,j}+\hat{\mathrm{V}}_{\mathrm{nuc,nuc}}-E_{\mathrm{tot}}\right)|\,\psi_{\mathrm{nuc},\,j}\,\rangle+\sum_{i=1}^{n}\mathbf{\Lambda}_{ji}\,|\,\psi_{\mathrm{nuc},\,i}\,\rangle = 0 \quad i = 1, 2, \dots, \tag{2.9}$$

where the operator $\mathbf{\Lambda}_{ji}$ is defined by

$$\mathbf{\Lambda}_{ji} = -\sum_{\alpha=1}^{2}\frac{1}{2\mu_\alpha}\Big(\underbrace{2\langle\psi_{\mathrm{el},\,j}\,|\nabla_\alpha|\psi_{\mathrm{el},\,i}\rangle\,\nabla_\alpha}_{\text{first-order non-adiabatic}} + \underbrace{\langle\psi_{\mathrm{el},\,j}\,|\nabla_\alpha^2|\psi_{\mathrm{el},\,i}\rangle}_{\text{second-order non-adiabatic}}\Big) \tag{2.10}$$

with the terms under the braces denoting the first- and second-order non-adiabatic coupling elements.

The coupling in the set of equations (2.9) means that for any i-th equation, $\psi_{\mathrm{nuc},\,i}$ enters all other equations as the $\mathbf{\Lambda}_{ji}\psi_{\mathrm{nuc},\,i}$ term. This makes solving the set of the coupled equations (2.9) very difficult. A simple way to decouple the equations is to ignore the coupling term $\mathbf{\Lambda}_{ji}$. This can be done in two ways. One way is to neglect the coupling in (2.9) for all $i \neq j$, i. e., equating all the off-diagonal elements of $\mathbf{\Lambda}_{ji}$ to zero then only the diagonal terms with $i = j$ survive. This kind of approximation is referred to as the *adiabatic approximation*[3]. The other way is to assume that the operator $\mathbf{\Lambda}_{ji}$ is null for all i without any exception. This means that all the elements of $\mathbf{\Lambda}_{ji}$ can be equated to zero, i. e., the diagonal correction is neglected. This introduces the BO approximation[4]. With this assumption, it implies that the nuclei moves on a potential energy curve which is a solution of the electronic SE. These two approximations lead to the nuclear Schrödinger equations of the form

$$\hat{\mathrm{H}}_{\mathrm{nuc}}\, \psi_{\mathrm{nuc},\,j} = E_j\, \psi_{\mathrm{nuc},\,j} \qquad j = 1, 2 \tag{2.11}$$

here, $\hat{\mathrm{H}}_{\mathrm{nuc}}$ is the nuclear Hamiltonian. Within the adiabatic approximation, $\hat{\mathrm{H}}_{\mathrm{nuc}}$ takes the form

$$\hat{\mathrm{H}}_{\mathrm{nuc}} = \hat{\mathrm{T}}_{\mathrm{nuc}} + E_{\mathrm{el},\,j} + \hat{\mathrm{V}}_{\mathrm{nuc,nuc}} - \mathbf{\Lambda}_{jj}\,, \tag{2.12}$$

while within the BO approximation, it reduces

$$\hat{\mathrm{H}}_{\mathrm{nuc}} = \hat{\mathrm{T}}_{\mathrm{nuc}} + E_{\mathrm{el},\,j} + \hat{\mathrm{V}}_{\mathrm{nuc,nuc}}\,. \tag{2.13}$$

The interaction between an atom and a single ion can involve: an alkali atom with an alkali-metal ion of the same or different nucleus, an alkali-metal atom with an alkaline-earth ion, or an alkali-metal atom and a rare-earth ion. In all these cases, either the atom or both the atom and the ion have an electron in the outermost shell. The atom-ion interaction can be modeled within the BO approximation, which involves solving the electronic SE (2.6) for static nuclear positions and the resulting electronic eigenvalues form the potential energy curve where the two nuclei move. Solving such a problem in itself is quite laborious. However, the interaction potential energy curves can be estimated by numerical *ab initio* calculations. Alternatively, the *Rydberg-Klein-Rees* (RKR) method [77] can be used to obtain the potential energy curves. This approach gives a pair of turning points for each vibrational energy of the diatomic molecule based on spectroscopic measurements from which the potential is constructed.

The *ab initio* approaches treat the alkali atoms or dimers as an effective one- and two-electrons system moving in the field of two ionic cores and the core electrons are described using model potentials or pseudopotentials. Using numerical methods, for example, the one described in [78], an alkali dimer cation, for example, Li_2^+ can be treated as an effective one-electron system

---

[3] Only the ground state $i = 0$ is often considered in adiabatic approximation. Justification for this stems from the fact that the electron adjust instantaneously to the nuclear geometry and occupy only the ground state even for rapidly moving nuclei.

[4] The BO approximation breaks down when two or more solutions of the electronic SE come close together energetically.

and the resulting one-electron SE solved within the BO approximation using B spline basis set and prolate spheroidal coordinates, see for example, [79]. Except for simple systems like He_2 [80], it is generally very demanding to obtain high-precision *ab initio* potential curves. One way to assess the accuracy of the numerical *ab initio* data is to compare them with experimental results. Figure 2.1 shows BO potential curves of the ground state of Li_2^+ as a function of internuclear separation. Details how these potentials are constructed is provided in Chapter 5.

2.1.1 Term symbols for diatomic molecules

A diatomic molecule is formed by two identical (homonuclear) or different (heteronuclear) atoms that are chemically bonded. The term symbol for a molecular state of a homonuclear diatomic molecule is expressed as

$$^{2S+1}\Lambda^{(+/-)}_{\Omega,(g/u)} \tag{2.14}$$

Here, S is the total spin quantum number for the molecule and $2S + 1$ is the spin multiplicity. Λ is the projection of the electronic orbital angular momentum on internuclear axis. In analogy to the angular momentum $\vec{L}$ in atomic spectra, Λ takes capital Greek letters $\Lambda = \Sigma, \Pi, \Delta, \Phi, ...$ to denote $\Lambda = 0, 1, 2, 3, ...$, respectively. The symbol Ω represents the projection of the total angular momentum $|\Lambda + \Sigma|$ on the internuclear axis. For homonuclear molecules, an inversion symmetry through the midpoint between the two nuclei leaves the nuclear configuration of the molecule unchanged and so, its constituent symmetric (antisymmetric) wavefunctions are denoted *gerade* (*ungerade*) symbolized by a subscript g(u). Reflection symmetry with respect to a plane containing the internuclear axis yields symmetric (antisymmetric) wavefunctions represented by a superscript $+(-)$. For heteronuclear systems, the term symbol does not include the g/u part since they do not have an inversion center.

The example system for the atom-ion interaction in this thesis is Li_2^+. For this homonuclear system, ($Li + Li^+$), the electronic spin is $S = 1/2$ for Li and 0 (zero) for Li^+ giving a total electronic spin of 1/2 hence the spin multiplicity for this system is 2(1/2)+1=2, leading to doublet molecular potentials. The charge can be on either center thus parity transformation leads to symmetric or antisymmetric electronic wavefunction under symmetrization hence g or u state (the molecular potential curves for Li_2^+ are shown in Figure 2.1).

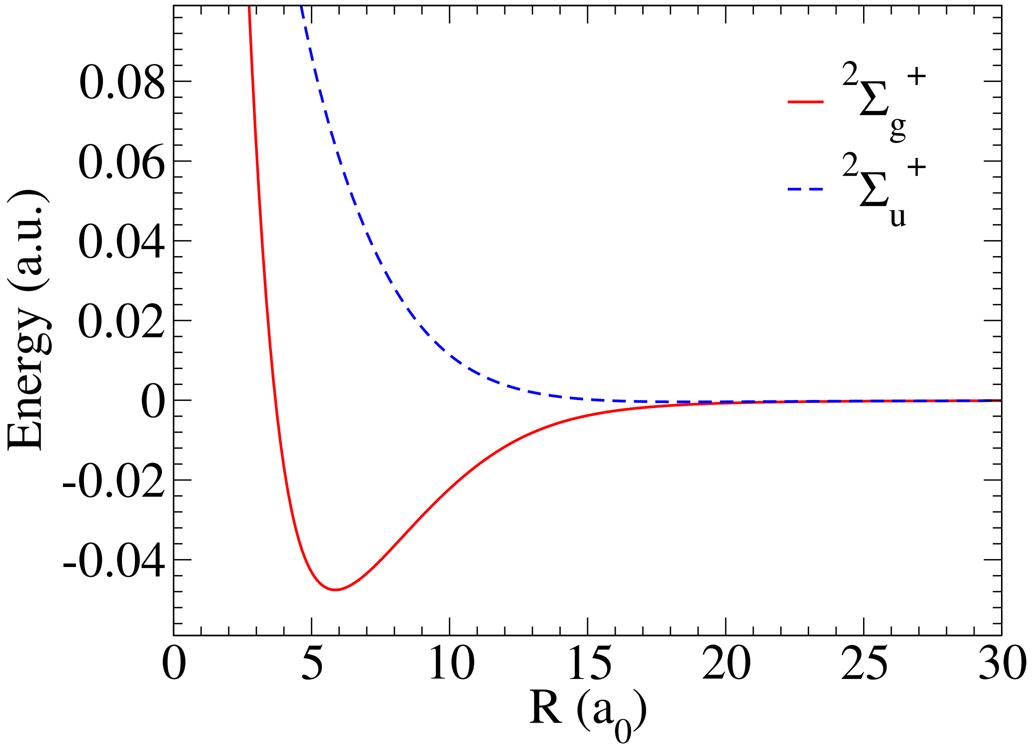

Figure 2.1: The BO potential energy curves of the two lowest electronic states for Li_2^+. The internuclear distance is units of Bohr radius a_0. The blue dashed line shows the *ab initio* potential for the *ungerade* state while the red line is the *gerade* state. These potential energy curves are taken from Ref. [81].

2.2 Optical lattices

An optical lattice is an artificial crystal of light formed by the standing wave interference pattern of two or more counterpropagating laser beams. The resulting interference pattern creates an effective periodic potential that can trap sufficiently cooled atoms.

When an atom is placed in a laser light field, the electric field $\mathbf{E}$ of the laser oscillating with the complex amplitude E at a frequency ω_L, induces an oscillating electric dipole moment $\mathbf{d}$ in the atom. The amplitude d of the dipole moment is related to the electric field amplitude E at position $\mathbf{r}$ by [82]

$$d\left(\mathbf{r}\right) = \alpha\left(\omega_L\right) E\left(\mathbf{r}\right), \tag{2.15}$$

where $\alpha(\omega_L)$ is the complex polarizability, which depends on the laser frequency ω_L and on the energies of the non-resonant excited states of the atom. Here, $\mathbf{r}$ refers to the spatial components of the electric field. The resulting dipole potential is determined by time averaging over $\mathbf{d} \cdot \mathbf{E}$ and is given by

$$V_{\text{dip}}\,(\mathbf{r}) \;=\; -\frac{1}{2\epsilon_0 c}\mathrm{Re}(\alpha)\,I(\mathbf{r}\,. \tag{2.16}$$

Here, ϵ_0 is the vacuum permittivity, c is the speed of light and $I = 2\,\epsilon_0\,c\,|E|^2$ is the intensity of the laser beam. If the laser is red-detuned (i. e., its frequency is less than a specific electronic transition frequency within an atom), the atoms are attracted towards the regions of high laser intensity corresponding to the potential minima. However, if the laser is blue-detuned, (i. e., its frequency is higher than the transition frequency), the atoms are pushed away from the maxima since the potential minima are at the positions of minimum intensity. Either way the atoms can be trapped in the bright or dark regions of the optical lattice.

The periodic potential is obtained by overlapping counterpropagating lasers to create a standing wave. In particular, superimposing three standing waves, each formed by two counterpropagating laser fields that are orthogonal to each other forms a spatially periodic OL potential for the atoms, see Figure 2.2(b), of the form

$$V_{\text{OL}} = \sum_{j=x,y,z} V_j\,\sin^2(k_j j)\,, \tag{2.17}$$

where $V_j \;=\; -\dfrac{1}{2\epsilon_0 c}\,\mathrm{Re}\{\alpha(\omega_L)\}\,I_j$ is the potential depth of the optical lattice in direction j, $k_j = 2\pi/\lambda_j$ is the wave vector, with λ_j being the wavelength of the laser creating the OL potential along direction j. The potential depth can also be expressed in units of the recoil energy $E_r^j = \;{}^2k_j^2/2m$, m being the mass of the atom. The OL potential can also be expressed in terms of a $\cos^2$ (or $\pi/2$-shifted $\sin^2$) potential of the form

$$V_{\text{OL}}^{\cos} = \sum_{j=x,y,z} V_j\,\cos^2(k_j j)\,. \tag{2.18}$$

Ultracold quantum gases confined in an OL form a fascinating physical system closely related to many systems in condensed matter and solid-state physics. Unlike a true crystal, an OL is free from defects and has no phonons. The OL potential is also directly controllable via the laser intensities and the wavelengths.

The harmonic trap potential for the atom-ion pair is important to this thesis. It can be obtained by expanding equation (2.17) in a Taylor series around the trap minima up to the second order. This will be discussed in more details later in Chapters 3 and 4 for concentric and off-centered traps, respectively.

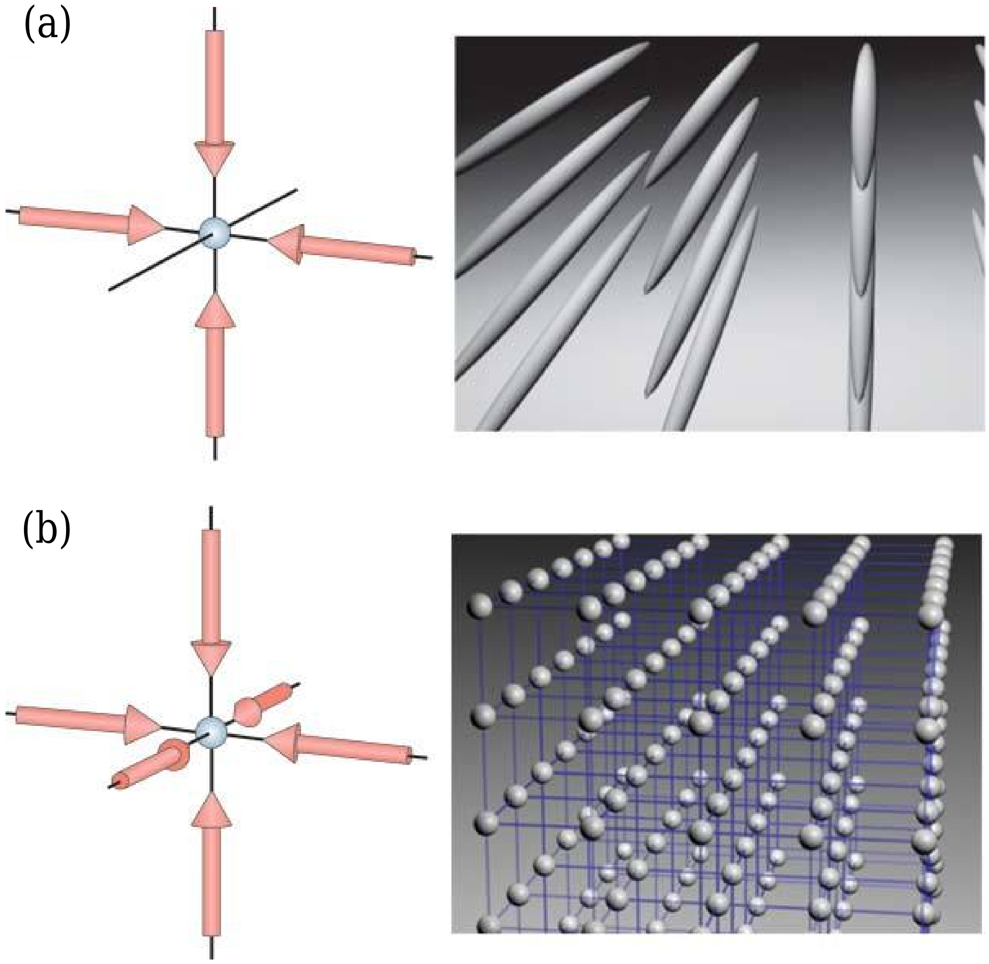

Figure 2.2: Optical lattice potentials formed by superimposing two or three orthogonal standing waves. (a) For a 2D optical lattice, the atoms are confined to an array of tightly confining 1D potential tubes. (b) In the 3D case, the optical lattice can be approximated by a 3D simple cubic array of tightly confining harmonic oscillator potentials at each lattice site. The figure and the caption are taken from Ref. [10].

2.3 Scattering at ultracold temperatures

In this section, a short overview of scattering theory relevant to the topics of this thesis is given. More comprehensive discussions can be found in standard quantum mechanics textbooks, e. g., Refs [83, 84].

Consider a two-body quantum scattering problem in free space in which the two particles interact via a spherically symmetric potential $V(r)$ that tends to zero when $r \to \infty$. The scattering properties can then be determined by solving the SE with the potential $V(r)$

$$\Big(-\frac{{}^{2}}{2\mu}\nabla^2 + V(r)\Big)\psi(\mathbf{r}) \;=\; E\,\psi(\mathbf{r})\,. \tag{2.19}$$

In free space, the problem reduces to the scattering of a particle with an incident momentum $\mathbf{k}$ on the potential $V(r)$ within the center-of-mass frame. The collision energy is

$$E = \frac{{}^{2}\,k^2}{2\mu} \tag{2.20}$$

where μ is the reduced mass of the two particles. If the interaction potential is nonzero, then the collisions between the two particles result in a scattered wave whose asymptotic form is given by

$$\psi_{\mathbf{k}}(\mathbf{r}) \;\sim\; e^{i\,\mathbf{k}\cdot\mathbf{r}} + f(E,\hat{\kappa},\hat{\mathrm{n}})\,\frac{e^{ikr}}{r}\,, \qquad r \to \infty\ . \tag{2.21}$$

The first part of the wavefunction (2.21) is an incoming plane wave while the second part describes an outgoing spherical wave that is modulated by the scattering amplitude $f(E,\hat{\kappa},\hat{\mathrm{n}})$. The unit vectors $\hat{\kappa} = \mathbf{k}/k$ and $\hat{\mathrm{n}} = \mathbf{r}/r$ indicate the directions of the incident plane wave and the scattering amplitude, respectively. The scattering amplitude contains all information about the scattering process and is related to the *differential scattering cross section* via

$$\frac{d\sigma}{d\Omega} = |f(E,\hat{\kappa},\hat{\mathrm{n}})|^2 \tag{2.22}$$

with

$$\sigma(E,\hat{\kappa}) = \int |f(E,\hat{\kappa},\hat{\mathrm{n}})|^2 \mathrm{d}^2 n \tag{2.23}$$

being the total cross section.

For a weak interaction potential, the scattering amplitude can be determined using the wavefunction with the zeroth-order approximation of $\exp(i\,\mathbf{k}\cdot\mathbf{r})$ and it is given by

$$f(E,\hat{\kappa},\hat{\mathrm{n}}) \simeq -\frac{\mu}{2\pi\ {}^{2}}\int \mathrm{d}^3\mathbf{r}'\, e^{-i\,(\mathbf{k}-\mathbf{k}')\cdot\mathbf{r}'}\, V\,(\,\mathbf{r}'\,)\,. \tag{2.24}$$

The expression given by equation (2.24) above is known as the *Born approximation.* Within this approximation, the scattering amplitude is given by the Fourier transform of the potential with respect to the momentum transfer. Here, $\mathbf{k}'$ is the momentum of the outgoing plane wave. This approximation often gives good results for high kinetic energies but it is not exact and does not account for the effective range of the potential. For low-energy scattering, it is often useful to expand the incident and scattered wavefunctions in spherical coordinates by means of a partial wave expansion,

$$\psi(\mathbf{r}) = \sum_{l=0}^{\infty} \sum_{m=-l}^{m=l} Y_l^m(\theta,\phi) \frac{u_{k,l,m}(r)}{r}\,, \tag{2.25}$$

where ϕ is the azimuthal angle around the z axis, defined as the incident wavefunction direction and $Y_l^m(\theta,\phi)$ are the spherical harmonic functions. Because the potential is spherically symmetric, the index m is zero[5]. Therefore, the spherical harmonics contributing to the scattering are $Y_l^0(\theta,\phi) \propto P_l(\cos(\theta)$, where $P_l(\cos(\theta)$ are the Legendre polynomials. Inserting the expansion equation (2.25) in to the SE (2.19) leads to a radial SE for the reduced wavefunction ($u \equiv r\psi$) that describes the collisions of the form

$$\left[-\frac{{}^2}{2\mu}\frac{\mathrm{d}^2}{\mathrm{d}r^2} - E + V_{\text{eff}}\,(r)\right] u_{k,l}(r) = 0\,. \tag{2.26}$$

The two particles feel an l-dependent effective potential

$$V_{\text{eff}}\,(r) = V(r) + \frac{{}^2\, l(l+1)}{2\mu r^2}. \tag{2.27}$$

The second term in equation (2.27) is called the *centrifugal barrier.* It introduces an additional repulsive term to the potential for $l \neq 0$ states. At ultracold temperatures, the particles are not able to overcome the barrier for higher partial waves and only the $l = 0$ contributions are important. The consequence of this is that, the lower the temperature, the lower the number of the partial waves that have to be taken into account to describe the collisions. The scattering for $l = 0, 1, ...,$ are referred to as s-wave, p-wave, etc.

The asymptotic form of the radial wavefunction to equation (2.26) for $kr \gg 1$ is

$$u_{k,l}(r) \sim \sin\left(kr - l\frac{\pi}{2} + \delta_l\right), \quad r \to \infty\,. \tag{2.28}$$

From equation (2.28), the radial wavefunction $u_{k,l}(r)$ behaves in the same manner as a free wave except a possible phase shift δ_l for the reflected outgoing wave. Therefore, the effect of the potential $V(r)$ at short-range is seen in the asymptotic limit $r \to \infty$ only as phase shifts δ_l to the radial wavefunction.

The partial wave expansion (2.25) of the incident and the scattered waves in equation (2.21) leads to the scattering amplitude $f(k,\theta)$ and total cross section $\sigma(k)$ of the form

$$f(k,\theta) = \frac{1}{2ik}\sum_{l=0}^{\infty}(2l+1)(e^{2i\delta_l} - 1)\,P_l(\cos\theta) \tag{2.29}$$

---

[5] This is not fulfilled anymore for dipolar quantum gases where the dipole-dipole interaction is not negligible or those of polar heteronuclear molecules.

and

$$\sigma(k) = \frac{4\pi}{k^2} \sum_{l=0}^{\infty} (2l+1) \sin^2 \, \delta_l(k) \,, \tag{2.30}$$

respectively. The total cross section can also be expressed in terms of the imaginary part of the forward scattering amplitude $f(k, \theta = 0)$ according to

$$\operatorname{Im} f(k, \theta = 0) \; = \frac{k}{4\pi} \, \sigma \,. \tag{2.31}$$

The relationship between the forward scattering amplitude and the total cross section of the scatterer given by equation (2.31) is known as the *optical theorem*. It shows that all the scattering information including the differential ones are already contained in the scattering amplitude for $\theta = 0$.

Also, since the scattering wavefunction must be (anti)symmetric with respect to exchange of the atom pair, the scattering amplitude $f(k, \theta)$ should be replaced by $f(k, \theta) \pm f(k, \pi - \theta)$, where the $(+)$ term corresponds to symmetrization for bosons and the $(-)$ part corresponds to the anti-symmetrization for fermions with $0 \leq \theta \leq \pi/2$. Therefore, using the properties of the Legendre polynomials and the (anti)symmetrization requirements, the expressions for the scattering cross section for polarized bosons and fermions will then contain only even or odd values of l given by

$$\sigma_+(k) = \frac{8\pi}{k^2} \sum_{l \, \text{even}}^{\infty} (2l+1) \sin^2 \, \delta_l(k) \,, \quad \text{for bosons} \,, \tag{2.32}$$

and

$$\sigma_-(k) = \frac{8\pi}{k^2} \sum_{l \, \text{odd}}^{\infty} (2l+1) \sin^2 \, \delta_l(k) \,, \quad \text{for fermions} \,, \tag{2.33}$$

respectively.

2.3.1 Scattering length

In the low-energy limit, i. e., $kr \ll 1$, we do not resolve the angular properties of the scattering potential since only the $l = 0$ partial waves have to be taken into account. If the energy term E is neglected altogether, then the stationary radial SE (2.26) for the s-wave can be written as

$$\frac{\mathrm{d}^2 \, u(r)}{\mathrm{d}r^2} = \frac{2\mu}{{}^2} V(r) \, u(r) \,. \tag{2.34}$$

Using inner boundary condition $u(0) = 0$, then for an arbitrary potential $V(r)$ that obey the asymptotic condition

$$\lim_{r\to\infty} r^n\, V(r) = 0 \quad \text{for} \quad n > 3\,, \tag{2.35}$$

the wavefunction $u(r)$ has to be linear such that [85]

$$\psi(r) = \frac{u(r)}{r} = \frac{b(r - a_{\mathrm{sc}})}{r} = b\left(1 - \frac{a_{\mathrm{sc}}}{r}\right), \quad r \to \infty\,, \tag{2.36}$$

where a_{sc} and b are real constants.

The constant a_{sc} which is the intersection of the asymptotic straight line and the r axis will be the definition of the *scattering length*. This is the technique used to determine the scattering length values in the present work. If the phase is chosen such that the wavefunction is real, then the curvature of the wavefunction will have the same sign as the wavefunction itself in regions where the potential is repulsive ($a_{\mathrm{sc}} > 0$) and an opposite sign in regions where the potential is attractive ($a_{\mathrm{sc}} < 0$). The absolute value of the scattering length gives the interaction strength. The graphical representation given in Figure 2.3 illustrates how the scattering length can be determined from the intersection of the asymptotes of the scaled radial wavefunction and the r axis.

In the ultracold regime, the collision between the atoms can be described to a good approximation by a single parameter, the scattering length [86]. This greatly simplifies the theoretical description of the atoms in the low-energy collision regime. The true interaction potential between the atoms can be replaced by a simple pseudopotential that can reproduce the same scattering length as the true potential, see discussions in section 2.3.2.

To wrap up the discussion on the scattering lengths, it is noteworthy to mention that there exists an analytical formula for calculating the scattering length corresponding to a potential $V(r)$ that decays asymptotically as $-C_n/r^n$, with $n = 4$ for atom-ion interaction and $n = 6$ for interacting pair of neutral atoms as $r \to \infty$ that was obtained by Gribbakin and Flambaum [88], also discussed in [89]. The scattering length is calculated (using the Wentzel-Kramers-Brillouin (WKB) approximation [90]) by matching the semiclassical wave function inside the potential well with the exact solution in the asymptotic region. For atom-ion collisions, the scattering length takes the form

$$a_{\mathrm{sc}} \;=\; -\sqrt{\mu\, C_4}\, \tan\left(\Phi - \frac{\pi}{4}\right) \tag{2.37}$$

where C_4 is the static dipole polarizability and Φ is the semiclassical phase given by

$$\Phi \;=\; \int_{r_0}^{\infty} \sqrt{-\mu\, V(r)}\, \mathrm{d}\, r \tag{2.38}$$

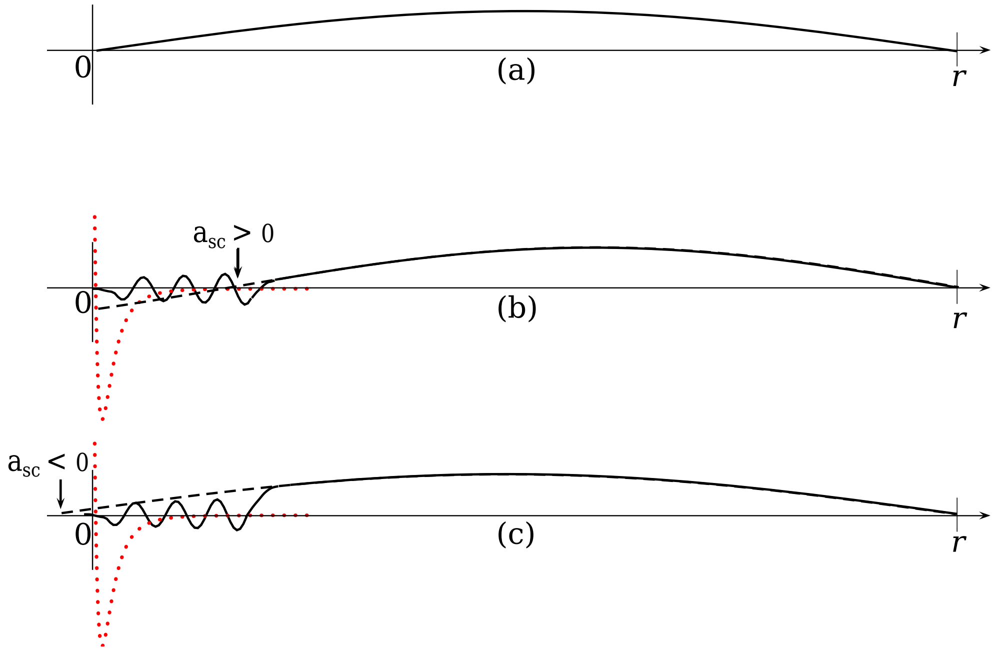

Figure 2.3: Representation of the s-wave radial wavefunction in a spherical box of radius r with strict boundary conditions (solid line): (a) in the absence of interactions, (b) with a positive scattering length, and (c) with a negative scattering length. The dotted red lines in (b) and (c) denote the interaction potentials. The dashed line is the extrapolating function $u(r)$ for all r of the asymptotic form of the radial wave. Its intersection with the axis gives the value and the sign of the scattering length. Figure and caption adopted from Ref. [87].

with r_0 being the zero energy classical turning point[6] obtained from the solution when the potential $V(r)$ is zero. The phase Φ passes through many cycles of π at the threshold energy. Gribbakin and Flambaum also showed that the number of bound states $\mathrm{N_{bs}}$ supported by the potential $V(r)$ is given by

$$\mathrm{N_{bs}} = \left[\frac{\Phi}{\pi} - \frac{n-1}{2(n-2)}\right] + 1 \tag{2.39}$$

where the value inside the square bracket indicates the largest integer. The value of $a_{\rm sc}$ calculated using the intersection of the asymptotic part of the wavefunction (2.36) or by the numerical integration of the potential $V(r)$ using equation (2.37) should be the same.

---

[6] As a technical detail, for numerical potential curves, this value must be accurately determined in order to find the correct scattering length and the phase Φ of the potential. One can use for example, the 'FindRoot' feature of *Mathematica* to numerically determine this point.

2.3.2 Regularized δ-function pseudopotential

The regularized zero-range s-wave (Fermi-Huang) pseudopotential [91, 92] given by equation (2.42) is often used to model two-body interaction potentials for sufficiently low-energy scattering. This potential can be obtained from equation (2.36) as follows: we seek a solution of the form $V(r) \propto \delta(r)$ and use the trick $\frac{\partial}{\partial r}(r\,\psi(r)) = b$ to find the exact form of $V(r)$, i. e., from the source equation $\nabla^2 \frac{1}{r} = 4\pi\delta(r)$, we have

$$\nabla^2\,\psi(r) = -4\pi\,a_{\mathrm{sc}}\,\delta(r)\,b \tag{2.40}$$

substituting for b in (2.40) gives

$$\nabla^2\,\psi(r) = -4\pi\,a_{\mathrm{sc}}\,\delta(r)\,b = -4\pi\,a_{\mathrm{sc}}\,\delta(r)\,\frac{\partial}{\partial r}\,(r\,\psi(r)) \tag{2.41}$$

dropping $\psi(r)$ from both sides yields the Fermi-Huang δ pseudopotential

$$V_{\mathrm{pseudo}}(\mathbf{r}) \;=\; \frac{4\pi\quad{}^{2}\,a_{\mathrm{sc}}}{m}\,\delta(\mathbf{r})\,\frac{\partial}{\partial r}\,r\,. \tag{2.42}$$

The pseudopotential $V_{\mathrm{pseudo}}(r)$ is simple and can be used to replace the exact potential $V(r)$ provided it gives the same scattering length as $V(r)$ and allows for the Born approximation treatment [87]. For a system of two ultracold neutral atoms trapped in harmonic potentials, analytical solutions to the SE exists if the interaction potential is modeled using the δ-function pseudopotential [93–97]. However, for a system composed of an ultracold neutral atom and a single ion, the δ-function pseudopotential approximation does not hold anymore [72]. This is discussed later in section 2.5. The prefix *pseudo* implies that it is not a true potential like the actual interaction between the two atoms, but simply an operator that accounts for the phase shift of the interatomic interaction potential $V(r)$ at the same time giving a good approximation of the eigenvalues and the corresponding eigenfunctions of the SE when used instead of the actual interaction potential.

2.4 Feshbach resonances

A Feshbach resonance in ultracold collisions arises when the scattering state of two atoms colliding in the *open channel* resonantly couple to a molecular bound state in the *closed channel* [4]. A two-channel model for a Feshbach resonance is illustrated schematically in Figure 2.4. The open channel (red) is the interaction potential along which the colliding atoms scatter. The closed

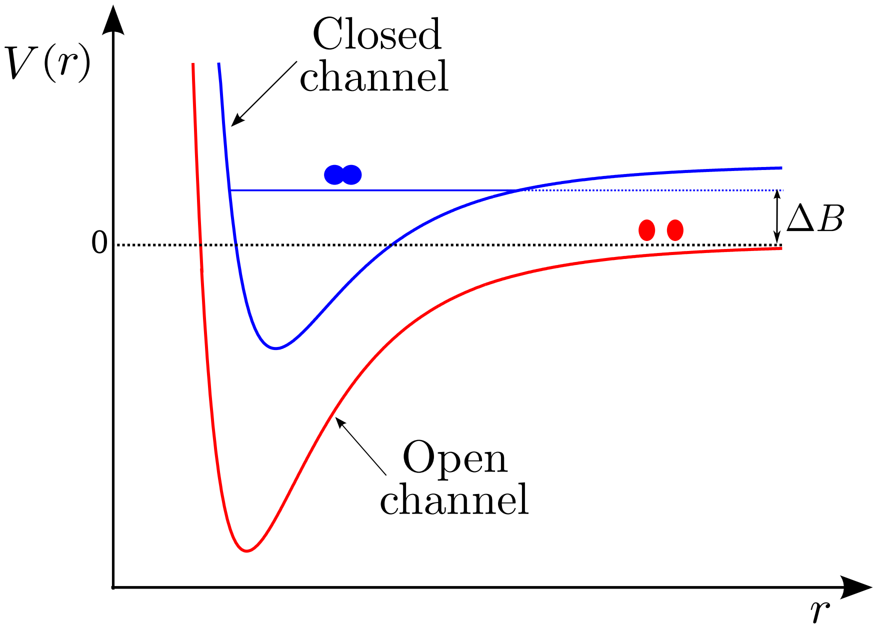

Figure 2.4: Schematic illustration of a two-channel model for a Feshbach resonance. A Feshbach resonance arises if the energy of the free atoms in the open channel (red) couples resonantly with the energy of the bound state in the closed channel (blue). The resonance can be controlled by modifying the relative position of scattering and bound states using an external magnetic field.

channel (blue) contains the resonant bound state whose dissociation energy threshold is above that of the colliding atoms in the open channel. If the scattering and the bound states have different magnetic moments, an applied magnetic field shifts the two channels with respect to each other and so to the energy difference between them owing to the Zeeman effect. This modification of the collision potential results in a change of the scattering length a_{sc}.

The scattering length is related to the applied magnetic field B by [98]

$$a_{\mathrm{sc}}(B) = a_{\mathrm{bg}}\left(1 - \frac{\Delta B}{B - B_0}\right), \tag{2.43}$$

where a_{bg} is the off-resonant background scattering length of the open channel, ΔB is the width and B_0 is the position of the resonance. Equation (2.43) shows that very large positive and negative values of a_{sc} can be realized with magnetic Feshbach resonances. This tunability of the interactions that Feshbach resonances facilitate remains one of the cornerstones of ultracold atomic physics. A quantitative introduction to the theory of Feshbach resonances can be found e. g., in Refs. [4, 99].

Generally, the accurate calculation of magnetic Feshbach resonances entails solving a complex multi-channel problem. However, a Feshbach resonance can be described in terms of its entrance-channel component, e. g., the method developed in [100] for mimicking the variation of the scattering length at a Feshbach resonance with single-channel approach. The procedure used in this thesis is the variation of the steep repulsive inner wall of the BO potential curve of the atom-ion interaction potential. This will be described in details in Chapter 5.

Finally, let us remark that magnetic Feshbach resonances have been predicted theoretically for the hybrid atom-ion systems [46] but reaching the s-wave collision regime in current experiments has not been possible due to the higher energies that arise from the long-range nature of their interactions (see section 2.5) and the large elastic cross section.

2.5 Atom-ion polarization potential

At large internuclear separations between the atom-ion pair, the interaction potential can be expressed in terms of the multipole expansion $\sum C_n/r^n$ where C_n is the leading van der Waals coefficient. The dominant interaction between the two particles can be understood as follows. A singly charged ion with elementary charge e creates an electric field

$$\varepsilon(r) = \frac{e}{4\pi\,\varepsilon_0\,r^2} \tag{2.44}$$

at a distance r where ε_0 is the vacuum permittivity. This electric field induces a dipole moment

$$d(r) = 4\pi\,\varepsilon_0\,\alpha\,\varepsilon(r) \tag{2.45}$$

in a neutral atom where α is the atom's static electric dipole polarizability. The long-range behavior of the atom-ion potential is therefore characterized by the interaction between the charge of the ion and the dipole moment of the atom for states without permanent quadrupole moment. The dominant term of this polarization potential V_{pol} is well known at large distances and is given by [101]

$$\lim_{r\to\infty} V_{\mathrm{pol}}(r) \simeq -\frac{1}{2}\,d(r)\,\varepsilon(r) \sim -\frac{C_4}{r^4} \tag{2.46}$$

where $C_4 = \alpha e^2/(8\pi\varepsilon_0)$. However, the short-range behavior of V_{pol} is more complicated and is not well known. Equation (2.46) is only valid for separation distances larger than the radius that defines the characteristic size of the inner core region of the atom-ion complex. This characteristic radius of the atom-ion potential is defined by [72]

$$R^* = \sqrt{2\mu C_4/\ ^2}\,. \tag{2.47}$$

The length scale R^* is useful in the characterization of atom-ion properties such as the size of the least bound states [102], the interaction range and provides a limit for typical scattering length values [44]. Another characterization of the atom-ion interaction is given by the characteristic energy E^* which is defined by [72]

$$E^* = \ ^2/(2\mu R^{*2})\,. \tag{2.48}$$

This energy scale sets the energy spacing for the loosely bound states and the onset of the s-wave scattering of the atom-ion collisions. As already mentioned in section 2.4, the atom-ion s-wave scattering length has not been measured in current experiments. This is due to the very low temperatures required for the onset of atom-ion s-wave scattering. To illustrate this, consider an example of Li_2^+ potential, using equations (2.48) and (2.47) with $C_4 = 164$ a.u, the characteristic energy $E^* = 23.54\,\mu\text{K} \times k_B$ where μK stands for microkelvin and k_B is the Boltzmann constant. Despite the fact that this energy is in the microkelvin range and that it is possible to cool neutral atoms to much lower temperatures up to the nanokelvin regime, the typical atom-ion collision energies are presently technically limited to energies on the order of $\text{mK}\times k_B$ or higher [44].

The polarization potential (2.46) diverges for $r \to 0$. In this limit of small separations, the higher terms like the exchange forces begin to dominate the atom-ion interaction which becomes strongly repulsive and as already pointed out, the exact form of the potential becomes complicated [72]. In the case of ultracold neutral atoms, the characteristic length of the trapping potential is typically much larger than the characteristic radius (2.47) of the interatomic interaction hence the justification to describe the atom-atom interaction using the δ-function pseudopotential (2.42). However, for the atom-ion system, the characteristic range R^* of the polarization potential (2.46) is comparable to or larger than the typical size of the trap potentials preventing the use of the contact pseudopotential to describe the interaction [72, 103]. Using the example of Li_2^+, the characteristic length, $R^* \approx 1024\,a_0$. Therefore, an atom confined in an isotropic harmonic potential with length

$$l_j = \sqrt{\ /(m_j\omega_j)}, \tag{2.49}$$

at a frequency say $\omega_a = 2\,\pi \times 100\,\text{kHz}$ has a trap length, $l_a \approx 904\,a_0$, while the length of an ion trap confined with a frequency of $\omega_i = 2\,\pi \times 200\,\text{kHz}$ is $l_i \approx 639\,a_0$, (a_0 is the Bohr radius). Both of these two trap lengths are smaller than the atom-ion characteristic length R^*.

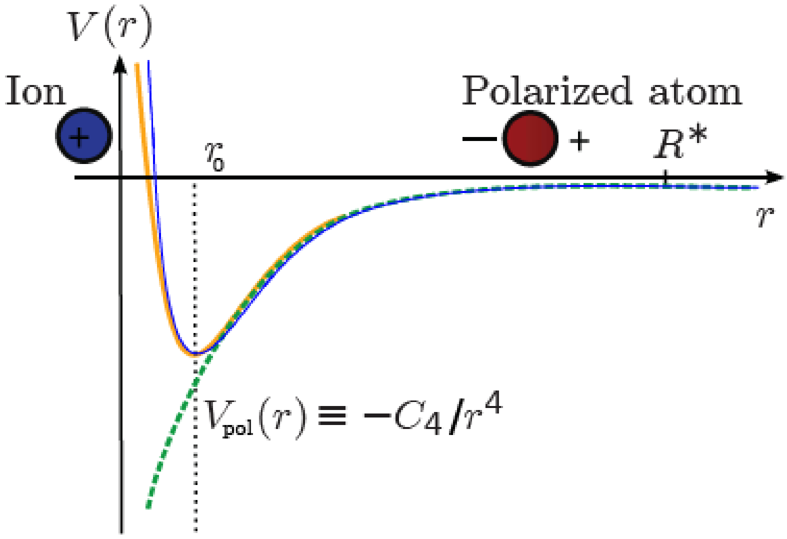

Figure 2.5: The long-range part of the atom-ion interaction potential is given by the polarization potential $V_{\rm pol}(r)$. At distances smaller than the potential minimum r_0, repulsive terms start to dominate. Quantum defect theory replaces the actual potential $V(r)$ (solid yellow line) with a reference potential $V_{\rm pol}(r)$ (dashed green line) and includes the short-range effects using a quantum-defect parameter related to the short-range phase of the relative wave function. The characteristic range R^* of the interaction is typically much larger than r_0. Figure and caption are taken from Ref. [56]. The blue solid line has been included to indicate the full atom-ion potential obtained by merging the *ab initio* data for the short-range with the known long-range part.

The QDT approach, briefly discussed in section 2.6, has been used [72] to describe trapped atom-ion systems where the details of the interaction at short separation distances is not known and the pseudopotential is not applicable. A schematic illustration of atom-ion interaction is shown in Figure 2.5. In this thesis, the atom-ion interaction potential is described by using a realistic interaction potential numerically provided by a Born-Oppenheimer curve.

2.6 Quantum defect theory

Quantum defect theory is a well established and a powerful concept in atomic physics. It provides a technique for describing scattering processes when the exact form of the interparticle interaction at short distances is unknown. A detailed account of the history of the development of QDT and multichannel

QDT can be found in [104–107]. Applications of this method to the atom-ion system can be found in [46, 56, 72, 102, 108–110] and the references therein.

In this section, the basic features of QDT are highlighted following [72] where a hybrid trapped atom-ion system was investigated theoretically for the first time. Consider a single atom and a single ion trapped in a harmonic potential whose relative motion part is given by

$$V_{\mathrm{t}} = \frac{1}{2}\,\mu\,\omega^2\,r^2 \tag{2.50}$$

where ω is the trapping frequency. Including the trap potential (2.50) in the radial SE (2.26) gives

$$\left[-\frac{\mathrm{d}^2}{\mathrm{d}r^2} + \frac{2\mu}{{}^{2}}\left(\frac{{}^{2}\,l(l+1)}{2\mu r^2} + \frac{1}{2}\mu\,\omega^2\,r^2 + V(r) - E\right)\right]u_{k,l}(r) = 0\,. \tag{2.51}$$

The basic idea of QDT is to replace the true interaction $V(r)$ by a reference potential that produces the correct asymptotic behavior, in this case, the polarization potential (2.46). At short distances when $r \to 0$, the energy of the trapping potential becomes negligible compared to that of the atom-ion interaction. Also, the wavefunction becomes independent of the total energy and the relative orbital angular momentum [111]. Therefore, the only dominant energy is the polarization term $-C_4/r^4$ and the resulting SE becomes

$$\left[\frac{\mathrm{d}^2}{\mathrm{d}r^2} + \left(\frac{R^*}{r^2}\right)^2\right]u_l(r) = 0 \tag{2.52}$$

whose solution is

$$u_l(r) = r\,\sin\left[\frac{R^*}{r} + \varphi\right] \tag{2.53}$$

for small r and φ is the short-range phase that depends on the internal structure of the atom and the ion. The phase φ constitutes the quantum defect parameter that define the phase of the oscillation. When $k = 0$, the solution (2.53) becomes valid for all r. Using the asymptotic behavior for the zero-energy solution (2.36) in equation (2.53), the relationship between the short-range phase and the s-wave scattering length is found to be

$$a_{\mathrm{sc}} = -R^*\,\cot\,\varphi\,. \tag{2.54}$$

The quantum defect parameter φ can then be calculated if the value of the scattering length is known.

Chapter 3

Numerical Techniques

The description of the method for theoretically treating two ultracold neutral atoms interacting via a central potential while trapped in a finite three-dimensional (3D) optical lattice is given in [73]. The model was developed by Sergey Grishkevich (first introduced in [112, 113]) and it allows for the full numerical description of a pair of trapped atoms using realistic interatomic interaction potentials, typically Born-Oppenheimer curves. The salient features of the approach is reviewed in this chapter following closely the original work in [73]. The motivation for doing this is to provide the underlying features of the method before its extension to incorporate trap potentials that are off-centered which is the topic of discussion in the next chapter. In addition, the method in this chapter will be used in the discussion in Chapter 7. The description of the programs used to perform the calculations is also given.

3.1 Hamiltonian

The Hamiltonian describing two interacting atoms $i = 1, 2$ with mass m_i trapped in a three-dimensional optical lattice is given by

$$\hat{\mathrm{H}}(\mathbf{r}_1, \mathbf{r}_2) = \hat{\mathrm{T}}_1(\mathbf{r}_1) + \hat{\mathrm{T}}_2(\mathbf{r}_2) + \hat{\mathrm{V}}^{(1)}_{\mathrm{trap}}(\mathbf{r}_1) + \hat{\mathrm{V}}^{(2)}_{\mathrm{trap}}(\mathbf{r}_2) + \hat{\mathrm{U}}_{\mathrm{int}}(\mathbf{r}_1, \mathbf{r}_2) \tag{3.1}$$

where $\hat{\mathrm{T}}_i$ is the kinetic energy operator for atom i, $\hat{\mathrm{V}}^{(i)}_{\mathrm{trap}}$ denotes the sinusoidal-like trapping potential experienced by atom i, and $\hat{\mathrm{U}}_{\mathrm{int}}$ is the atom-atom interaction potential. The trapping potential is that of an OL (already discussed in Chapter 2) given by

$$\hat{\mathrm{V}}^{(i)}_{\mathrm{trap}}(\mathbf{r}_i) = \sum_{c\,=\,x,y,z} V^{(i)}_c \sin^2(k_c c_i) \tag{3.2}$$

here, c refers to the Cartesian coordinates x, y, and z.

Solving the SE associated with the Hamiltonian (3.1) is complicated. This is due to the dependence of $\hat{\mathrm{U}}_{\mathrm{int}}$ on all six coordinates describing the two-particle system, even if the interatomic interaction is central, i. e., $\hat{\mathrm{U}}_{\mathrm{int}}(\mathbf{r}_1, \mathbf{r}_2) = \hat{\mathrm{U}}_{\mathrm{int}}(|\mathbf{r}_1 - \mathbf{r}_2|)$. Therefore, the interaction term expressed in the absolute Cartesian coordinates leads to very laborious six-dimensional integrals. Treating this problem within the center-of-mass (c.m.) and relative (rel.) motion coordinates turns out to be convenient. The apparent advantage of formulating the problem within the c.m. and the rel. motion coordinates is that it allows for the inclusion of realistic interaction potentials without having to deal with six-dimensional integrals. This is due to the fact that the interaction potential acts only on the relative motion coordinate. Therefore, the dimensions of $\hat{\mathrm{U}}_{\mathrm{int}}$ reduce from six to three. Furthermore, when spherical coordinates are adopted like in the present case, the interaction potential becomes a function of the radial coordinate only.

The rel.-motion and c.m. coordinates $\mathbf{r}$ and $\mathbf{R}$, respectively, are defined as

$$\begin{aligned} \mathbf{r} &= \mathbf{r}_1 - \mathbf{r}_2 & (3.3) \\ \mathbf{R} &= \mu_1\,\mathbf{r}_1 + \mu_2\,\mathbf{r}_2 & (3.4) \end{aligned}$$

with the dimensionless parameters $\mu_i = m_i/(m_1+m_2)$. However, the transition to the c.m. and the rel. motion coordinates frame complicates the treatment of the trapping potential equation (3.2) because the original separability in the absolute Cartesian coordinates is lost. Complete separability in the c.m. and relative-motion coordinates exists only within the harmonic approximation for the trap potential for two identical particles in the same internal state. In such a case, an analytical solution of the SE for two particles in isotropic and anisotropic harmonic traps exists if the atom-atom interaction potential is replaced by a δ-function pseudopotential that reproduces the two-body zero-energy s-wave scattering asymptotically [93–97]. Noteworthy, even in a purely harmonic trap potential, the center-of-mass and relative-motion coordinates do not separate if the two particles are not identical or if they experience different trapping potentials.

Performing a Taylor series expansion of the trapping potential (3.2) around the origin in Cartesian c.m. and rel. coordinates allow for the splitting of the trap potential according to

$$\hat{\mathrm{V}}(\mathbf{R},\mathbf{r}) = \hat{\mathrm{V}}_{\mathrm{c.m.}}(\mathbf{R}) + \hat{\mathrm{v}}_{\mathrm{rel.}}(\mathbf{r}) + \hat{\mathrm{W}}(\mathbf{R},\mathbf{r}) \qquad (3.5)$$

where $\hat{\mathrm{V}}_{\mathrm{c.m.}}$ and $\hat{\mathrm{v}}_{\mathrm{rel.}}$ are the separable parts of the trap potential containing only the c.m. and the rel. motion coordinates, respectively. The coupling terms between the c.m. and the rel. motions are contained in $\hat{\mathrm{W}}(\mathbf{R},\mathbf{r})$. The corresponding components of the trap potential (3.5) are given by [73]

$$\begin{aligned} \hat{\mathrm{V}}_{\mathrm{c.m.}}(\mathbf{R}) &= -\frac{1}{2}\sum_{s=1}^{2}\sum_{c=x,y,z} V_c^s \sum_{k=1}^{n} {}^{\cos}_{0kcs}\, R_c^{2k} & (3.6) \\ \hat{\mathrm{v}}_{\mathrm{rel.}}(\mathbf{r}) &= -\frac{1}{2}\sum_{s=1}^{2}\sum_{c=x,y,z} V_c^s \sum_{t=1}^{n} {}^{\cos}_{t0cs}\, r_c^{2t} & (3.7) \end{aligned}$$

$$\begin{aligned}\hat{\mathrm{W}}(\mathbf{R},\mathbf{r}) \;=\; & \frac{1}{2}\sum_{s=1}^{2}\sum_{c=x,y,z} V_c^s \Bigg[(-1)^{\eta_s} \sum_{j=0}^{n-1}\sum_{i=0}^{n-1-j} {}^{\sin}_{ijcs}\, R_c^{2i+1}\, r_c^{2j+1} \\ & - \sum_{t=1}^{n}\sum_{k=1}^{n-t} {}^{\cos}_{tkcs}\, R_c^{2k}\, r_c^{2t} \Bigg] \end{aligned} \tag{3.8}$$

where $\eta_s = s + (-1)^{s-1}$. The coefficients ${}^{\cos}_{tkcs}$ and ${}^{\sin}_{ijcs}$ are defined by

$$\begin{aligned} {}^{\cos}_{tkcs} &= \frac{(-1)^{k+t}}{(2k)!(2t)!}\,(2k_c)^{2(k+t)}\,\mu_{\eta_s}^{2t}\,, \\ {}^{\sin}_{ijcs} &= \frac{(-1)^{i+j}}{(2i+1)!(2j+1)!}\,(2k_c)^{2(i+j+1)}\,\mu_{\eta_s}^{2j+1}\,. \end{aligned} \tag{3.9}$$

As discussed in Chapter 2, the OL can also be expressed in terms of a $\cos^2$ potential. The expressions for the $\cos^2$ trap potentials in c.m. and rel. coordinates are the same like the ones given in equations (3.6) - (3.8) but with opposite sign and an extra equation for the constant part (see equations (43) - (46) in Ref. [73]). The infinite Taylor expansion of the $\sin^2$ ($\cos^2$) is restricted up to the (2n)th degree with the orders $n = 1, 2, 3, \ldots$, where n should be odd (even) in the $\sin^2$ ($\cos^2$) cases so that the OL potential $\hat{\mathrm{V}}_{\mathrm{trap}} \to +\infty$ and the wavefunctions decay exponentially as $r \to \infty$. The upper panel of Figure 3.1 shows the lattice form $\sin^2$ (red solid line). The second order expansion gives the harmonic trap potential (blue line). The sixth order expansion gives the sextic potential (green line). This sextic form of trap potential reproduces a very good approximation for a single-well of the $\sin^2$ potential and thus of the OL compared to the harmonic approximation. The 4th order expansion (black dashed line) tends to $-\infty$ for all x values going to $\pm\infty$. Therefore, the expansion to this order results in unphysical negative-energy states. The lower panel shows the alternative lattice form $\cos^2$ (red line) together with the 6th- (green dashed line) and the 12th- order (blue solid line) expansions of the Taylor series.

Another unique feature of the program is that it provides for the flexibility on the form of periodic potential to use, i. e., one can use either a $\sin^2$ or a $\cos^2$ or a combination of both depending on the trap geometry of interest. For example, an atom-ion system composed of an ultracold neutral atom in a double-well potential and an ion trapped in an harmonic potential at the center of the atom cloud (like the one investigated in [55]) can be realized by Taylor expanding a $\cos^2$ potential up to the 12th order to obtain a double-well potential together with a $\sin^2$ potential expanded up to the 2nd order for a single-well potential as shown in Figure 3.2. It is also possible to use the program to simulate other forms of generic confinement potentials for example those with Gaussian shapes.

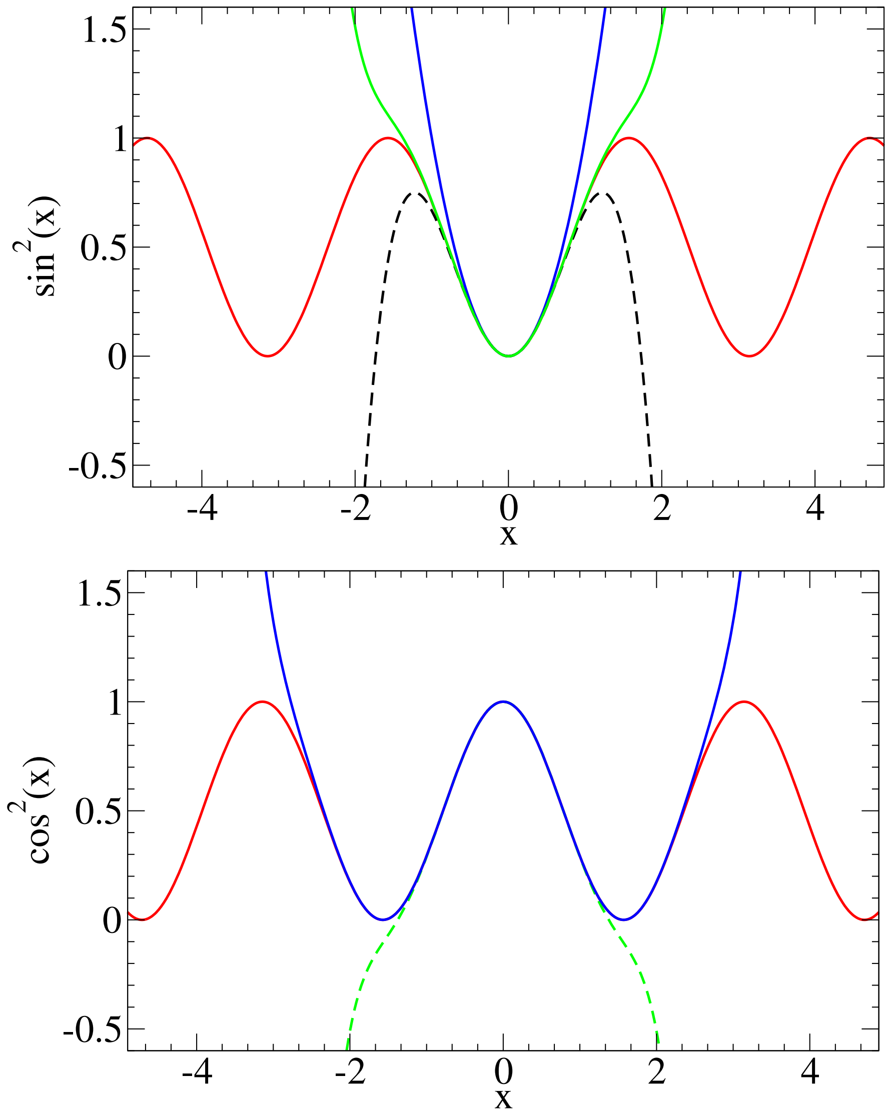

Figure 3.1: Top: The $\sin^2(x)$ function (red solid line) together with the 2^{nd}- (blue line), 4^{th}- (black dashed line) and 6^{th}- order (green solid) expansion of the Taylor series.
Bottom: The $\cos^2(x)$ function (red) together with the 6^{th}- (green dashed line) and the 12^{th}- order (blue solid line) expansion of the Taylor series.

After performing the Taylor expansion of the trap potential around the origin and the transformation of the Hamiltonian (3.1) into c.m.-rel. motions frame, the resulting Hamiltonian takes the form

$$\hat{\mathrm{H}}(\mathbf{R},\mathbf{r}) = \hat{\mathrm{H}}_{\mathrm{c.m.}}(\mathbf{R}) + \hat{\mathrm{h}}_{\mathrm{rel.}}(\mathbf{r}) + \hat{\mathrm{W}}(\mathbf{R},\mathbf{r}) \tag{3.10}$$

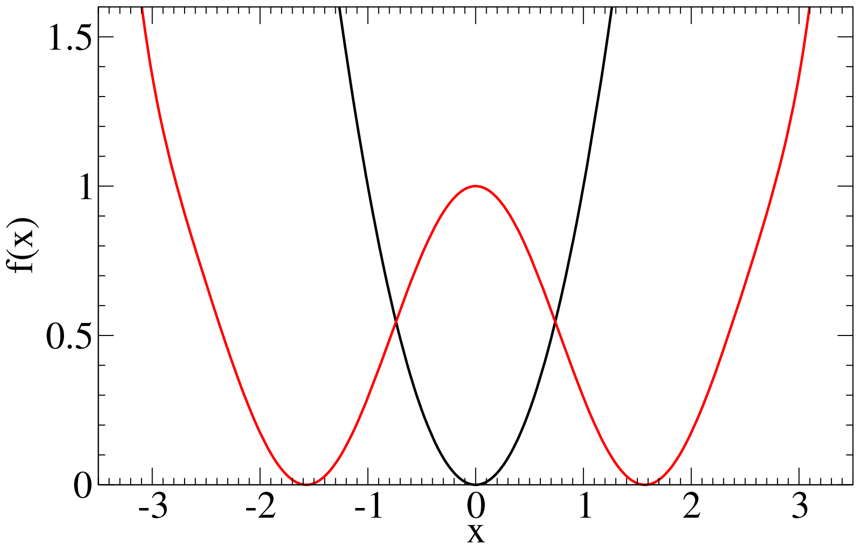

Figure 3.2: A double-well potential (red line) realized from the Taylor expansion of a $\cos^2$-like potential up to the 12^{th} order and an harmonic potential (black line) obtained by Taylor expanding a $\sin^2$-like lattice up to the second order along the x direction.

with

$$\hat{\mathrm{H}}_{\text{c.m.}}(\mathbf{R}) = \hat{\mathrm{T}}_{\text{kin}}(\mathbf{R}) + \hat{\mathrm{V}}_{\text{c.m.}}(\mathbf{R})\,, \tag{3.11}$$

$$\hat{\mathrm{h}}_{\text{rel.}}(\mathbf{r}) = \hat{\mathrm{t}}_{\text{kin}}(\mathbf{r}) + \hat{\mathrm{v}}_{\text{rel.}}(\mathbf{r}) + \hat{\mathrm{U}}_{\text{int}}(\mathbf{r})\,. \tag{3.12}$$

Here, $\hat{\mathrm{T}}_{\text{kin}}$ and $\hat{\mathrm{t}}_{\text{kin}}$ denote the kinetic-energy operators of the c.m. and the relative motion coordinates, respectively. The formulation of the problem in the c.m. and rel.-motion coordinates and the Taylor expansion of the OL potential means that all the separable terms of the OL are contained in the c.m. and rel. Hamiltonian (3.11) and (3.12), respectively. The nonseparable terms represented by the products of the c.m. and rel.-motion coordinates are contained in the coupling term $\hat{\mathrm{W}}$. The main achievement of recasting the problem to the c.m.-rel.-motion coordinates is that realistic interatomic interaction potential can be used to describe the interaction $\hat{\mathrm{U}}_{\text{int}}$.

3.2 Implementation of the method

The stationary solutions of the SE is numerically solved using the procedure introduced by Grishkevich et al. [73]. Within this approach, the Hamiltonian (3.1) is first transformed into the c.m., the rel., and the coupled parts as described above. Resulting Hamiltonians in c.m.-rel. coordinates are transformed to spherical coordinates. The c.m. and the rel. motion wavefunctions are then expressed in basis functions that are products of spherical harmonics for the angular part and B splines for the radial part. In a configuration-interaction (CI) procedure, the eigenfunctions of the c.m. and rel. motions are used to determine the eigenfunctions of the full lattice Hamiltonian (3.10). These steps are outlined in the following.

3.2.1 Orbital calculations

In this stage, called *orbitals* (in analogy to electronic-structure calculations where single-particle wavefunctions are referred to as orbitals), the eigenstates and eigenvalues of the c.m. and the rel. motion Hamiltonians (3.11) and (3.12) are calculated independently by solving numerically the corresponding generalized (due to the nonorthogonality of the B splines) eigenvalue equations

$$\hat{\mathrm{H}}_{\text{c.m.}}|\psi_j\rangle = \epsilon_j^{\text{c.m.}}|\psi_j\rangle \tag{3.13}$$

and

$$\hat{\mathrm{h}}_{\text{rel.}}|\varphi_i\rangle = \epsilon_i^{\text{rel.}}|\varphi_i\rangle\,. \tag{3.14}$$

The eigenfunctions of the c.m. and rel. parts are expressed in a basis of spherical harmonics Y_L^M (Y_l^m) and B splines B_β (B_α) of order $k_{\text{c.m.}}$ ($k_{\text{rel.}}$), i. e., the corresponding eigenfunctions for the c.m. and rel. motions are

$$\psi_j(R,\Theta,\Phi) = \sum_{\beta=1}^{N_R}\sum_{L=0}^{N_L}\sum_{M=-L}^{L} C_{j,\beta LM}\,\frac{B_\beta(R)}{R}\,Y_L^M(\Theta,\Phi) \tag{3.15}$$

and

$$\varphi_i(r,\theta,\phi) = \sum_{\alpha=1}^{N_r}\sum_{l=0}^{N_l}\sum_{m=-l}^{l} C_{i,\alpha lm}\,\frac{B_\alpha(r)}{r}\,Y_l^m(\theta,\phi) \tag{3.16}$$

where N_R (N_r) and N_L (N_l) are the number of B splines and orbital quantum numbers for c.m. (rel.) motions, respectively.

3.2.2 Exact diagonalization

The second step involves using the obtained wavefunctions $\psi(\mathbf{R})$ and $\varphi(\mathbf{r})$ from the c.m. and the rel. motion Schrödinger equations (3.13) and (3.14) to form configuration state functions

$$\Phi_\kappa(\mathbf{R},\mathbf{r}) = \varphi_{i_\kappa}(\mathbf{r})\,\psi_{j_\kappa}(\mathbf{R})\,. \tag{3.17}$$

The stationary SE

$$\hat{\mathrm{H}}\,|\Psi_i\rangle = \mathcal{E}_i\,|\Psi_i\rangle\,, \tag{3.18}$$

with the full Hamiltonian (3.10) is solved by expanding Ψ in terms of the configurations (3.17)

$$\Psi_i(\mathbf{R},\mathbf{r}) = \sum_{\kappa} C_{i,\kappa}\,\Phi_{\kappa}(\mathbf{R},\mathbf{r})\,. \tag{3.19}$$

The configurations (3.19) in spherical c.m.-rel. coordinates are given by the superposition

$$\Psi(r,\theta,\phi,R,\Theta,\Phi) = \sum_{\mathbf{a}}\sum_{\mathbf{b}} \quad {}_{\mathbf{ab}}\,\varphi^{\mathbf{a}}(r,\theta,\phi)\,\psi^{\mathbf{b}}(R,\Theta,\Phi) \tag{3.20}$$

where, the short-hand notations $\mathbf{a} \equiv \alpha, l, m$, $\mathbf{b} \equiv \beta, L, M$, and $\quad_{\mathbf{ab}}$ have been introduced for compactness. $\quad_{\mathbf{ab}}$ denote the expansion coefficients for different configurations.

Inserting the expansion (3.20) into the SE (3.18), then multiplying from the left with Φ^*_{κ}, and integrating over $\mathbf{r}$ and $\mathbf{R}$ yields an ordinary matrix eigenvalue equation

$$\mathbf{H}\mathbf{C}_i = \mathcal{E}_i\,\mathbf{C}_i \tag{3.21}$$

which is then diagonalized in the configuration basis from the products of the eigensolutions of $\hat{\mathrm{h}}_{\mathrm{rel.}}$ and $\hat{\mathrm{H}}_{\mathrm{c.m.}}$. The corresponding matrices for the eigenvalue problems (3.13), (3.14), and (3.21) are given in Appendix C.

B splines have the advantage of being compact in space leading to sparse Hamiltonian matrices and the expansion of the trap in terms of spherical harmonics leads to an analytical form of the matrix elements except those of the numerically defined interatomic interaction.

3.2.3 Symmetry of the system

The Hamiltonian of two atoms confined in an orthorhombic $\sin^2$- or $\cos^2$-type periodic potential is invariant under the symmetry operations of the $\mathrm{D_{2h}}$ point group. The symmetry operations of $\mathrm{D_{2h}}$ are

$$S = \{E,\ C_2(x),\ C_2(y),\ C_2(z),\ \sigma(xy),\ \sigma(xz),\ \sigma(yz),\ \mathbf{i}\} \tag{3.22}$$

where E is the identity, $C_n(\alpha)$ is the rotation about $2\pi/n$ along the α axis $(\alpha = x, y, z)$, $\sigma(\alpha\beta)$ is the reflection on the $\alpha\beta$ plane $(\alpha \neq \beta = x, y, z)$, and $\mathbf{i}$ is the inversion, i. e., point reflection at the origin. These symmetry elements are shown in Figure 3.3.

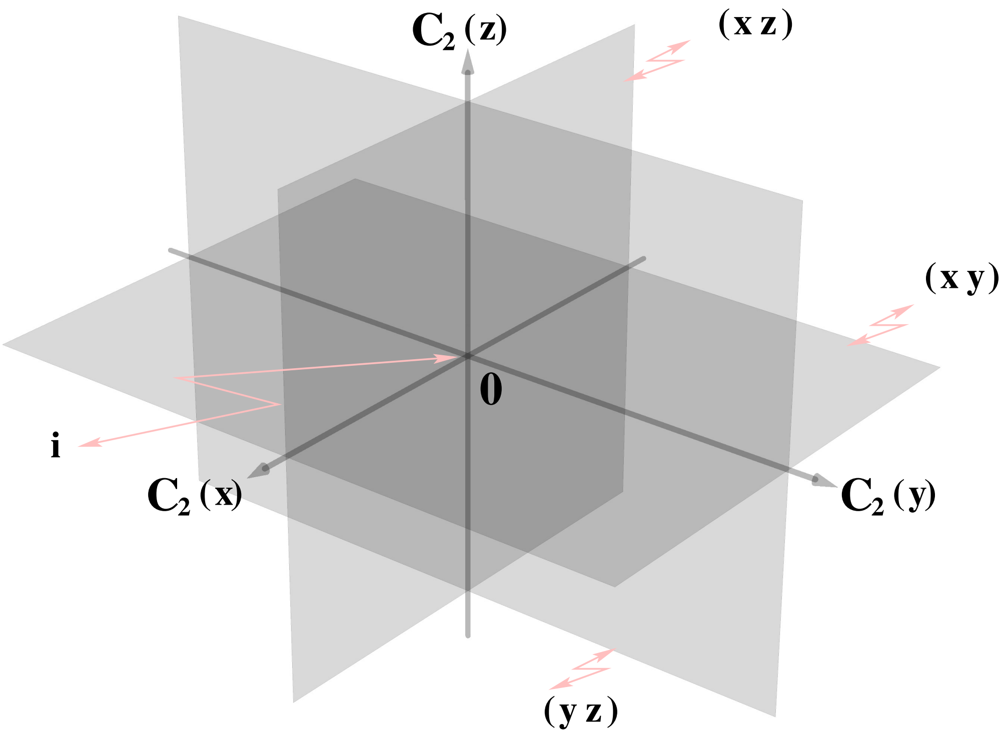

Figure 3.3: The symmetry elements of two particles trapped in a $\sin^2$-like potential interacting via a central potential. The shown operations together with the identity E form the $\mathrm{D_{2h}}$ point group. Figure taken from [73].

The symmetry group $\mathrm{D_{2h}}$ has eight irreducible representations (IRs) Γ^σ with

$$\sigma \in \{A_g,\, B_{1g},\, B_{2g},\, B_{3g},\, A_u,\, B_{1u},\, B_{2u},\, B_{3u}\}\ . \tag{3.23}$$

The character of these IRs are indicated in Table 3.1. Since the terms depending on the radial coordinate are totally symmetric, the symmetry operations affect only the angular part. Therefore, the behavior of the symmetry is determined by the spherical harmonic functions only. Table 3.2 shows the corresponding $\mathrm{D_{2h}}$ group operations on the spherical coordinates together with the corresponding transformations of the spherical harmonics.

The symmetry-adapted basis functions are constructed from the superposition of the spherical harmonics with restrictions on l and m values. A more exhaustive details on the symmetry of the problem is discussed in [73]. Using Tables 3.1 and 3.2, the eight sets of orthonormal linear combination of the spherical harmonics are constructed by projecting the IRs Γ^σ onto the spherical harmonics Y_l^m. The resulting symmetry-adapted basis functions of

Table 3.1: The character table of the symmetry group D_{2h}

D_{2h}	E	$C_2(z)$	$C_2(y)$	$C_2(x)$	$\mathbf{i}$	$\sigma(xy)$	$\sigma(xz)$	$\sigma(yz)$
A_g	1	1	1	1	1	1	1	1
B_{1g}	1	1	-1	-1	1	1	-1	-1
B_{2g}	1	-1	1	-1	1	-1	1	-1
B_{3g}	1	-1	-1	1	1	-1	-1	1
A_u	1	1	1	1	-1	-1	-1	-1
B_{1u}	1	1	-1	-1	-1	-1	1	1
B_{2u}	1	-1	1	-1	-1	1	-1	1
B_{3u}	1	-1	-1	1	-1	1	1	-1

Table 3.2: Results of the D_{2h} group operations on the spherical coordinates together with the corresponding transformations of the spherical harmonics.

Symmetry	Spherical $(\theta' + \theta, \phi' + \phi)$	Y_l^m $Y_l^m(\theta' + \theta, \phi' + \phi)$
E	(θ, ϕ)	$Y_l^m(\theta, \phi)$
$C_2(z)$	$(\theta, \pi + \phi)$	$(-1)^m \, Y_l^m(\theta, \phi)$
$C_2(y)$	$(\pi - \theta, \pi - \phi)$	$(-1)^{l+m} \, Y_l^{-m}(\theta, \phi)$
$C_2(x)$	$(\pi - \theta, 2\pi - \phi)$	$(-1)^l \, Y_l^{-m}(\theta, \phi)$
$\mathbf{i}$	$(\pi - \theta, \pi + \phi)$	$(-1)^l \, Y_l^m(\theta, \phi)$
$\sigma(xy)$	$(\pi - \theta, \phi)$	$(-1)^{l+m} \, Y_l^m(\theta, \phi)$
$\sigma(xz)$	$(\theta, 2\pi - \phi)$	$(-1)^m \, Y_l^{-m}(\theta, \phi)$
$\sigma(yz)$	$(\theta, \pi - \phi)$	$Y_l^{-m}(\theta, \phi)$

the relative motion are

$$\varphi_i^{A_g} = \sum_{\alpha=1}^{N_r} \sum_{l=0,\{2\}}^{N_l} \sum_{m=0,\{2\}}^{l} \tilde{c}_{i,\alpha lm}^{A_g}\, r^{-1}\, B_\alpha(r) \ {}_{lm}^{+} \tag{3.24}$$

$$\varphi_i^{B_{1g}} = \sum_{\alpha=1}^{N_r} \sum_{l=2,\{2\}}^{N_l} \sum_{m=2,\{2\}}^{l} \tilde{c}_{i,\alpha lm}^{B_{1g}}\, r^{-1}\, B_\alpha(r) \ {}_{lm}^{+} \tag{3.25}$$

$$\varphi_i^{B_{2g}} = \sum_{\alpha=1}^{N_r} \sum_{l=2,\{2\}}^{N_l} \sum_{m=1,\{2\}}^{l} \tilde{c}_{i,\alpha lm}^{B_{2g}}\, r^{-1}\, B_\alpha(r) \ {}_{lm}^{-} \tag{3.26}$$

$$\varphi_i^{B_{3g}} = \sum_{\alpha=1}^{N_r} \sum_{l=2,\{2\}}^{N_l} \sum_{m=1,\{2\}}^{l} \tilde{c}_{i,\alpha lm}^{B_{3g}}\, r^{-1}\, B_\alpha(r) \ {}_{lm}^{+} \tag{3.27}$$

$$\varphi_i^{A_u} = \sum_{\alpha=1}^{N_r} \sum_{l=3,\{2\}}^{N_l} \sum_{m=2,\{2\}}^{l} \tilde{c}_{i,\alpha lm}^{A_u}\, r^{-1}\, B_\alpha(r) \ {}_{lm}^{-} \tag{3.28}$$

$$\varphi_i^{B_{1u}} = \sum_{\alpha=1}^{N_r} \sum_{l=1,\{2\}}^{N_l} \sum_{m=0,\{2\}}^{l} \tilde{c}_{i,\alpha lm}^{B_{1u}}\, r^{-1}\, B_\alpha(r) \ {}_{lm}^{+} \tag{3.29}$$

$$\varphi_i^{B_{2u}} = \sum_{\alpha=1}^{N_r} \sum_{l=1,\{2\}}^{N_l} \sum_{m=1,\{2\}}^{l} \tilde{c}_{i,\alpha lm}^{B_{2u}}\, r^{-1}\, B_\alpha(r) \ {}_{lm}^{+} \tag{3.30}$$

$$\varphi_i^{B_{3u}} = \sum_{\alpha=1}^{N_r} \sum_{l=1,\{2\}}^{N_l} \sum_{m=1,\{2\}}^{l} \tilde{c}_{i,\alpha lm}^{B_{3u}}\, r^{-1}\, B_\alpha(r) \ {}_{lm}^{-} \tag{3.31}$$

where the notations

$${}_{l0}^{+} = {}_{l0}^{-} = Y_l^0(\theta,\phi)\,, \tag{3.32}$$

$${}_{lm}^{\pm} = Y_l^m(\theta,\phi) \pm Y_l^{-m}(\theta,\phi) \quad \text{for} \quad m \neq 0 \tag{3.33}$$

are introduced for compactness, the 2 in the curly brackets (e. g., in the summation index $l = i, \{2\}$) means that the index is increasing in steps of two, i. e., $l = i, i+2, \ldots$. The center-of-mass symmetry-adapted basis functions are analogous.

The symmetry-adapted configurations are constructed from the product of the c.m. and the rel. motion orbitals. The product Table 3.3 shows how the c.m. and rel. functions can be selectively combined to form a configuration of desired symmetry, for example, a configuration with B_{3g} can be formed by the product $\varphi_{i_\kappa}^{B_{2g}} \psi_{j_\kappa}^{B_{1g}}$. When considering identical bosons (fermions), the rel. motion wavefunction has to be symmetric (antisymmetric) under inversion $\mathbf{i}$, i. e., all gerade (ungerade) basis functions $\sigma \in \{A_g, B_{1g}, B_{2g}, B_{3g}\}$ ($\sigma \in \{A_u, B_{1u}, B_{2u}, B_{3u}\}$) are allowed for identical bosons (fermions).

The symmetry considerations reduce the computational efforts drastically. The eight IRs can be treated independently of each other leading to a reduction

Table 3.3: Product table of the $\mathrm{D_{2h}}$ point group

$\otimes$	A_g	B_{1g}	B_{2g}	B_{3g}	A_u	B_{1u}	B_{2u}	B_{3u}
A_g	A_g	B_{1g}	B_{2g}	B_{3g}	A_u	B_{1u}	B_{2u}	B_{3u}
B_{1g}	B_{1g}	A_g	B_{3g}	B_{2g}	B_{1u}	A_u	B_{3u}	B_{2u}
B_{2g}	B_{2g}	B_{3g}	A_g	B_{1g}	B_{2u}	B_{3u}	A_u	B_{1u}
B_{3g}	B_{3g}	B_{2g}	B_{1g}	A_g	B_{3u}	B_{2u}	B_{1u}	A_u
A_u	A_u	B_{1u}	B_{2u}	B_{3u}	A_g	B_{1g}	B_{2g}	B_{3g}
B_{1u}	B_{1u}	A_u	B_{3u}	B_{2u}	B_{1g}	A_g	B_{3g}	B_{2g}
B_{2u}	B_{2u}	B_{3u}	A_u	B_{1u}	B_{2g}	B_{3g}	A_g	B_{1g}
B_{3u}	B_{3u}	B_{2u}	B_{1u}	A_u	B_{3g}	B_{2g}	B_{1g}	A_g

of the size of the matrices to be diagonalized by a factor of approximately 64. The possibility of the particle indistinguishability that is accounted for by the symmetry considerations also reduces the number of possible orbital combinations by a factor of two in the case of indistinguishable atoms. For identical bosons or fermions, often not all the symmetries have to be considered leading to a further reduction of the numerical efforts.

Finally, a recent extension of the program allows for the restriction of m quantum numbers in the spherical harmonics basis Y_l^m instead of using the full m space in the expansion of the wavefunctions in equations (3.15) and (3.16). This implementation[1] dramatically reduces the computation requirements in objects with spherical symmetry and in systems of low dimensions, e.g., in quasi-1D systems where the preferred direction is along the z axis. A system with strong anisotropy along an axis requires a large number of spherical harmonics to describe. However, if the anisotropy is along the z direction, then spherical harmonics with $m < l$ are sufficient. This way, m quantum number runs up to a maximum value $m_{\max}$ and not l. When all spherical harmonics are used ($m_{\max} = l$), the basis size increases quadratically with l, however, with the m restriction, the basis size increases only linearly with l with the slope defined by $m_{\max}$.

---

[1] Extra information on the implementation of the m quantum numbers for the program is given in Chapter 4 of the M.Sc thesis of Bruno Schulz [114] (thesis written in German).

3.3 Description of the codes

The stationary Schrödinger equation with the full Hamiltonian (3.10) is solved using the program `TwoAtInOL` of the AMO group at the Institute of Physics, Humboldt-University of Berlin. The code `TwoAtInOL` has two main subcodes. The *orbital* and the *configuration* codes. The orbital code solves the Schrödinger equations for the separable parts of the Hamiltonian while the configuration code solves the problem with the full Hamiltonian using configurations built from the eigenvectors of the c.m. and rel. motions. The details of each of the calculations is provided in the following.

3.3.1 Orbital calculations

The first stage called *orbital calculations* involves solving the Schrödinger equations for the separable parts of the Hamiltonians (3.13) and (3.14). This is performed using the code `otagsd2hm`. This code is run by supplying input files for the basis, the interatomic interaction potential, and the trap potentials. The basis file contains the information about the number and order of B splines as well as their knot sequence, and the upper limits of angular momentum in the spherical harmonic expansions in equations (3.15) and (3.16). The order and type of knot sequence of the B splines determine the density of the basis functions within a given range. The implementation of the code allow for linear distributions, geometric distributions, or certain combination of both. An example sample basis file is given in Appendix D.1.1.

The parameters contained in the trap-potential file include the polarizability of the trapped atoms, the wavelength, and the intensity of the laser fields forming the OL potential. In the original program, both ultracold atoms were trapped in optical lattices formed by the same standing laser fields, however, the code was modified to allow for the simulation of atomic traps with a more general anharmonic potential (not just a $\sin^2$ or a $\cos^2$) and it is this version that is used in the present case. The Taylor expansion coefficients appearing in equations (3.6) - (3.8) are calculated for each particle. This way, it is possible to realize e. g., OL traps for each particle with different polarizability, intensity and wavelength. The general format and an example sample of the generic trap input is given in Appendix D.1.2. The interaction potential is generally known numerically but other potentials, e. g., a square-well potential can also be used with the code provided the choice of the knot sequence for the B splines are distributed such that the discontinuities of the square-well potential are resolved by the basis function.

An example of orbital calculation for two identical noninteracting ^{7}Li atoms confined in isotropic harmonic trap potentials at a frequency of $2\,\pi \times 22$ kHz in

x, y, and z directions is given in Appendix D.1.3. The harmonic trap potential is obtained by Taylor expanding the $\sin^2$ potential (3.2) up to the second order. When interaction is included, the B splines for the relative motion wavefunction can be described by a combination of linear and geometric knot sequence. A linear knot sequence can be used to represent the highly oscillatory interaction range region and an ascending geometric progression sequence for the remaining region.

3.3.2 Configuration interaction calculations

The second step entails using the eigenvectors ψ and φ from the orbital calculation to build the configurations (3.17). This is done using the configuration interaction (CI) code `citaold2hm`. Here, the active orbitals for the center-of-mass and relative-motions required to form particular symmetry-adapted configuration according to the product Table 3.3 of the $\mathrm{D_{2h}}$ is specified. A sample of configuration input file for the orbital calculation example given in Appendix D.1.3 is found in Appendix D.2.1. In this example, the A_g symmetry-adapted configuration is formed from the product $\varphi_{i_\kappa}^{A_g}\psi_{j_\kappa}^{A_g}$. In this particular example, the coupling term $\hat{\mathrm{W}}$ is zero, hence, sufficiently converged CI calculations were found by using only 10 orbitals each for the rel. and center-of-mass (see Appendix D.2.2). However, if a coupling between the center-of-mass and relative motions is present, the convergence depends on the strength of the coupling.

3.4 Convergence study

In order to explore the numerical stability of the code in the case of different trap frequencies which is typical of atom-ion experiments where the ion is tightly trapped compared to the neutral atom, a case of two noninteracting particles in an isotropic harmonic confinement is considered. For this particular system, the eigenvalues are the usual 3D-harmonic oscillator states in spherical coordinates given by $\mathrm{E} = (k + 3/2)\ \ \omega$, where $k \equiv 2n + l$ with the degeneracy of eigenstate k being $(k + 2)(k + 4)/8$. For the A_g symmetry considered here, k takes only even values $k = 0,\ 2,\ 4, \ldots$. The trap potential in c.m.-rel. coordinates is given by

$$V_{\mathrm{ho}} = \omega_{\mathrm{rel.}} r^2 + \Omega_{\mathrm{c.m.}} R^2 + W_{\mathrm{Rr}} R r \tag{3.34}$$

where the coefficients

$$\Omega_{\text{c.m.}} = \sqrt{\frac{m_1}{2}\omega_1^2 + \frac{m_2}{2}\omega_2^2}\,, \tag{3.35}$$

$$\omega_{\text{rel.}} = \sqrt{\frac{m_2\,\omega_1^2 + m_1\,\omega_2^2}{m_1 + m_2}}\,, \tag{3.36}$$

$$W_{\text{Rr}} = \mu(\omega_1^2 - \omega_2^2)\,. \tag{3.37}$$

$\Omega_{\text{c.m.}}$ and $\omega_{\text{rel.}}$ denote the c.m. and rel. frequencies, respectively, and W_{Rr} is the coupling coefficient. In the case when the two frequencies $\omega_1 = \omega_2$, the coupling is zero, otherwise, the coupling is non-zero whenever $\omega_1 \neq \omega_2$. This is true for physical cases of distinguishable particles or indistinguishable particles in different quantum states.

The present convergence study is performed in relation to the difference between the harmonic trap frequencies of the two particles. The exact ground state energy for each frequency ratio ω_2/ω_1 is compared with the results obtained by varying the number of configurations in the CI calculation shown in Tables 3.4 - 3.9. Since the frequencies are different, a coupling between the c.m. and the rel. motions exists. In order to account for this coupling, all symmetries have to be considered while forming the CI expansion. In each calculation, an equal number of active c.m. and rel. orbitals have been used to build the configurations as indicated in the first columns of the tables. The adopted notation is understood as follows. For a given number N of active orbitals, the configurations are built from $N/2$ relative and $N/2$ center-of-mass orbitals. In all the cases considered, B splines of order eight distributed in a linear knot sequence covering the entire box range have been used. The convergence for the lowest-lying 10 energy levels of the orbital calculations using the specified basis sets for each ratio is achieved within at least 10 significant digits. Furthermore, the ground state energies of the orbitals are converged up to 14 decimal places.

In general, the numerical demands increase with an increase in the ratio ω_2/ω_1 between the two traps. This is because the strength of the coupled Hamiltonian matrices become much larger with the increase in the c.m.-rel. coupling due to the difference in the two frequencies. Table 3.5 presents the ground-state energy of two particles when their trapping frequencies differ by a factor of two. In this case, the coupling is about 0.154 ω_{rel}. Using 80 rel. and 80 c.m. orbitals to build the CI configurations, the ground-state energy deviates from the exact value by about $4.80474 \times 10^{-4}\,\%$. Increasing the CI basis size by including more c.m. and rel. orbitals leads to an improved convergence as can be seen when 480 rel. and 480 c.m. orbitals are used. However, this large basis increases the computation demands drastically, the CI vector length for this case is in the order of 28800 and the required memory to store the matrix is 4.7GB.

Table 3.4: Total energy for the ground state of two identical particles in an isotropic trapping potentials with $\omega_2 = 1.4\,\omega_1$, computed with different numbers of configurations. A box size of $\sqrt{3} \times 10000\,a_0$ was used with 116 and 112 B splines for rel. and c.m. orbitals, respectively. The spherical harmonics are expanded up to $l = m = 8$.

No. of active orbitals (rel. & c.m.)	$E_{\text{numerical}}$ ($\omega_{\text{rel.}}$)	% error
160	2.95918177291824	4.80474×10^{-8}
320	2.95918177149732	3.00744×10^{-11}
480	2.95918177149666	7.77371×10^{-12}
640	2.95918177149646	1.02049×10^{-12}
Exact	2.95918177149643	

Table 3.5: Same as Table 3.4 with $\omega_2 = 2\,\omega_1$. Box size = $\sqrt{3} \times 10000\,a_0$, $l = m = 8$, number of B splines: rel. = 178 c.m. = 156.

No. of active orbitals (rel. & c.m.)	$E_{\text{numerical}}$ ($\omega_{\text{rel.}}$)	% error
160	2.84605544840627	1.95157×10^{-4}
320	2.84604995245749	2.04866×10^{-6}
480	2.84604991284280	6.56744×10^{-7}
640	2.84604989454073	1.36747×10^{-8}
800	2.84604989416138	3.45731×10^{-10}
960	2.84604989415934	2.74063×10^{-10}
Exact	2.84604989415154	

The computation time is about 23 hours using one processor of a computer with 256GB of memory. This duration initially appears to be a small amount of time, but when one has to calculate an energy spectrum that typically consists of a number of individual calculations (typically about 100) the total duration and storage can be enormous. Table 3.6 shows a calculation when the two frequencies still differ by a factor of two but with a larger basis set. The orbital calculations are performed using spherical harmonics up to $l = m = 20$. Again this leads to an improved accuracy especially for higher-lying states, the first 100 states are converged to at least 13 significant digits. However, the energy of the first few trap states for $l = m = 8$ and $l = m = 20$ are the same. The difference in the numerical values between the CI energy of the ground state for the two calculations is however not huge for the same basis specification.

Table 3.6: Same as Table 3.4 with $\omega_2 = 2\,\omega_1$. Box size $= \sqrt{3} \times 10000\,a_0$, $l = m = 20$, number of B splines: rel. = 142 c.m. = 134.

No. of active orbitals (rel. & c.m.)	$E_{\text{numerical}}$ ($\omega_{\text{rel.}}$)	% error
160	2.84605544840627	1.95157×10^{-4}
320	2.84604995245689	2.04864×10^{-6}
480	2.84604991619802	7.74634×10^{-7}
640	2.84604989458938	1.53841×10^{-8}
800	2.84604989430111	5.25534×10^{-9}
960	2.84604989415666	1.79895×10^{-10}
Exact	2.84604989415154	

Table 3.7: Same as Table 3.4 with $\omega_2 = 5\,\omega_1$. Box size $= \sqrt{3} \times 8000\,a_0$, $l = m = 10$, number of B splines: rel. = 139 c.m. = 134.

No. of active orbitals (rel. & c.m.)	$E_{\text{numerical}}$ ($\omega_{\text{rel.}}$)	% error
160	2.50819578144978	4.82539×10^{-1}
320	2.49879510314456	1.05932×10^{-1}
480	2.49846125612169	9.25574×10^{-2}
640	2.49662677548041	1.90651×10^{-2}
800	2.49624053760155	3.59171×10^{-3}
960	2.49623039329331	3.18532×10^{-3}
Exact	2.49615088301353	

Table 3.8: Same as Table 3.4 with $\omega_2 = 10\,\omega_1$. Box size $= \sqrt{3} \times 10000\,a_0$, $l = m = 10$, number of B splines: rel. = 178 c.m. = 156.

No. of active orbitals (rel. & c.m.)	$E_{\text{numerical}}$ ($\omega_{\text{rel.}}$)	% error
320	2.35336239296042	1.35625
480	2.35273077948814	1.32905
640	2.33716592002395	6.58694×10^{-1}
800	2.33596893148222	6.07141×10^{-1}
960	2.32910757073461	3.11631×10^{-1}
Exact	2.32187189760996	

Table 3.9: Same as Table 3.4 with $\omega_2 = 100\,\omega_1$. Box size $= \sqrt{3} \times 2000\,a_0$, $l = m = 10$, number of B splines: rel. = 164 c.m. = 109.

No. of active orbitals (rel. & c.m.)	$E_{\text{numerical}}$ ($\omega_{\text{rel.}}$)	% error
320	2.28666527996175	6.73250
480	2.28029321190800	6.43508
640	2.25502301914193	5.25556
800	2.23364633916061	4.25778
960	2.22896130272769	4.03911
Exact	2.14242642835172	

For a large frequency difference, i.e., $\omega_2 = 100\,\omega_1$, the c.m. and rel. become strongly coupled with a coupling of about 0.858 ω_{rel}. Increasing the basis size does not lead to a drastic improvement in the accuracy. An analysis of the wavefunctions in the c.m. and rel. coordinates can be used to visualize the distribution of the wavefunction along the c.m. and rel. axes. Figure 3.4 shows the contour plot of the wavefunction for the frequency ratio ω_2/ω_1 equal to 1, 2, 5, and 10. As the ratio between the frequencies of the two traps increases, the wavefunction turns around the center and becomes more localized. This is due to the increase in the c.m. and rel. frequencies making the trap walls tighter. A larger ratio of $\omega_2/\omega_1 = 1000$ has a coupling of about 0.878 $\omega_{\text{rel.}}$ and the CI calculation would demand more computer memory and computation time. In the present case, it was not possible to obtain improved accuracy with these extreme frequency differences between the two traps. Finally, it should be remarked that an orbital calculation is generally not very demanding compared to a CI calculation if coupling has to be accounted for. The ability to restrict the m quantum number in the spherical-harmonic expansion allows for the study of anisotropic cases provided the ratio between the two traps is not large.

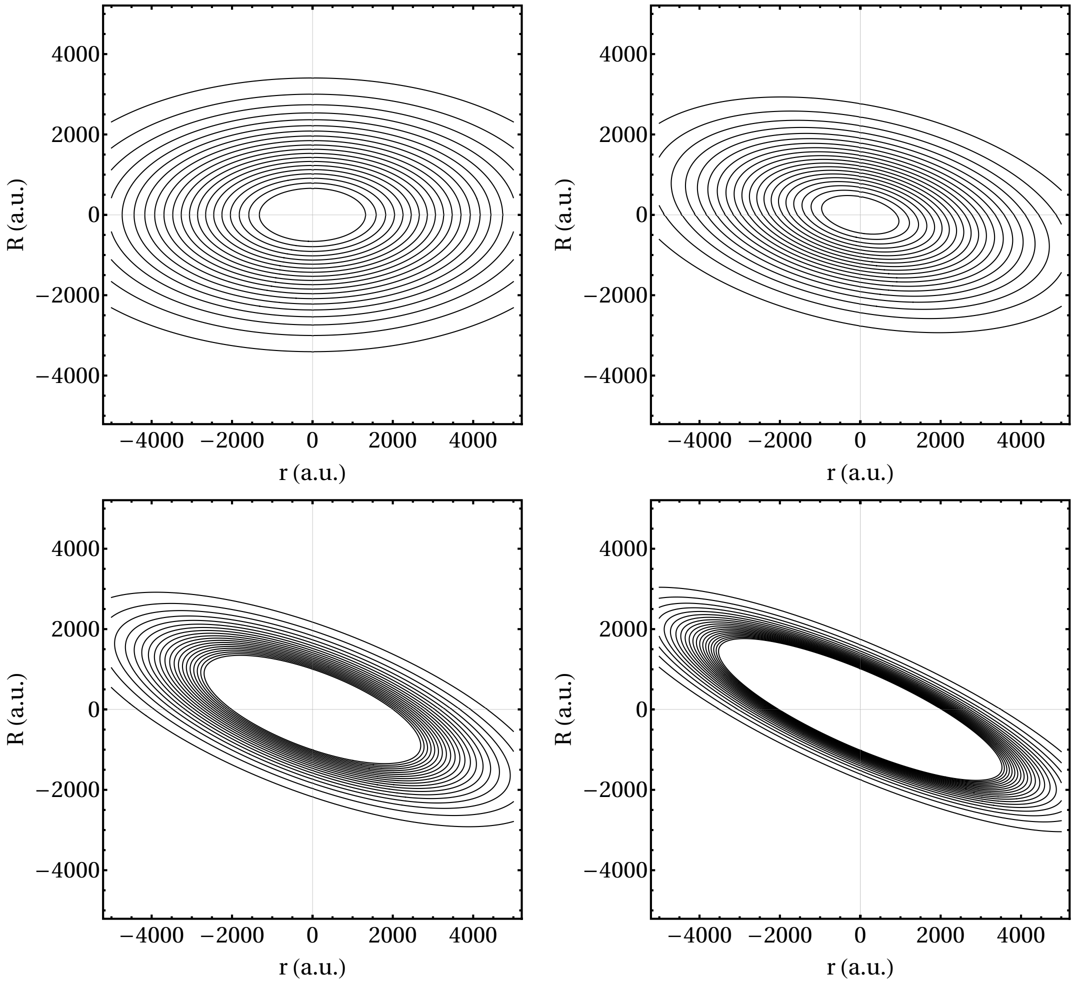

Figure 3.4: Contour plots of the wavefunction in center-of-mass and relative-motion coordinates for two ^{7}Li atoms in a harmonic trap potential when the ratio ω_2/ω_1 is 1 (top left), 2 (top right), 5 (bottom left), and 10 (bottom right).

Chapter 4

Description of Two Particles in Spatially Displaced Traps

In this chapter, a theoretical method for describing two particles that are confined in spatially separated traps while interacting via realistic central (isotropic) potential is presented. The approach outlined here is an extension of the previous model detailed in [73] which has been introduced in Chapter 3. The implementation to incorporate the spatial displacement of the trap potentials is an essential methodological component of the present study. The extension makes it possible to vary the position of the minimum of one of the traps with respect to each other. The remainder of the chapter is organized as follows. In section 4.1, the two-particle Hamiltonian is introduced. In particular, the description of the trapping potential within the center-of-mass and relative-motion coordinates together with the Taylor expansion of the trap potential is presented in section 4.1.1, then the transformation of the final form of the trap potentials to spherical coordinates is given in section 4.1.2. The matrix elements of the trap potentials to be calculated are presented in section 4.1.3. The implementation of symmetry into the method is described in section 4.2 and a discussion on the influence of the trap displacement term on the center-of-mass and relative-motion trap potentials is given in section 4.3. In section 4.4, the check of the implementation of the method is given using an example of two noninteracting particles in separated harmonic traps. The chapter ends with a brief summary in section 4.5.

4.1 Hamiltonian

The Hamiltonian describing two interacting particles confined in separated trap potentials that are located at positions $\mathbf{d}_1$ and $\mathbf{d}_2$, respectively, is given by

$$\hat{\mathrm{H}}(\mathbf{r}_1, \mathbf{r}_2) = \hat{\mathrm{T}}_1(\mathbf{r}_1) + \hat{\mathrm{T}}_2(\mathbf{r}_2) + \hat{\mathrm{V}}_{\mathrm{trap},1}(\mathbf{r}_1 - \mathbf{d}_1) + \hat{\mathrm{V}}_{\mathrm{trap},2}(\mathbf{r}_2 - \mathbf{d}_2) + \hat{\mathrm{U}}(|\mathbf{r}_1 - \mathbf{r}_2|) \quad (4.1)$$

where $\hat{\mathrm{T}}_s$ and $\hat{\mathrm{V}}_{\mathrm{trap},s}$ with $s = 1, 2$ are the respective kinetic energy operators and trapping potentials for the two particles. The last term $\hat{\mathrm{U}}(|\mathbf{r}_1 - \mathbf{r}_2|)$ is the interparticle interaction potential. Note that the Hamiltonian equation (4.1) reduces to that given in (3.1) when $\mathbf{d}_1 = \mathbf{d}_2 = 0$.

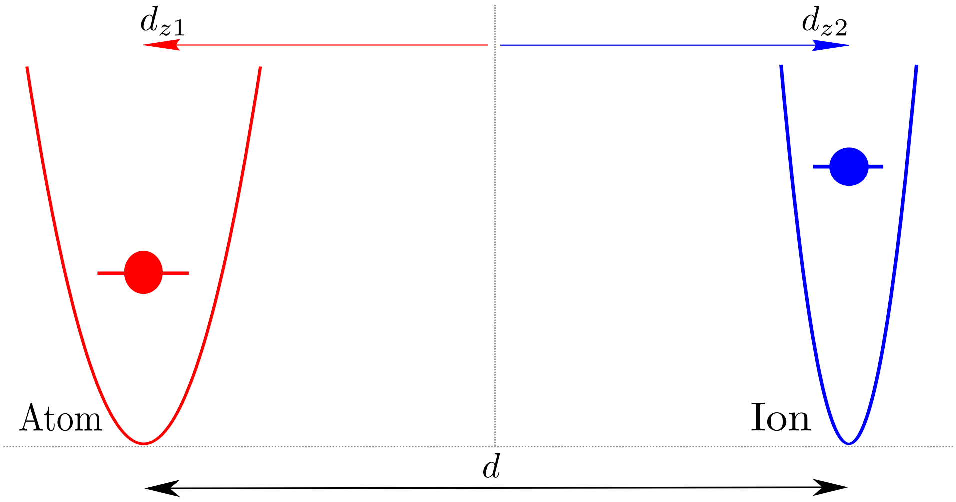

Figure 4.1: Schematic representation of two one-dimensional harmonic-trap potentials for an atom and an ion located at points d_{z1} and d_{z2}, respectively, and the centers of the traps are separated by a distance d along the z direction.

The trapping potential for two spatially separated[1] traps can be modeled from a periodic $\sin^2$-like potential of the form

$$\hat{\mathrm{V}}^{\sin}_{\mathrm{trap},s}(\mathbf{r}_s) = \sum_{s=1}^{2} \sum_{c=x,y,z} V_c^{(s)} \sin^2\{k_c\,[c_s + (-1)^{s-1} d_{c\,s}]\} \tag{4.2}$$

where $k_c = 2\pi/\lambda_c$ is the wave vector associated with the wavelength λ_c of the laser creating the potential along coordinate $c = x, y$, and z. $V_c^{(s)} = I_c^{(s)}\alpha_s$ is the potential depth with $I_c^{(s)}$ being the laser intensity in c direction and α_s is the polarizability of particle s. The traps are located at positions $\mathbf{d}_{c1}$ and $\mathbf{d}_{c2}$ along the x, y, and z spatial coordinates with the separation vector between them being defined as $\mathbf{d} = \mathbf{d}_{c2} - \mathbf{d}_{c1}$. A schematic illustration of two separated (harmonic) traps along the z direction is shown in Figure 4.1. Here, the following convention is adopted. Whenever the distance between the two traps is zero ($d = 0$), then both traps will be located at the origin, otherwise, the first trap, $\hat{\mathrm{V}}_{\mathrm{trap},1}$, will always be on the left of the second trap, $\hat{\mathrm{V}}_{\mathrm{trap},2}$. This convention (enforced by the condition $(-1)^{s-1}$) ensures that both traps are actually located at different points along c for all $d \neq 0$ and not just displaced to the same point from the origin. It is important to remind that when both traps are located at the origin, then the description of the problem follows the discussions given in the preceding chapter.

---

[1] Separation here refers to the distance between the centers of the trap minima. For example, in Figure 4.1, the separation distance is the length d.

Equation (4.2) is essentially an OL potential already discussed in the previous chapters. In order to use the theoretical model in [73] to describe two particles whose Hamiltonian is given by equation (4.1) with the trap potential (4.2), similar steps are followed, i. e., the Hamiltonian is transformed from the absolute Cartesian coordinates to the center-of-mass and relative-motion frame. The trap potential equation (4.2) is Taylor expanded around the minima of the trap centers unlike in the original model where the expansion is performed around the origin where both traps are located. The resulting Hamiltonian will then have parts that depend on the center-of-mass, relative coordinates, and a coupled part. The Hamiltonians in the center-of-mass and relative-motion coordinates are then transformed to spherical coordinates, then the Schrödinger equations for the c.m. and rel. motion Hamiltonians are independently solved and their solutions used to form configurations for solving the SE with the full Hamiltonian that include the coupling part. In the following, the Taylor expansion of the trap potential (4.2) in c.m. and rel.-motion coordinates is discussed.

4.1.1 Taylor expansion of trap potential

Using equations (3.3) and (3.4), the trap potential (4.2) in c.m.-rel.-motion coordinates frame becomes

$$\hat{\mathrm{V}}^{\sin}(\mathbf{R},\mathbf{r}) = \sum_{s=1}^{2} \sum_{c=x,y,z} V_c^s \sin^2\{k_c[R_c + (-1)^s(\mu_{\eta_s} r_c) + (-1)^{s-1} d_{c\,s}]\} \tag{4.3}$$

where $\eta_s = s + (-1)^{s-1}$. Clearly, the new coordinates complicate the expression for the trap potential since the original separability in absolute Cartesian coordinates is lost. This is the price to pay in order to be able to describe the interaction between the two particles using realistic interatomic interaction potentials. It turns out that some separation within the c.m.-rel. frame is achievable by performing a Taylor series expansion of equation (4.3) around the minimum of the trap centers i. e., at $R_c = r_c = (-1)^s d_{c\,s}$.

Restricting the Taylor expansion to the order $2n$ with $n = 1, 2, 3, ...$, and using the relation

$$\begin{aligned}(r+d)^{2n} &= \sum_{n'=0}^{2n} \binom{2n}{n'} r^{n'} d^{2n-n'} \\ &= \sum_{n'=1}^{n} \frac{(2n)!\, d^{(2n-2n'+1)}}{(2n'-1)!\,(2n-2n'+1)!} r^{2n'-1} \\ &\quad + \sum_{n'=1}^{n} \frac{(2n)!\, d^{2n-2n'}}{(2n')!\,(2n-2n')!} r^{2n'} + d^{2n}\end{aligned} \tag{4.4}$$

from the binomial theorem, the terms of the Taylor approximated trap potential (4.3) can be separated into parts containing the constant term from the separation distance, the center-of-mass, the relative-motion, and the nonseparable terms according to

$$\hat{\mathrm{V}}_{\mathrm{trap}}\,(\mathbf{R},\mathbf{r}) = \hat{\mathrm{v}}_0^{\mathrm{sin}} \,+\, \hat{\mathrm{V}}_{\mathrm{c.m.}}^{\mathrm{sin}}(\mathbf{R}) \,+\, \hat{\mathrm{V}}_{\mathrm{rel.}}^{\mathrm{sin}}(\mathbf{r}) \,+\, \hat{\mathrm{W}}^{\mathrm{sin}}(\mathbf{R},\mathbf{r})\,. \tag{4.5}$$

Specifically, the terms in equation (4.5) are given by

$$\hat{\mathrm{v}}_0^{\mathrm{sin}} \;=\; -\frac{1}{2}\sum_{s=1}^{2}\sum_{c=x,y,z} V_c^s \sum_{n'=1}^{n} (-1)^{n'}\,\frac{(2k_{c\,s})^{2n'}(d_{c\,s})^{2n'}}{(2n')!}\,, \tag{4.6}$$

$$\hat{\mathrm{V}}_{\mathrm{c.m.}}^{\mathrm{sin}}(\mathbf{R}) \;=\; -\frac{1}{2}\sum_{s=1}^{2}\sum_{c=x,y,z} V_c^s \sum_{k=1}^{n}\left[\;{}^{\mathrm{even}}_{0kcs}R_c^{2k} + (-1)^{s-1}\;\;{}^{\mathrm{odd}}_{0kcs}R_c^{2k-1}\right], \tag{4.7}$$

$$\hat{\mathrm{v}}_{\mathrm{rel.}}^{\mathrm{sin}}(\mathbf{r}) \;=\; -\frac{1}{2}\sum_{s=1}^{2}\sum_{c=x,y,z} V_c^s \sum_{t=1}^{n}\left[\;{}^{\mathrm{even}}_{t0cs}r_c^{2t} -\;\;{}^{\mathrm{odd}}_{t0cs}r_c^{2t-1}\right], \tag{4.8}$$

and

$$\begin{aligned}\hat{\mathrm{W}}^{\mathrm{sin}}(\mathbf{R},\mathbf{r}) \;=\;& \frac{1}{2}\sum_{s=1}^{2}\sum_{c=x,y,z} V_c^s\Bigg[(-1)^{s-1}\sum_{j=0}^{n-1}\sum_{i=0}^{n-1-j}\;\;{}_{ijcs}\,R_c^{2i+1}\,r_c^{2j+1}\\ &-\sum_{t=1}^{n}\sum_{k=1}^{n-t}\;\;{}_{tkcs}\,R_c^{2k}\,r_c^{2t} + \sum_{k=1}^{n-1}\sum_{j=0}^{n-1-k}\;\;{}_{kjcs}\,R_c^{2k}\,r_c^{2j+1}\\ &+(-1)^s\sum_{t=1}^{n-1}\sum_{i=0}^{n-1-t}\;\;{}_{itcs}\,R_c^{2i+1}\,r_c^{2t}\Bigg]\,.\end{aligned} \tag{4.9}$$

Equation (4.6) is the constant part of the trap potential arising from the separation distance term. The center-of-mass and relative motion parts of the trap potential are given by equation (4.7) and (4.8), respectively, and equation (4.9) is the coupling part. Other than the constant term $\hat{\mathrm{v}}_0^{\mathrm{sin}}$, the set of equations (4.7) - (4.9) take a similar structure like those given in equations (3.6) - (3.8). The components of the trap potential after the Taylor expansion in the present case compared with those in the original formulation are the extra terms with the odd powers in the c.m. and rel. motion equations (4.7) and (4.8) which are absent when the traps are centered at the origin. The first two terms inside the square bracket (with the coefficients $_{ijcs}$ and $_{tkcs}$) in the expression for the coupling term (4.9) are similar to those in the coupling equation (3.8) without the trap separation except that the coefficients have been modified by the separation distance term (see equations (4.10) - (4.17) below). In these two terms, the products of the center-of-mass and the relative-motion have odd-odd ($R_c^{2i+1}\,r_c^{2j+1}$) and even-even ($R_c^{2k}\,r_c^{2t}$) powers only. After the inclusion of the trap separation, two extra sums arise with products of even c.m. and odd rel. (coefficients given by ${}_{kjcs}$) and even rel. and odd c.m. orders (coefficients given by ${}_{itcs}$). The coefficients of the Taylor expansion appearing in equations (4.7) - (4.9) are defined by

$$ {}^{\text{even}}_{0kcs} = \sum_{n'=1}^{n} (-1)^{n'} \frac{(2k_{c\,s})^{2n'}(d_{c\,s})^{2(n'-k)}}{(2k)!(2n'-2k)!}\,, \tag{4.10}$$

$$ {}^{\text{odd}}_{0kcs} = \sum_{n'=1}^{n} (-1)^{n'} \frac{2^{2n'+1}(k_{c\,s})^{2n'}(d_{c\,s})^{2(n'-k)+1}}{(2k)!(2n'-2k+1)!} k, \tag{4.11}$$

$$ {}^{\text{even}}_{t0cs} = \sum_{n'=1}^{n} (-1)^{n'} \frac{(2k_{c\,s})^{2n'}(d_{c\,s})^{2(n'-t)}}{(2t)!(2n'-2t)!} (\mu_{\eta_s})^{2t}, \tag{4.12}$$

$$ {}^{\text{odd}}_{t0cs} = \sum_{n'=1}^{n} (-1)^{n'} \frac{2^{2n'+1}(k_{c\,s})^{2n'}(d_{c\,s})^{2(n'-t)+1}}{(2t)!(2n'-2t+1)!}\, t\,(\mu_{\eta_s})^{2t-1}, \tag{4.13}$$

$$ {}_{ijcs} = \sum_{n'=1}^{n} (-1)^{n'} \frac{(2k_{c\,s})^{2n'}(d_{c\,s})^{2(n'-i-j-1)}}{(2i+1)!(2j+1)!(2(n'-i-j-1))!} (\mu_{\eta_s})^{2j+1}, \tag{4.14}$$

$$ {}_{tkcs} = \sum_{n'=1}^{n} (-1)^{n'} \frac{(2k_{c\,s})^{2n'}\,(d_{c\,s})^{2(n'-t-k)}}{(2t)!\,(2k)!\,(2(n'-t-k))!}\,(\mu_{\eta_s})^{2t}, \tag{4.15}$$

$$ {}_{kjcs} = \sum_{n'=1}^{n} (-1)^{n'} \frac{(2k_{c\,s})^{2n'}\,(d_{c\,s})^{2(n'-k-j)-1}}{(2k)!\,(2j+1)!\,(2(n'-k-j)-1)!}\,(\mu_{\eta_s})^{2j+1}, \tag{4.16}$$

$$ {}_{itcs} = \sum_{n'=1}^{n} (-1)^{n'} \frac{(2k_{c\,s})^{2n'}\,(d_{c\,s})^{2(n'-i-t)-1}}{(2t)!\,(2i+1)!\,(2(n'-i-t)-1))!}\,(\mu_{\eta_s})^{2t}\,. \tag{4.17}$$

In the numerical implementation, the coefficients (4.10) - (4.17) are calculated for each order of the expansion[2] in the same way described in section 3.2.1.

Similarly, the expression for the alternative $\cos^2$ lattice for the trap potential is given by

$$\hat{\mathrm{V}}^{\cos}_{\text{trap},s}(\mathbf{r}_s) = \sum_{s=1}^{2} \sum_{c=x,y,z} V_c^{(s)} \sin^2\{k_c\,[c_s + (-1)^{s-1} d_{c\,s} + \frac{\pi}{2}]\}\,. \tag{4.18}$$

Transforming equation (4.18) to c.m.-rel.-motion coordinates leads to a splitting into parts containing a constant, center-of-mass, relative motion, and coupled

---

[2] A sample of input file with the expansion coefficients is given in Appendix D.3

terms similar to equations (4.6) - (4.9) but with opposite signs,

$$\hat{\mathrm{v}}_0^{\cos} = \frac{1}{2}\sum_{s=1}^{2}\sum_{c=x,y,z} V_c^s\left[2+\sum_{n'=1}^{n}(-1)^{n'}\frac{(2k_{c\,s})^{2n'}(d_{c\,s})^{2n'}}{(2n')!}\right], \tag{4.19}$$

$$\hat{\mathrm{V}}_{\text{c.m.}}^{\cos}(\mathbf{R}) = \frac{1}{2}\sum_{s=1}^{2}\sum_{c=x,y,z} V_c^s\sum_{k=1}^{n}\left[\ {}^{\text{even}}_{0kcs}R_c^{2k}\ +(-1)^{s-1}\ {}^{\text{odd}}_{0kcs}R_c^{2k-1}\right], \tag{4.20}$$

$$\hat{\mathrm{v}}_{\text{rel.}}^{\cos}(\mathbf{r}) = \frac{1}{2}\sum_{s=1}^{2}\sum_{c=x,y,z} V_c^s\sum_{t=1}^{n}\left[\ {}^{\text{even}}_{t0cs}r_c^{2t}-\ {}^{\text{odd}}_{t0cs}r_c^{2t-1}\right], \tag{4.21}$$

$$\begin{aligned}\hat{\mathrm{W}}^{\cos}(\mathbf{R},\mathbf{r}) = -\frac{1}{2}\sum_{s=1}^{2}\sum_{c=x,y,z} V_c^s\Bigg[&(-1)^{s-1}\sum_{j=0}^{n-1}\sum_{i=0}^{n-1-j}\ {}_{ijcs}\,R_c^{2i+1}\,r_c^{2j+1}\\ &-\sum_{t=1}^{n}\sum_{k=1}^{n-t}\ {}_{tkcs}\,R_c^{2k}\,r_c^{2t}+\sum_{k=1}^{n-1}\sum_{j=0}^{n-1-k}\ {}_{kjcs}\,R_c^{2k}\,r_c^{2j+1}\\ &+(-1)^s\sum_{t=1}^{n-1}\sum_{i=0}^{n-1-t}\ {}_{itcs}\,R_c^{2i+1}\,r_c^{2t}\Bigg].\end{aligned} \tag{4.22}$$

The components of the $\sin^2$ lattice potential (4.2) given by the set of equations (4.6) - (4.9) and those of the $\cos^2$ lattice of equation (4.18) given by equations (4.19) - (4.22) allow for the realization of two traps located at any point along the x, y, and z directions. This modification of the trap potential to include the spatial displacement is an essential achievement of this thesis. The Hamiltonian takes the same form given in equations (3.10) - (3.12), i. e.,

$$\hat{\mathrm{H}}(\mathbf{R},\mathbf{r}) = \hat{\mathrm{H}}_{\text{c.m.}}(\mathbf{R})+\hat{\mathrm{h}}_{\text{rel.}}(\mathbf{r})+\hat{\mathrm{W}}(\mathbf{R},\mathbf{r}) \tag{4.23}$$

where

$$\hat{\mathrm{H}}_{\text{c.m.}}(\mathbf{R}) = \hat{\mathrm{T}}_{\text{kin}}(\mathbf{R})+\hat{\mathrm{V}}_{\text{c.m.}}(\mathbf{R})\,, \tag{4.24}$$

$$\hat{\mathrm{h}}_{\text{rel.}}(\mathbf{r}) = \hat{\mathrm{t}}_{\text{kin}}(\mathbf{r})+\hat{\mathrm{v}}_{\text{rel.}}(\mathbf{r})+\hat{\mathrm{U}}_{\text{int}}(\mathbf{r})\,. \tag{4.25}$$

and the components of the trap potentials $\hat{\mathrm{V}}_{\text{c.m.}}$, $\hat{\mathrm{v}}_{\text{rel.}}(\mathbf{r})$, and $\hat{\mathrm{W}}(\mathbf{R},\mathbf{r})$ are given by equations, (4.7), (4.8), and (4.9), respectively for $\sin^2$-like potentials. For $\cos^2$-like potentials, the corresponding trap components are given by equations (4.20) - (4.22) At this point, the theoretical treatment follows the same procedure described in sections 3.2.1 and 3.2.2 in Chapter 3. In the following section, the transformation of the trap potentials to spherical coordinates is described.

4.1.2 Trap potentials in spherical coordinates

After the shift to the center-of-mass and relative-motion coordinates, the resulting Hamiltonian is transformed to spherical coordinates. The transformation equations from and to Cartesian coordinates are

$$\begin{aligned} x &= r\,\sin\theta\cos\varphi, \\ y &= r\,\sin\theta\sin\varphi, \\ z &= r\,\cos\theta, \end{aligned} \tag{4.26}$$

and

$$\begin{aligned} r &= \sqrt{x^2+y^2+z^2}, \quad 0 \le r, \\ \theta &= \cos^{-1}\left(\frac{z}{\sqrt{x^2+y^2+z^2}}\right), \quad 0 \le \theta \le \pi\,, \\ \phi &= \tan^{-1}\left(\frac{y}{x}\right), \quad 0 \le \varphi \le \pi. \end{aligned} \tag{4.27}$$

The trapping potentials in spherical c.m.-rel.-motion coordinates are modified by the displacement term and take the form

$$\begin{aligned} \hat{\mathrm{V}}(R,\Theta,\Phi) = -\frac{1}{2}\sum_{s=1}^{2}\sum_{c=x,y,z} V_c^s \sum_{k=1}^{n}\Bigg\{ & {}^{\text{even}}_{0kcs} R^{2k} \sum_{L=0,\{2\}}^{2k} \sum_{M=-L,\{2\}}^{L} {}^{c}_{LMk} Y_L^M(\Theta,\Phi) \\ & + {}^{\text{odd}}_{0kcs} R^{2k-1} \sum_{L=1,\{2\}}^{2k-1} \left[\tilde{}\,{}^{c}_{L0k} Y_L^0(\Theta,\Phi) + \sum_{M=-L,\{2\}}^{L} \tilde{}\,{}^{c}_{LMk} Y_L^M(\Theta,\Phi) \right] \Bigg\} \end{aligned} \tag{4.28}$$

and

$$\begin{aligned} \hat{\mathrm{v}}(r,\theta,\phi) = -\frac{1}{2}\sum_{s=1}^{2}\sum_{c=x,y,z} V_c^s \sum_{t=1}^{n}\Bigg\{ & {}^{\text{even}}_{t0cs} r^{2t} \sum_{l=0,\{2\}}^{2t} \sum_{m=-l,\{2\}}^{l} {}^{c}_{lmt} Y_l^m(\theta,\phi) \\ & + {}^{\text{odd}}_{t0cs} r^{2t-1} \sum_{l=1,\{2\}}^{2t-1} \left[\tilde{}\,{}^{c}_{l0t} Y_l^0(\theta,\phi) + \sum_{m=-l,\{2\}}^{l} \tilde{}\,{}^{c}_{lmt} Y_l^m(\theta,\phi) \right] \Bigg\} \end{aligned} \tag{4.29}$$

while the coupling term of the trap potential is given by

$$
\begin{aligned}
&\hat{\mathrm{W}}(R,\Theta,\Phi,r,\theta,\phi) = \\
&\quad \frac{1}{2}\sum_{s=1}^{2}\sum_{c=x,y,z} V_c^s \left(\left\{ (-1)^{s-1} \sum_{j=0}^{n-1}\sum_{i=0}^{n-1-j} {}_{ijcs}R^{2i+1}r^{2j+1} \right.\right. \\
&\quad \times \sum_{L=1,\{2\}}^{2i+1} \left[\tilde{\ }{}^{c}_{L0i}Y_L^0(\Theta,\Phi) + \sum_{M=-L,\{2\}}^{L} \tilde{\ }{}^{c}_{LMi}Y_L^M(\Theta,\Phi) \right] \\
&\quad \left. \times \sum_{l=1,\{2\}}^{2j+1} \left[\tilde{\ }{}^{c}_{l0j}Y_l^0(\theta,\phi) + \sum_{m=-l,\{2\}}^{l} \tilde{\ }{}^{c}_{lmj}Y_l^m(\theta,\phi) \right] \right\} \\
&\quad - \left\{ \sum_{t=1}^{n}\sum_{k=1}^{n-t} {}_{tkcs}R^{2k}r^{2t} \sum_{l=0,\{2\}}^{2t}\sum_{m=-l,\{2\}}^{l} {}^{c}_{lmt}Y_l^m(\theta,\phi) \right. \\
&\quad \left. \times \sum_{L=0,\{2\}}^{2k}\sum_{M=-L,\{2\}}^{L} {}^{c}_{LMk}Y_L^M(\Theta,\Phi) \right\} \\
&\quad + \left\{ \sum_{k=1}^{n-1}\sum_{j=0}^{n-1-k} {}_{kjcs}R^{2k}r^{2j+1} \sum_{L=0,\{2\}}^{2k}\sum_{M=-L,\{2\}}^{L} {}^{c}_{LMk}Y_L^M(\Theta,\Phi) \right. \\
&\quad \left. \times \sum_{L=1,\{2\}}^{2j+1} \left[\tilde{\ }{}^{c}_{L0j}Y_L^0(\Theta,\Phi) + \sum_{M=-L,\{2\}}^{L} \tilde{\ }{}^{c}_{LMj}Y_L^M(\Theta,\Phi) \right] \right\} \\
&\quad + \left\{ \sum_{t=1}^{n-1}\sum_{i=0}^{n-1-t} {}_{itcs}R^{2i+1}r^{2t} \sum_{l=0,\{2\}}^{2t}\sum_{m=-l,\{2\}}^{l} {}^{c}_{lmt}Y_l^m(\theta,\phi) \right. \\
&\quad \left.\left. \times \left[\tilde{\ }{}^{c}_{L0i}Y_L^0(\Theta,\Phi) + \sum_{M=-L,\{2\}}^{L} \tilde{\ }{}^{c}_{LMi}Y_L^M(\Theta,\Phi) \right] \right\} \right). \qquad (4.30)
\end{aligned}
$$

Here, the sums, e. g., $\sum\limits_{l=0,\{2\}}^{2t}$ imply that the index runs in steps of 2, i. e., $\sum\limits_{l=0,2,4,\ldots}^{2t}$. The auxiliary coefficients ${}^{c}_{\alpha\beta\gamma}$ and $\tilde{\ }{}^{c}_{\alpha\beta\gamma}$ arise from the expansion of the OL potential in spherical harmonics. They are calculated in the same way like in the original work in [73] and are given in Appendix B. For all $m \neq 0$, $\tilde{\ }{}^{x}_{l0j} = \tilde{\ }{}^{y}_{l0j} = 0$ and $\tilde{\ }{}^{z}_{lmj} = 0$ in equation (4.30). A similar argument is implied in equations (4.28) and (4.29). After the transformation to c.m.-rel. coordinates and the Taylor expansion of the trap potentials around the trap minima, the full Hamiltonian in spherical c.m. and rel.-motion coordinates take a similar structure like the original model and are written as

$$
\hat{\mathrm{H}}(r,\theta,\phi,R,\Theta,\Phi) = \hat{\mathrm{h}}_{\mathrm{rel.}}(r,\theta,\phi) + \hat{\mathrm{H}}_{\mathrm{c.m.}}(R,\Theta,\Phi) + \hat{\mathrm{W}}(r,\theta,\phi,R,\Theta,\Phi) \qquad (4.31)
$$

where the center-of-mass motion Hamiltonian $\hat{\mathrm{H}}_{\mathrm{c.m.}}$ is given by

$$\hat{\mathrm{H}}_{\mathrm{c.m.}}(R,\Theta,\Phi) = -\frac{1}{2\mathrm{M}}\left[\frac{\partial^2}{\partial R^2} + \frac{2}{R}\frac{\partial}{\partial R} - \frac{\hat{\mathbf{I}}^2_{\mathrm{c.m.}}}{R^2}\right] + \hat{\mathrm{V}}_{\mathrm{c.m.}}(R,\Theta,\Phi) \tag{4.32}$$

and the relative-motion Hamiltonian given by

$$\hat{\mathrm{h}}_{\mathrm{rel.}}(r,\theta,\phi) = -\frac{1}{2\mu}\left[\frac{\partial^2}{\partial r^2} + \frac{2}{r}\frac{\partial}{\partial r} - \frac{\hat{\mathbf{I}}^2_{\mathrm{rel.}}}{r^2}\right] + \hat{\mathrm{v}}_{\mathrm{rel.}}(r,\theta,\phi) + \hat{\mathrm{U}}_{\mathrm{int}}(r)\,. \tag{4.33}$$

The set of equations (4.28) - (4.30) and their corresponding implementation in the original model in Ref. [73] is a central result of the present thesis. The matrix elements to be calculated are described in the following.

4.1.3 Matrix elements

As already pointed out, the new formulation to include the spatial displacement of the traps affects only the trapping potential component of the original model. The matrix elements to be calculated except those of the trap potentials are exactly the same like those without trap separation and are given in Appendix C. Here, the expressions for the matrix elements of the trap potentials after the transformation to spherical coordinates are explicitly given.

The matrix elements of the trap potentials (4.28) and (4.29) are

$$\begin{aligned}
[v_{\mathrm{rel.}}(r,\theta,\phi)]_{\mathbf{a}\,\mathbf{a}'} = -\frac{1}{2}\sum_{s=1}^{2}\sum_{c=\{x,y,z\}} V_c^s \sum_{t=1}^{n}\Bigg\{\Bigg[& {}^{\mathrm{even}}_{t0cs}\;{}^{2t}_{\alpha\,\alpha'}\sum_{l_t=0,\{2\}}^{2t}\;\sum_{m_t=-l_t,\{2\}}^{l_t} \times \\
& {}^{c}_{l_t m_t t}\;{}^{m'}_{l_t l l'}\begin{pmatrix} l_t & l & l' \\ m_t & m & -m' \end{pmatrix}\begin{pmatrix} l_t & l & l' \\ 0 & 0 & 0 \end{pmatrix}\Bigg] \\
& + \Bigg[\;{}^{\mathrm{odd}}_{t0cs}\;{}^{2t-1}_{\alpha\,\alpha'}\sum_{l_t=1,\{2\}}^{2t-1}\Bigg\{\tilde{}\,{}^{c}_{l_t 0 t}\begin{pmatrix} l_t & l & l' \\ 0 & m & m' \end{pmatrix} + \\
& \sum_{m_j=-l_t,\{2\}}^{l_t}\tilde{}\,{}^{c}_{l_t m_t t}\begin{pmatrix} l_t & l & l' \\ m_t & m & -m' \end{pmatrix}\Bigg\}\;{}^{m'}_{l_t l l'}\begin{pmatrix} l_t & l & l' \\ 0 & 0 & 0 \end{pmatrix}\Bigg]\Bigg\}
\end{aligned} \tag{4.34}$$

and

$$
\begin{aligned}
[V_{\text{c.m.}}(R,\Theta,\Phi)]_{\mathbf{b}\,\mathbf{b}'} = -\frac{1}{2}\sum_{s=1}^{2}\sum_{c=\{x,y,z\}} V_c^s \sum_{k=1}^{n} \Bigg\{ \Bigg[\ {}^{\text{even}}_{0kcs} \ {}^{2k}_{\beta\,\beta'} \sum_{L_k=0,\{2\}}^{2k} \sum_{M_k=-L_k,\{2\}}^{L_k} \times \\
{}^{c}_{L_kM_kk} \ {}^{M'}_{L_kLL'} \begin{pmatrix} L_k & L & L' \\ M_k & M & -M' \end{pmatrix} \begin{pmatrix} L_k & L & L' \\ 0 & 0 & 0 \end{pmatrix} \Bigg] \\
+ \Bigg[\ {}^{\text{odd}}_{0kcs} \ {}^{2k-1}_{\beta\,\beta'} \sum_{L_k=1,\{2\}}^{2k-1} \Bigg\{ \tilde{\ }^{c}_{L_k0k} \begin{pmatrix} L_k & L & L' \\ 0 & M & M' \end{pmatrix} + \\
\sum_{M_k=-L_k,\{2\}}^{L_k} \tilde{\ }^{c}_{L_kM_kk} \begin{pmatrix} L_k & L & L' \\ M_k & M & -M' \end{pmatrix} \Bigg\} \ {}^{M'}_{L_kLL'} \begin{pmatrix} L_k & L & L' \\ 0 & 0 & 0 \end{pmatrix} \Bigg] \Bigg\},
\end{aligned}
\tag{4.35}
$$

while the matrix elements that couple the center-of-mass and relative motions are

$$
\hat{\mathrm{W}}_{\kappa,\kappa'} = \frac{1}{2}\sum_{s=1}^{2}\sum_{c=x,y,z} V_c^s \Big[W_{\text{o\_o}} + W_{\text{e\_e}} + W_{\text{e\_o}} + W_{\text{o\_e}} \Big]. \tag{4.36}
$$

The terms in the sum in equation (4.36) are each given by

$$
\begin{aligned}
W_{\text{o\_o}} \ = \ & (-1)^{s-1} \sum_{j=0}^{n-1} \ {}_{ijcs} \sum_{\alpha=2}^{N_r-1} \sum_{l=0}^{N_l} \sum_{m=-l}^{l} \tilde{c}^{\text{rel.}}_{p_\kappa,\mathbf{a}} \sum_{\alpha'=2}^{N_r-1} \sum_{l'=0}^{N_l} \sum_{m'=-l}^{l} \tilde{c}^{\text{rel.}}_{p_{\kappa'},\mathbf{a}'} \ {}^{2j+1}_{\alpha\,\alpha'} \\
& \times \sum_{l_j=1,\{2\}}^{2j+1} \Bigg\{ \Bigg[\tilde{\ }^{c}_{l_j0j} \begin{pmatrix} l_j & l & l' \\ 0 & m & m' \end{pmatrix} + \sum_{m_j=-l_j,\{2\}}^{l_j} \tilde{\ }^{c}_{l_jm_jj} \begin{pmatrix} l_j & l & l' \\ m_j & m & -m' \end{pmatrix} \Bigg] \\
& \times \ {}^{m'}_{l_jll'} \begin{pmatrix} l_j & l & l' \\ 0 & 0 & 0 \end{pmatrix} \Bigg\} \sum_{i=0}^{n-1-j} \sum_{\beta=2}^{N_R-1} \sum_{L=0}^{N_L} \sum_{M=-L}^{L} \tilde{C}^{\text{c.m.}}_{q_\kappa,\mathbf{b}} \sum_{\beta'=2}^{N_R-1} \sum_{L'=0}^{N_L} \sum_{M'=-L'}^{L'} \ {}^{2i+1}_{\beta\,\beta'} \\
& \times \sum_{L_i=1,\{2\}}^{2i+1} \Bigg\{ \Bigg[\tilde{\ }^{c}_{L_i0i} \begin{pmatrix} L_i & L & L' \\ 0 & M & M' \end{pmatrix} + \sum_{M_i=-L_i,\{2\}}^{L_i} \tilde{\ }^{c}_{L_iM_ii} \begin{pmatrix} L_i & L & L' \\ M_i & M & -M' \end{pmatrix} \Bigg] \\
& \times \ {}^{M'}_{L_iLL'} \begin{pmatrix} L_i & L & L' \\ 0 & 0 & 0 \end{pmatrix} \Bigg\},
\end{aligned}
\tag{4.37}
$$

$$\begin{aligned}
W_{\text{e\_e}} &= \sum_{t=1}^{n} \; tkcs \sum_{\alpha=2}^{N_r-1} \sum_{l=0}^{N_l} \sum_{m=-l}^{l} \tilde{c}^{\,\text{rel.}}_{p_\kappa,\mathbf{a}} \sum_{\alpha'=2}^{N_r-1} \sum_{l'=0}^{N_l} \sum_{m'=-l}^{l} \tilde{c}^{\,\text{rel.}}_{p_{\kappa'},\mathbf{a}'} \; {}^{2t}_{\alpha\,\alpha'} \\
&\times \sum_{l_t=0,\{2\}}^{2t} \; \sum_{m_t=-l_t,\{2\}}^{l_t} \; {}^{c}_{l_t m_t t} \; {}^{m'}_{l_t l l'} \begin{pmatrix} l_t & l & l' \\ m_t & m & -m' \end{pmatrix} \begin{pmatrix} l_t & l & l' \\ 0 & 0 & 0 \end{pmatrix} \\
&\times \sum_{k=1}^{n-t} \sum_{\beta=2}^{N_R-1} \sum_{L=0}^{N_L} \sum_{M=-L}^{L} \tilde{C}^{\,\text{c.m.}}_{q_\kappa,\mathbf{b}} \sum_{\beta'=2}^{N_R-1} \sum_{L'=0}^{N_L} \sum_{M'=-L'}^{L'} \tilde{C}^{\,\text{c.m.}}_{q_{\kappa'},\mathbf{b}'} \; {}^{2k}_{\beta\,\beta'} \\
&\times \sum_{L_k=0,\{2\}}^{2k} \; \sum_{M_k=-L_k,\{2\}}^{L_k} \; {}^{c}_{L_k M_k k} \; {}^{M'}_{L_k L L'} \begin{pmatrix} L_k & L & L' \\ M_k & M & -M' \end{pmatrix} \begin{pmatrix} L_k & L & L' \\ 0 & 0 & 0 \end{pmatrix},
\end{aligned} \tag{4.38}$$

$$\begin{aligned}
W_{\text{e\_o}} &= \sum_{k=1}^{n-1} \; kjcs \sum_{\beta=2}^{N_R-1} \sum_{L=0}^{N_L} \sum_{M=-L}^{L} \tilde{C}^{\,\text{c.m.}}_{q_\kappa,\mathbf{b}} \sum_{\beta'=2}^{N_R-1} \sum_{L'=0}^{N_L} \sum_{M'=-L}^{L} \tilde{C}^{\,\text{c.m.}}_{q_{\kappa'},\mathbf{b}'} \; {}^{2k}_{\beta\,\beta'} \\
&\times \sum_{L_k=0,\{2\}}^{2k} \; \sum_{M_k=-L_k,\{2\}}^{L_k} \; {}^{c}_{L_k M_k k} \; {}^{M'}_{L_k L L'} \begin{pmatrix} L_k & L & L' \\ M_k & M & -M' \end{pmatrix} \begin{pmatrix} L_k & L & L' \\ 0 & 0 & 0 \end{pmatrix} \\
&\times \sum_{j=0}^{n-1-k} \; \sum_{\alpha=2}^{N_r-1} \sum_{l=0}^{N_l} \sum_{m=-l}^{l} \tilde{c}^{\,\text{rel.}}_{p_\kappa,\mathbf{a}} \sum_{\alpha'=2}^{N_r-1} \sum_{l'=0}^{N_l} \sum_{m'=-l'}^{l'} \tilde{c}^{\,\text{rel.}}_{p_{\kappa'},\mathbf{a}'} \; {}^{2j+1}_{\alpha,\alpha'} \\
&\times \sum_{l_j=1,\{2\}}^{2j+1} \left\{ \left[\tilde{}\;{}^{c}_{l_j 0 j} \begin{pmatrix} l_j & l & l' \\ 0 & m & m' \end{pmatrix} + \sum_{m_j=-l_j,\{2\}}^{l_j} \tilde{}\;{}^{c}_{l_j m_j j} \begin{pmatrix} l_j & l & l' \\ m_j & m & -m' \end{pmatrix} \right] \right. \\
&\times \left. {}^{m'}_{l_j l l'} \begin{pmatrix} l_j & l & l' \\ 0 & 0 & 0 \end{pmatrix} \right\},
\end{aligned} \tag{4.39}$$

$$
\begin{aligned}
W_{\text{o\_e}} \;=\; & (-1)^{s} \sum_{t=1}^{n-1} \; itcs \sum_{\alpha=2}^{N_r-1} \sum_{l=0}^{N_l} \sum_{m=-l}^{l} \tilde{c}^{\,\text{rel.}}_{p_\kappa,\mathbf{a}} \sum_{\alpha'=2}^{N_r-1} \sum_{l'=0}^{n_l} \sum_{m'=-l}^{l} \tilde{c}^{\,\text{rel.}}_{p_{\kappa'},\mathbf{a}'} \; {}^{2t}_{\alpha\,\alpha'} \\
& \times \sum_{l_t=0,\{2\}}^{2t} \; \sum_{m_t=-l_t,\{2\}}^{l_t} \; {}^{c}_{l_t m_t t} \; {}^{m'}_{l_t l l'} \begin{pmatrix} l_t & l & l' \\ m_t & m & -m' \end{pmatrix} \begin{pmatrix} l_t & l & l' \\ 0 & 0 & 0 \end{pmatrix} \\
& \times \sum_{i=0}^{n-1-t} \sum_{\beta=2}^{N_R-1} \sum_{L=0}^{N_L} \sum_{M=-L}^{L} \tilde{C}^{\,\text{c.m.}}_{q_\kappa,\mathbf{b}} \sum_{\beta'=2}^{N_R-1} \sum_{L'=0}^{N_L} \sum_{M'=-L'}^{L'} \tilde{C}^{\,\text{c.m.}}_{p_{\kappa'},\mathbf{b}'} \; {}^{2i+1}_{\beta\,\beta'} \\
\times & \sum_{l_i=1,\{2\}}^{2i+1} \left\{ \left[\tilde{\ }{}^{c}_{l_i 0 i} \begin{pmatrix} L_i & L & L' \\ 0 & M & M' \end{pmatrix} + \sum_{m_j=-L_i,\{2\}}^{L_i} \tilde{\ }{}^{c}_{L_i M_i i} \begin{pmatrix} L_i & L & L' \\ M_i & M & -M' \end{pmatrix} \right] \right. \\
\times & \left. {}^{M'}_{L_i L L'} \begin{pmatrix} L_i & L & L' \\ 0 & 0 & 0 \end{pmatrix} \right\} \qquad (4.40)
\end{aligned}
$$

where

$$
{}^{a}_{b\,c\,d} = (-1)^{a} \sqrt{\frac{(2b+1)(2c+1)(2d+1)}{4\pi}}\,, \qquad (4.41)
$$

and ${}^{\lambda}_{\alpha\,\alpha'}$ (${}^{\lambda}_{\beta\,\beta'}$) denote the integrals over B splines and their derivatives for rel. (c.m.), see equations (C.6) and (C.5). The components $W_{\text{o\_o}}$, $W_{\text{e\_e}}$, $W_{\text{e\_o}}$, and $W_{\text{o\_e}}$ in equation (4.36) correspondingly denote the terms where the products of center-of-mass and relative-motion both have odd-odd, even-even, even-odd, or odd-even powers.

4.2 Symmetry implementation

Choosing the vector connecting the centers of the two traps such that it is parallel to one of the Cartesian axes and if the displacement of the two traps is restricted along one axis of the optical lattice, the symmetry in the directions orthogonal to the displacement axis remain unaffected. In the case where the two particles are confined in isotropic harmonic traps at the same center, the problem has spherical symmetry. While when both particles are trapped in an anisotropic confinement e. g., $\omega_x \neq \omega_y = \omega_z$, then the system possesses cylindrical symmetry. Moreover, if the traps of the two particles are displaced from each other, then system posses cylindrical symmetry. When the particles are displaced while confined in identical isotropic traps, they will have equivalent points at either ends of the displacement axis, a horizontal mirror plane, and an infinite number of two-fold rotation axes perpendicular to the principal axis [115]. In this case, such a system will posses the $\mathrm{D}_{\infty\mathrm{h}}$ point group symmetry. However, if the two traps are different for both particles, then the symmetry elements are C_∞ and vertical mirror planes hence the point group for this case is $\mathrm{C}_{\infty\mathrm{v}}$. It should be noted that since the original code was designed for

Table 4.1: Character table for the $\mathrm{C_{2v}}$ point group.

$\mathrm{C_{2v}}$	E	$C_2(z)$	$\sigma_v(xz)$	$\sigma_v(yz)$	linear, rotations	quadratic
A_1	1	1	1	1	z	x^2, y^2, z^2
A_2	1	1	-1	-1	R_z	xy
B_1	1	-1	1	-1	x, R_y	xz
B_2	1	-1	-1	1	y, R_x	yz

orthorhombic symmetry due to the orthogonal optical lattice potentials which has $\mathrm{D_{2h}}$ symmetry, it was convenient to implement the $\mathrm{C_{2v}}$ symmetry even though only single-well potentials are considered in the present study. Higher order symmetries as $\mathrm{D_{\infty h}}$ and, or $\mathrm{C_{\infty v}}$ could still in principle be implemented.

To implement symmetry into the extension method incorporating spatial displacement of the trap potentials, an assumption is made that the confining potentials are solely displaced along the z direction. Then, symmetry can be accounted for by considering a system whose potential energy is symmetric in the x and y directions, but without symmetry in the remaining z direction. The system and thus its Hamiltonian is therefore invariant under the symmetry operations of the $\mathrm{C_{2v}}$ point group. The symmetry group $\mathrm{C_{2v}}$ has four irreducible representations

$$\mathcal{I}_r = \{A_1,\, A_2,\, B_1,\, B_2\}\,. \tag{4.42}$$

The symmetry operations of the $\mathrm{C_{2v}}$ point group includes the identity operation E, a rotation about π along z axis, $\mathrm{C_2}$, and two vertical mirror planes σ_v and σ_v'. These symmetry elements are shown in Figure 4.2. Thus, the system eigenfunctions belong to the different irreducible representations and have different symmetries: the A_1 eigenfunctions are completely symmetric with respect to the xz and yz planes, while the eigenfunctions that belong to the A_2 irreducible representations are completely antisymmetric with respect to those planes. The B_1 (B_2) eigenfunctions are symmetric (antisymmetric) with respect to the xz plane and antisymmetric (symmetric) with respect to the yz plane.

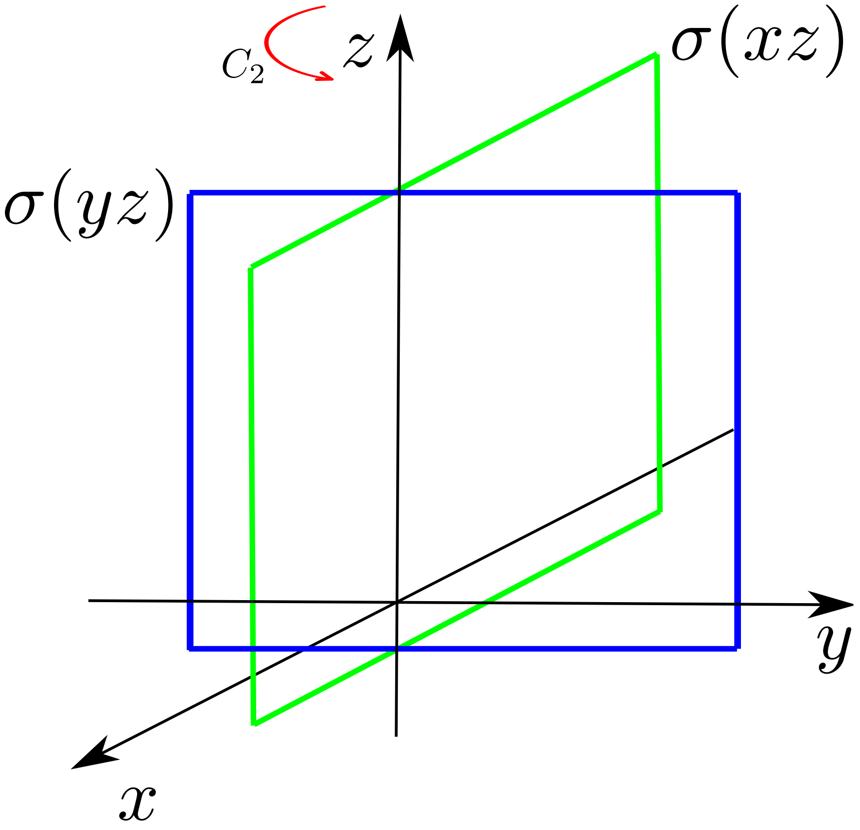

Figure 4.2: The symmetry operations of the point group C_{2v}. The reflection through the xz and yz planes, and C_2 is a π rotation around the z axis. The complete operations includes the identity E.

The symmetry-adapted basis functions for the relative-motion Hamiltonian (4.33) after the symmetry considerations are given by

$$\psi_i^{A_1} = \sum_{\alpha=1}^{N_r}\sum_{l=0,\{2\}}^{N_l}\sum_{m=0,\{2\}}^{l} \tilde{c}^{A_1}_{i,\alpha lm}\frac{B_\alpha(r)}{r}\;{}^{+}_{lm}\,, \tag{4.43}$$

$$\psi_i^{A_2} = \sum_{\alpha=1}^{N_r}\sum_{l=2,\{2\}}^{N_l}\sum_{m=2,\{2\}}^{l} \tilde{c}^{A_2}_{i,\alpha lm}\frac{B_\alpha(r)}{r}\;{}^{-}_{lm}\,, \tag{4.44}$$

$$\psi_i^{B_1} = \sum_{\alpha=1}^{N_r}\sum_{l=1,\{2\}}^{N_l}\sum_{m=1,\{2\}}^{l} \tilde{c}^{B_1}_{i,\alpha lm}\frac{B_\alpha(r)}{r}\;{}^{+}_{lm}\,, \tag{4.45}$$

$$\psi_i^{B_2} = \sum_{\alpha=1}^{N_r}\sum_{l=1,\{2\}}^{N_l}\sum_{m=1,\{2\}}^{l} \tilde{c}^{B_2}_{i,\alpha lm}\frac{B_\alpha(r)}{r}\;{}^{-}_{lm}\,, \tag{4.46}$$

Table 4.2: Product table for the irreducible representations of $\mathrm{C_{2v}}$

$\otimes$	A_1	A_2	B_1	B_2
A_1	A_1	A_2	B_1	B_2
A_2	A_2	A_1	B_2	B_1
B_1	B_1	B_2	A_1	A_2
B_2	B_2	B_1	A_2	A_1

where ${}^{+}_{l0} = {}^{-}_{l0} = Y_l^0(\theta,\phi)$ and ${}^{\pm}_{lm} = Y_l^m(\theta,\phi) \pm Y_l^{-m}(\theta,\phi)$ for $m \neq 0$. The expressions for the symmetry-adapted basis functions for the center-of-mass are analogous.

The configurations for solving the full Hamiltonian (4.31) are formed from the products of c.m. and rel. eigensolutions. The irreducible representations of these products are specified in Table 4.2. By using the symmetry adapted basis functions, the size of the total Hamiltonian matrix $\mathcal{N}$ is formed by 4 blocks of size $\mathcal{N}/4$ and since the diagonalization of a matrix scales as $\mathcal{N}^3$, the diagonalization of the Hamiltonian matrix in a symmetrized basis set would require $4 \times \left(\frac{\mathcal{N}}{4}\right)^3 = \frac{\mathcal{N}^3}{16}$ operations. Therefore, the dimensions of the matrices to be diagonalized reduces by a factor of about 16 and the required storage memory reduce by a factor of 4.

4.3 Influence of the displacement term on the energies

The two traps can be displaced in a number of ways. One trap can be fixed while moving the second trap and vice versa or both can be displaced with respect to each other. In each situation, the displacement term contributes differently to the center-of-mass and relative motion energies depending on the frequency of each trap and the respective masses of the two particles. In general, when the masses of the two particles are not equal, $m_1 \neq m_2$, and the trap frequencies $\omega_1 \neq \omega_2$, the contribution from the displacement term to both rel. and c.m. energies is the same regardless of the choice of trap displacement. However, the total energy of the two particles will be the same irrespective of the manner in which the two traps are displaced.

To demonstrate how the different displacement options for the two traps influences the c.m. and rel. energies, an example of two identical particles each with mass m in an isotropic harmonic trap potential with frequency ω are considered. When one trap is fixed at the origin while displacing the second one, then the distance of separation will have an equal contribution of $1/4\, m\, \omega^2\, d^2$ to both c.m. and rel. energies. This is true if the order is reversed, i. e., second trap fixed while displacing the first trap. The trap potential for c.m. and rel. motions are respectively given by

$$\hat{V}_{\text{c.m.}}(\vec{R}\,) = \frac{1}{2}\,M\,\omega^2\left(\frac{d}{2}-R\right)^2 \tag{4.47}$$

$$\hat{v}_{\text{rel.}}(\vec{r}\,) = \frac{1}{2}\,\mu\,\omega^2\,(d-r)^2 \tag{4.48}$$

where μ is the reduced mass and M is the total mass for the two particles.

The other alternative of displacing the two traps relative to each other is by moving them in opposite directions away from the origin in equal steps. This way, the two traps remain equidistant from each other with the origin remaining at the middle of the line joining the centers of the two traps. The setup can be visualized as depicted in Figure 4.1. Assuming the two particles have equal mass and that they are trapped at the same frequency, the displacement term enter only the relative motion energy. This is because the position of the center-of-mass does not change and always remain at the origin. The harmonic trap potential for c.m. and rel. takes the following form (the same form as in ref [116]),

$$\hat{V}_{\text{c.m.}}(\vec{R}\,) = \frac{1}{2}\,M\,\omega^2\,R^2, \tag{4.49}$$

$$\hat{v}_{\text{rel.}}(\vec{r}\,) = \frac{1}{2}\,\mu\,\omega^2\,(r-d)^2\,. \tag{4.50}$$

4.4 Test of implementation: non-interacting case

To verify whether the implementation of the method has been done correctly, the special case of two noninteracting particles is considered. When the particles do not interact, they see only the trap potential and the total energy is independent of the separation between the them. Besides providing a minimum check for the correctness of the implementation, this calculation provides also important information on the convergence behavior.

Consider two noninteracting ^{7}Li atoms confined in isotropic harmonic-trap potentials with the same trap frequency. The eigenvalues and eigenfunctions for this system are those of the harmonic oscillator. Taking the polarizability of the two atoms $\alpha = 164$ a.u., wavelength $\lambda = 1000$ nm and intensity $I = 1000$ W cm^{-2}, these parameters yields a trap with depth $V_0 = 5.896\,E_{\text{r}}$ the recoil energy $E_{\text{r}} = {}^2k^2/2m$, and frequency $\omega \approx 2\pi \times 22$ kHz in x, y, and z directions. The box size should be chosen such that it contains both traps

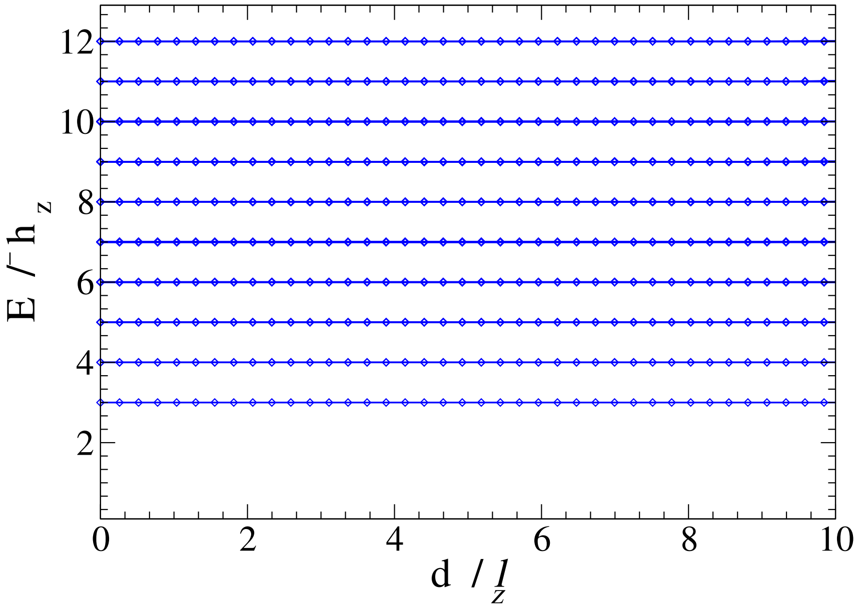

Figure 4.3: Total energy spectrum for the A_1 symmetry of two non-interacting particles in an isotropic harmonic trap potential as a function of trap separation along z direction. Each particle is trapped at a frequency $\omega \approx 2\pi \times 22$ kHz.

at the desired maximum separation distance. Also, since harmonic potentials extend to $+\infty$, the states of interest should fit into this finite box. Definitely, larger trap separations will require more B splines and larger box sizes. In this example, a box size of $\sqrt{3} \times 40000\, a_0$ is used with a maximum separation between the two traps being $10\, l_z$ where $l_z \approx 2730\, a_0$ is the length of the harmonic trap along the z direction defined by equation (2.49). 300 B splines of order 8 distributed in a linear knot sequence to cover the entire box, and the spherical harmonics expanded upto $l = 30$ with $m = 0$ for both rel. and c.m. in the orbital calculations. The traps are displaced along the z direction equidistant from each with the origin at the middle (see Figure 4.1). The results of the total energy as a function of the trap displacement is shown in Figure 4.3 for the A_1 symmetry. The energy spectra show the first 10 energy level. From this example, the eigenvalues are sufficiently converged with respect to the analytical energies of two harmonic oscillators. In fact, the first twenty lowest states are converged to at least the fifth digit with this basis specification. From the spectrum it is seen that the total energy for the two particles is independent of the separation between them. This is expected because the two particles do not interact.

Figure 4.4 shows the cuts through the six-dimensional wavefunctions for the ground state of the two particles along the z direction ($x_1 = x_2 = y_1 = y_2 = 0$) for zero (left) and 10 l_z (right) trap separations, respectively. When the two

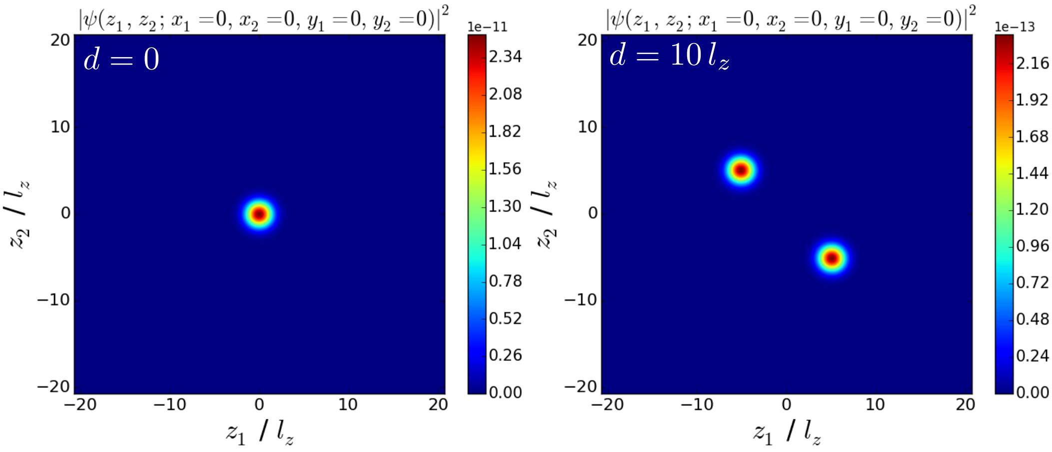

Figure 4.4: Cut of the two-particle density as a function of z_1 and z_2 ($x_1 = x_2 = y_1 = y_2 = 0$) scaled by the trap length along the z direction. The left plot shows the case of non-separated traps, $d = 0$, while the right plot is for the case when the two particles are separated by a distance $d = 10\, l_z$.

traps are not separated, the wavefunctions of the two particles overlap since they share the same point as shown on the left plot. As the separation distance between the two traps increases, the particles become clearly separated and ultimately reside exclusively in different traps (right plot of Figure 4.4).

Finally, it is important to remind that the same conclusions are true if both traps were moved such that they remained equidistant from each other with the origin at the middle. As already discussed in Chapter 3, whenever $\omega_1 \neq \omega_2$, a coupling exists between c.m. and rel. motions. The computation demands for the CI calculations increases as the coupling strength between the motions increases. With the m restriction implementation in the code, it is possible to consider anisotropic confinements.

4.5 Summary

In this chapter, an extension of the original method for describing two ultracold atoms in an optical-lattice potential and interacting among each other with central interatomic interaction potentials has been extended to include the possibility to spatially separate the trap potentials confining each of the two particles. For numerical efficiency, symmetry was implemented. It should be noted that the C_{2v} symmetry implementation was motivated by the structure of the original method that was designed for orthorhombic symmetry of the optical lattice. The much higher and more efficient $D_{\infty h}$ and $C_{\infty v}$ symmetries could still in principle be implemented. The present code is therefore limited to orthorhombic lattices for example where one of the particles is trapped in a periodic (optical) lattice and the displacement has to be along one of the crystal axes. In order to profit from the m restriction, the displacement of the two traps is chosen along the z direction.

Finally, even though the present study aims to describe an ion-atom system, a straightforward application of the present method is simulating neutral atoms in polarization-synthesized optical lattices [117]. State-selective OL shift can be realized by varying the lattice spacing between the atoms such that they are in different hyperfine states. This way, the lattice sites acts as storage and shift registers in atom-sorting schemes [118].

Chapter 5

Atom-Ion Interaction Potentials

The generic example for the realistic atom-ion interaction used in the present study is the *ungerade* electronic state of Li_2^+. The construction details about these potential curves together with the manipulation technique used to vary the scattering length values are provided in this chapter.

5.1 *Ab initio* potential energy curves for Li_2^+

The full interaction potential for the atom-ion system can be split into two parts: the short-range part and the long-range part. The short-range region $\mathcal{U}_{\text{SR}}(r)$ for internuclear distances ranging from 1.0 to 100 a_0 is constructed from the recently published *ab initio* data of Li_2^+ potential energy curves in Ref. [81] generously supplied by M. Bouledroua [119]. These potentials were calculated using a method similar to the one mentioned at the end of section 2.1 in Chapter 2, i. e., the Li_2^+ system is treated as an effective one-active electron moving in the field of two ionic cores and their interactions described by effective potentials while the wavefunctions are expanded on a set of generalized Slater-type orbitals expressed in prolate spheroidal coordinates, more details can be found in Ref. [120]. A cubic spline fitting[1] numerical scheme was used to interpolate the *ab initio* data points to obtain the short-range potential as a function of the internuclear separation.

The long-range part $\mathcal{U}_{\text{g,u}}(r)$ is given by [39]

$$\mathcal{U}_{\text{g,u}}(r) = \mathcal{U}_{\text{disp}}(r) \mp \mathcal{U}_{\text{exc}}(r) \tag{5.1}$$

with ∓ for *gerade* (g) and *ungerade* (u), respectively. The first term $\mathcal{U}_{\text{disp}}(r)$ is the dispersion potential introduced earlier in equation (2.46). For Li_2^+, the higher order Van der Waals coefficients are known and the dispersion potential is given (in atomic units) by

$$\mathcal{U}_{\text{disp}}(r) = -\frac{1}{2}\left(\frac{C_4}{r^4} + \frac{C_6}{r^6} + \frac{C_8}{r^8}\right) \tag{5.2}$$

where the coefficients C_4, C_6, and C_8 are the dipole, quadrupole, and octupole polarizabilities, respectively. The second term of equation (5.1) is the exchange

---

[1] This form of interpolation is suitable for data points where the curvature changes sign.

Table 5.1: The scattering length values for the *gerade* and the *ungerade* electronic states of Li_2^+ potential. The literature values are taken from [45, 122].

	gerade		*ungerade*	
	Present (a_0)	Literature (a_0)	Present (a_0)	Literature (a_0)
$^6\mathrm{Li} + {}^6\mathrm{Li}^+$	-477	-918	-1429	-1425
$^7\mathrm{Li} + {}^7\mathrm{Li}^+$	-5356	14337	1264	1262

interaction. The exchange energy basically accounts for the exponentially small energy difference between two asymptotically degenerate states of a diatomic molecule or molecular ion, a general procedure for calculating exchange energies for one-active-electron diatomic ions can be found e. g., in [121]. For the purposes of constructing the atom-ion potentials used in this thesis, the form of the exchange energy given in [81] is used. It is explicitly given by

$$\mathcal{U}_{\mathrm{exc}}(r) = \frac{1}{2}\mathcal{A}^2 r^{\frac{2}{\beta}-1} e^{-\beta r} \tag{5.3}$$

where $\mathcal{A}$ is the amplitude of the asymptotic wavefunction, and the parameter β is determined from the ionization energy E_I using $\beta = (2E_I)^{1/2}$.

The short-range data points were smoothly merged with the long-range part to obtain the full potential, i. e., $V(r) = \mathcal{U}_{\mathrm{SR}}(r) + \mathcal{U}_{\mathrm{g,u}}(r)$. The values of the parameters appearing in the dispersion equation (5.2) and the exchange equation (5.3) are all taken from [81]. These values (in atomic units) are: $C_4 = 164.19$, $C_6 = 1393$, $C_8 = 38710$, $\beta = 0.630$, and $\mathcal{A} = 0.815$. Fitting the interpolated *ab initio* points to the dispersion form (5.2) yielded $C_4 = 164.18999999916$, $C_6 = 3393.0000155742$, and $C_8 = 38709.92748$ which agree with the values given in [81]. The resulting potentials were already shown in Figure 2.1.

After constructing the full atom-ion interaction potentials, the scattering-length values and the number of bound states supported by the two potentials was determined. The scattering length values shown in Table 5.1 are obtained from the point of intersection of the extrapolated radial wavefunction and the r axis from equation (2.36) as described in section 2.3.1. The same values are found using the semiclassical treatment given by equation (2.37). The values of the scattering length for the *ungerade* electronic state of ^{6}Li and ^{7}Li isotopes agree fairly well to those in [45, 122]. However, the *gerade* values are not agreeing. In the case of ^{6}Li isotope, the magnitudes are different, while for the ^{7}Li isotope, both the magnitude and the sign differ. A reason for this deviation could not be found by the author.

Using equation (2.39), the number of bound states for the *gerade* and the *ungerade* electronic states for the ^{6}Li isotope are found to be 78 and 17, respectively. For the ^{7}Li isotope, the *gerade* and the *ungerade* potentials correspondingly have 84 and 19 bound states. A similar number of bound states for both isotopes is obtained if the radial SE (2.26) is solved for the trap-free case with $l = 0$ using the two potentials. The obtained number of bound states are comparable to those in [123] where it is reported (without specifying the isotopes) that the *gerade* state has 85 vibrational levels while the *ungerade* should have more than 14 levels.

Since the value of scattering length for *ungerade* potentials for both ^{6}Li and ^{7}Li isotopes agree fairly well compared to those reported in literature, this electronic state is chosen to model the atom-ion interaction in this thesis. Also, the relatively small number bound states supported by this particular potential means that less number of B splines are required to describe it.

5.2 Manipulation of the interaction potentials

As already mentioned in section 2.4, the accurate calculation of magnetic Feshbach resonances is a very laborious multi-channel (MC) problem. However, this complicated MC problem can be reduced to one parameter, i. e., the scattering length. The variation of the scattering length can then be related to the variation of the magnetic field. Single-channel (SC) approximations have been developed to describe the collisions of two atoms in resonant magnetic fields where the MC calculations are too demanding. One such SC approach is found in [100]. The idea underlying the SC approach is to vary the interaction strength artificially through a controlled manipulation of the Hamiltonian

$$\hat{\mathrm{H}}\,(r) \;=\; -\frac{1}{2\mu}\,\frac{\partial^2}{\partial\, r^2} + V(r) \tag{5.4}$$

where the reduced mass μ or the interaction potential $V(r)$ can be modified. Each of these modifications lead to a shift of the energy of the least bound state relative to the atom-ion potential threshold. Whenever a bound or a virtual[2] state crosses the dissociation threshold, the scattering length diverges. Single-channel techniques can be used to manipulate the energy of the bound or the virtual state in order to vary the scattering length.

The approach used in the present study follows the technique described in [100] where the strong-repulsive inner wall of the atom-ion potential is modified

---

[2] When a real bound state is lifted into the continuum, it turns into a virtual state.

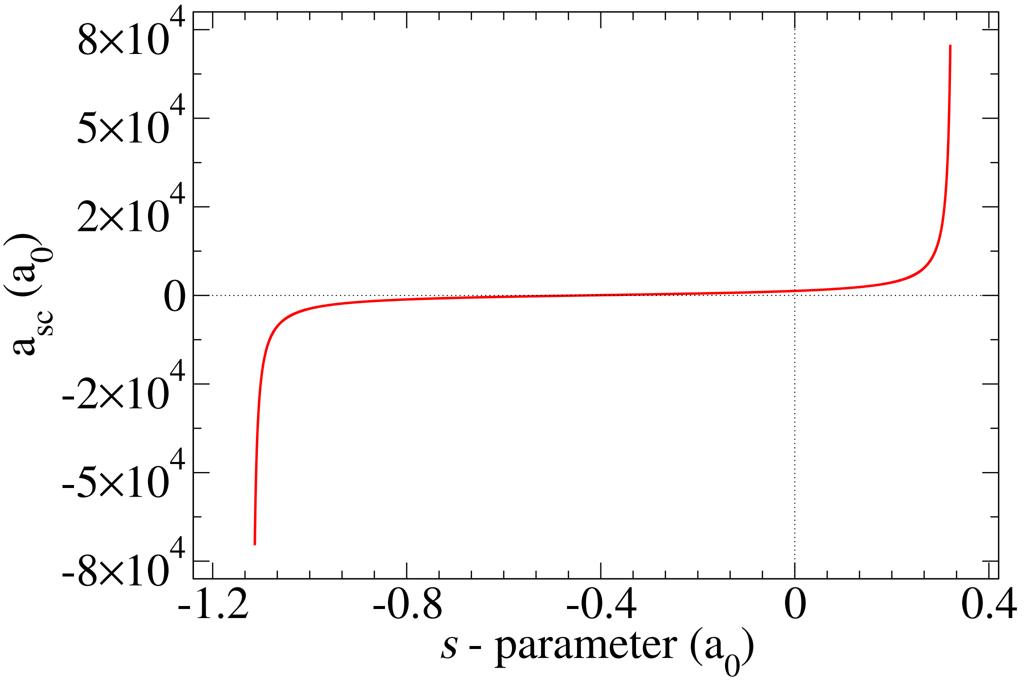

Figure 5.1: Scattering length a_{sc} as a function of the inner wall shift, s-parameter, for the *ungerade* ^{7}Li + ^{7}Li$^+$ potential. Modifying the inner wall continuously changes the scattering length from $-\infty$ to $-\infty$. This correspond to tuning the atom-ion interaction from strongly attractive via almost noninteracting to strongly repulsive.

by replacing $V(r)$ by

$$V^s(r) = \begin{cases} V(r - s\dfrac{r - r_e}{r_c - r_e}) \, , & r \leq r_e \, , \\ V(r) \, , & r > r_e \, , \end{cases} \tag{5.5}$$

where r_e is the equilibrium internuclear distance, r_c is the threshold crossing point, and s is the parameter denoting the shifting of the inner wall. The systematic shifting of the repulsive inner wall leads to a change in scattering length. Figure 5.1 shows a graph of the s-wave scattering length as a function of the s-parameter. In this case, the s-parameter is varied around one SC resonance. It is also possible to vary the s-parameter over two branches of scattering length, i. e., $a_{\mathrm{sc}} \in [-\infty, 0]$ and $a_{\mathrm{sc}} \in [0, \infty]$.

The inner wall shifted BO curves for the interaction of ^{7}Li in the *ungerade* electronic state is given in Figure 5.2 (a) for $s = -0.5210587\,a_0$ (black), $s = 0$ (red), and $s = 0.3037423\,a_0$ (green). The corresponding SC wavefunctions associated with each shift as given in Figure 5.2 (b).

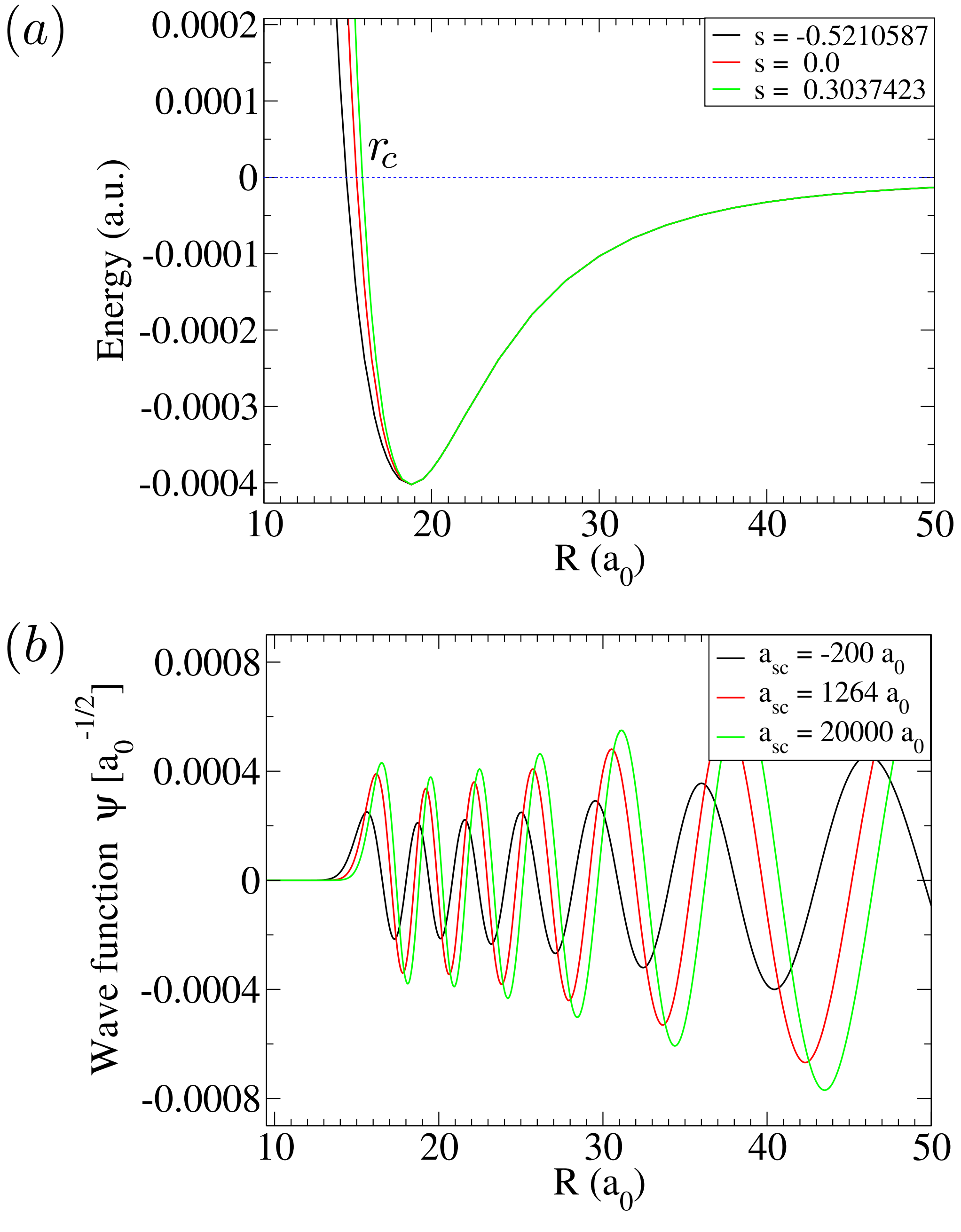

Figure 5.2: (a) Shifted Born-Oppenheimer curves for the interaction of ^{7}Li in the $^2\Sigma_u^+$ electronic state. (b) Single channel wavefunctions for $a_{\rm sc} = -200\,a_0$ (attractive), $a_{\rm sc} = 1264\,a_0$ (repulsive), and $a_{\rm sc} = 20000\,a_0$ (strongly repulsive), corresponding to the shifted potentials given in part (a) with $s = -0.5210587\,a_0$, $s = 0$, and $s = 0.3037423\,a_0$.

Table 5.2: Sample s-parameters and the corresponding scattering-length values for the *ungerade* electronic state of the ^{7}Li + ^{7}Li$^+$ potential.

s-paramter (a_0)	a_{sc} (a_0)
-0.026362681122	1136.07123338988
-0.019587014042	1167.53312619044
-0.013349688033	1197.37919251038
-0.007571419132	1225.82871430544
-0.002189243241	1253.05804466889
0.002847676772	1279.21128495351
0.007580978309	1304.40780877984
0.012045193091	1328.74769907233
0.016269277337	1352.31575712239
0.020277751011	1375.18450813941
0.024091560169	1397.41650412312
0.027728739454	1419.06610223174
0.031204927848	1440.18085766712

The mimicking of the variation of the s-wave scattering length at a Feshbach resonance using the inner wall shift is performed as follows: The scattering length values are calculated from the asymptotic solution given by equation (2.36) for various values of the s-parameter using the program[3] `scatlength.f90`. A sample resulting values of a_{sc} for each s-parameter are shown in Table 5.2 (plotted in Figure 5.1), the first column are the s-parameter values while the second column are the corresponding s-wave scattering length values. From this data, for any given s-parameter value the corresponding a_{sc} is obtained by interpolation, e. g., if a potential whose interaction strength is characterized by $a_{\text{sc}} = 1397.41650412312\, a_0$ is required, then the atom-ion potential $V(r)$ is shifted by $s = 0.024091560169\, a_0$ and the required potential is obtained from equation (5.5) using this new s-parameter value.

Finally, as a technical detail, generally the potential curves are extremely sensitive. One has to be very careful when merging the *ab initio* data points and the long-range part when constructing the complete potentials. One way of finding out if this merging has been done properly is to check the wavefunction in the regions where the two sets of data are joined. The other way is to fit the final potentials to the long-range form and compare the resulting coefficients with the known theoretical values. Also, during the manipulation process discussed above, if the values r_e and r_c are not accurately determined, one will end up with wrong results e. g., a possible kink in the energy spectrum analysis because the scattering length could change sign when actually no bound or virtual state has crossed the threshold due to the incorrect value of r_e and or r_c. It is worthy to remind that r_c should be determined accurately numerically

---

[3] Located in $\sim$`/TwoAtInOL/asc`. Run instructions are found on the script files inside the code directory.

and should not be taken simply as the value of the internuclear separation with the last negative value as $r \to 0$. The same applies to the equilibrium distance[4,5] r_e.

---

[4] After cubic spline interpolation of the *ab initio* data, the equilibrium values for the *gerade* and *ungerade* electronic states were found to be $5.86067959444027\,a_0$ and $18.7946443223160\,a_0$, respectively, compared to $5.85999999999992\,a_0$ and $18.7900000000001\,a_0$ from the original data.

[5] This stage of mapping the s parameter with the corresponding scattering-length values took a considerable amount of time during the study. A program based on an existing one for the lowest triplet and singlet states of two lithium atoms was developed to shift the inner wall of the Li_2^+ potentials.

Chapter 6

Systems of trapped atoms and ions

The formulation and implementation of the extension presented in Chapter 4 was done in a general manner. In this chapter, the developed approach is used to investigate a system composed of an ultracold neutral atom and a single ion confined in separated harmonic trapping potentials. The interaction between the atom-ion pair is modeled using as a generic example the *ungerade* electronic state of ^{7}Li isotope published in [81]. The construction details and the motivation for the choice of this potential is discussed in Chapter 5. In this chapter, states and energy spectra belonging to the irreducible representation A_1 of the $\mathrm{C_{2v}}$ point group are considered.

6.1 Model Hamiltonian

The system of interest is composed of a single neutral atom and a single ion. The two particles are confined in separate trapping potentials. The ion traps conventionally used in experiments are the radiofrequency (rf) traps. These rf traps use a combination of static and time varying electric fields to confine the ions [29]. As already pointed in Chapter 1, the time varying fields in the rf traps continuously push and pull the ion back and forth leading to fast oscillations called *micromotion*. Assuming that the micromotion is averaged out, and the typical deep nature of the rf traps, the ion is to a good approximation trapped in a time-independent harmonic potential provided it is close to the ground state of the potential well. Single neutral atoms on the other hand can be trapped in experiments using for example optical lattices. If the atom trap is also assumed to be well approximated by a harmonic potential, then the Hamiltonian (in atomic units) for the trapped atom-ion system can be written as

$$\hat{H}(\mathbf{r}_1, \mathbf{r}_2) = \frac{1}{2} \sum_{j=1}^{2} \left[-\frac{\nabla^2}{m_j} + m_j \omega_{\perp j}^2 \rho_j^2 + m_j \omega_j^2 (z_j - d_j)^2 \right] + \hat{U}(|\mathbf{r}_1 - \mathbf{r}_2|) \tag{6.1}$$

where $\rho^2 = x^2 + y^2$, $\omega_\perp$ is the transverse frequency, and d is the distance between the two trap minima, as before. The harmonic confinement is obtained from the Taylor expansion of equation (4.2) up to the second order. The trap frequencies

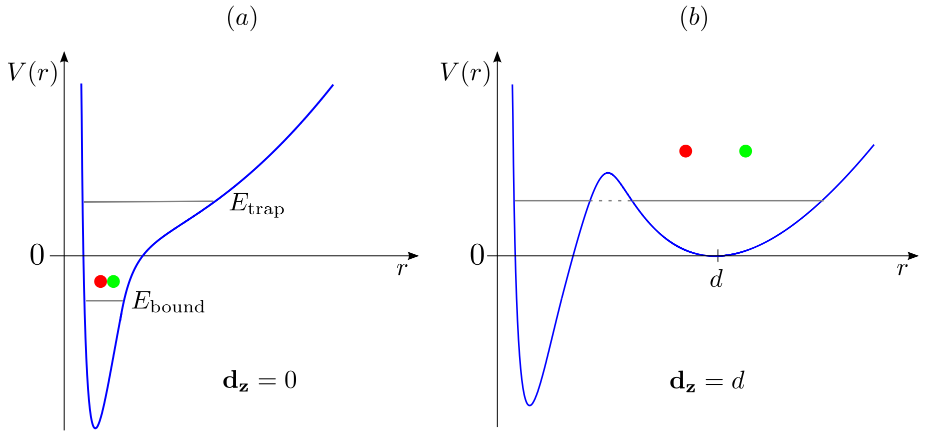

Figure 6.1: Schematic illustration of the trap-induced resonance. (a) Two particles trapped in a harmonic potential will experience an effective potential (blue line) given by the sum of the trap and interaction potentials at zero trap separation. (b) As the separation between the two traps increases, the least bound molecular state E_{bound} becomes resonant with the trap vibrational states E_{trap} resulting in a trap-induced resonance. For large separations, the relative coordinate is bound by the trap potential.

for the atom-ion pair are assumed to be equal in the present discussions hence no coupling exists between c.m. and rel. motions.

Transforming the two-body Hamiltonian (6.1) to c.m.-rel.-motion coordinates (using equations (3.3) and (3.4)), and taking the vector of the trap separation to point along the positive z direction, the relative motion part of the Hamiltonian (6.1) becomes

$$\hat{H}_{\text{rel.}} = -\frac{1}{2\mu}\nabla_r^2 + \frac{1}{2}\mu\,\omega^2\Big[\rho^2 + (\mathbf{z} - \mathbf{d}_z)^2\Big] + \hat{U}(\mathbf{r}), \tag{6.2}$$

while the center-of-mass part is given by

$$\hat{H}_{\text{c.m.}} = -\frac{1}{2M}\nabla_R^2 + \frac{1}{2}M\,\omega^2\left[\rho^2 + \left(\mathbf{Z} - \frac{\mathbf{d}_z}{2}\right)^2\right]. \tag{6.3}$$

In the present numerical calculations, the two traps are displaced by fixing the atom trap at the origin while the ion trap is moved along the z coordinate away from the origin.

Figure 6.1 (a) shows the relative part of the effective potential given by the sum of the trap potential at zero separation ($\mathbf{d}_z = 0$) and the interaction potential energy $\hat{U}(\mathbf{r})$. As the separation between the two traps is increased, the molecular bound state E_{bound} of the molecular interaction potential is raised up. At certain trap separation distance ($\mathbf{d}_z = d$), see Figure 6.1 (b), the bound state E_{bound} and the trap eigenstate E_{trap} become resonant leading to a *trap-induced resonance* (TIR) [116, 124]. This kind of resonance was first reported by Stock et al. where they investigated the controlled collisions between two trapped but separated atoms [116]. In that work, the interaction between the ultracold neutral atoms is treated using an energy-dependent δ-function pseudopotential model. The trap-induced resonances have also been reported for a system consisting of ^{87}Rb atom and ^{40}Ca$^+$ ion stored in separate traps [72] by Idziaszek et al. where the atom-ion interaction is treated using quantum defect theory. These trap-induced resonances show up as avoided crossings in the energy spectrum as a function of the trap separation. TIRs offer means for controlling interactions between ultracold atoms with applications e. g. in the design of quantum logic gates.

6.2 Results and discussions

The interaction between a neutral ultracold atom and a single ion is described based on the eigenenergy spectrum as a function of the trap separation. The single-channel approach in [100] described in Chapter 5 is used to manipulate the repulsive inner wall part of the *ungerade* Li$_2^+$ in order to realize the required s-wave scattering length values. The discussions are grouped into two cases. In one case, the distance between the two traps is varied for fixed interaction strengths. The second case is for fixed trap separation and varying interaction strengths.

The first result discussed is when the atom-ion pair is confined in 3D spherically symmetric harmonic traps for fixed interaction strengths. The ^{7}Li - ^{7}Li$^+$ pair is trapped at equal frequencies $\omega = 2\pi \times 22\,\mathrm{kHz}$. Each of the two traps has a depth $V_c = 5.8955\,E_{\mathrm{r}}$. These trapping parameters are realized by using wavelength $\lambda = 1000$ nm and intensity $I = 1000$ W cm^{-2} in x, y, and, z directions.

Figure 6.2 shows the rel.-motion energy spectrum for ^{7}Li atom-ion pair with an interaction strength characterized by the s-wave scattering length $a_{\mathrm{sc}} = 2000\,a_0$ as a function of separation distance d. The energy spectrum is qualitatively different from the case of noninteracting particles (see Section 4.4) going from zero to positive trap separations. At zero trap separation, the energy of the least molecular bound state (blue line) is positioned at $-1.5576 \quad \omega_z$. This is a consequence of the large positive scattering length. As the separation between the two traps is increased, the molecular and vibrational trap states change in a rather pronounced fashion. The molecular state increases in energy as it get pulled up and at around $d \approx 2.59\,l_z$, it becomes resonant with the first vibrational trap state resulting in an avoided crossing. The avoided crossings correspond to the trap-induced resonances [116]. As the separation between the atom and ion traps is increased further, more avoided crossings are observed as the molecular bound state become resonant with the higher-lying vibrational trap states. The avoided crossings associated with the higher-lying states follow approximately the quadratic shape of the harmonic trapping potential confining the atom-ion pair. The position of the lowest TIR is approximately located at the point where the sum of the molecular bound state energy and the trapping potential at zero trap separation equals the lowest vibrational trap state of the harmonic oscillator energy. Beyond the resonance position, as the distance between the atom-ion pair is increased, the two particles acquires noninteracting harmonic oscillator states.

In Figure 6.3, the presented energy spectrum is for the interaction strength with $a_{\mathrm{sc}} = 4000\, a_0$. For this larger positive scattering-length value, the molecular bound state is much closer to the dissociation threshold. The least bound molecular state is at $-2.2983 \times 10^{-2}\ \ \omega_z$, compared to when $a_{\mathrm{sc}} = 2000\, a_0$. Therefore, the molecular bound state becomes resonant with the trap states at smaller trap separations for large positive scattering lengths. The spectrum is generally similar to the one given in Figure 6.2 except that the avoided crossings are much wider and occur at relatively smaller trap separation distances. The lowest trap-induced resonance appears at $d \approx 1.95\, l_z$ with an energy gap of about $0.5\ \ \omega_z$ compared to an energy gap of $0.14723\ \ \omega_z$ if the s-wave scattering length is $2000\, a_0$. In general, the position and size of the avoided crossings leading to the TIRs depends strongly on the energy of the molecular bound state [116]. For example, when the scattering length is negative, the molecular state is deeply bound and far away from the dissociation threshold. Figure 6.4 shows the eigenenergy spectrum versus the separation distance between the atom and ion traps when the interaction strength is characterized by $a_{\mathrm{sc}} = -1000\, a_0$. For this value of the scattering length, the energy of the least bound state is $-105.6097\ \ \omega_z$ for zero trap separation. Therefore, for such an attractive interaction, trap-induced resonances are not observed in the energy spectrum.

The energy spectrum for the full Hamiltonian is given by the sum of the rel. and c.m. Hamiltonians (6.3) - (6.2). Since the trap frequencies for the atom and the ion are equal, no coupling exists between the c.m. and rel. motions. Also, since the two harmonic traps are identical, the displacement term does not enter the coupling equation (4.9). Therefore, the full spectrum that incorporates the c.m. is similar to those of relative motion except that it is shifted up by the center-of-mass excitations as shown in Figure 6.5.

Another observation is that the states with positive energies $E/\ \ \omega_z$ at zero trap separation split into two branches as the distance between the atom-ion traps increases for repulsive atom-ion interactions (Figures 6.2 - 6.3). The

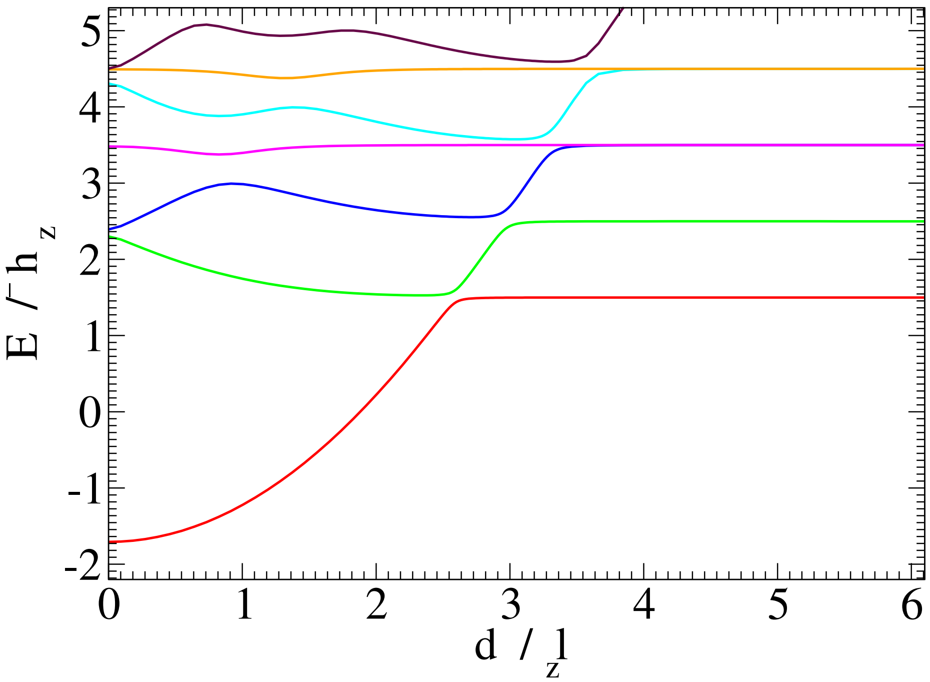

Figure 6.2: The relative motion energy spectrum as a function of separation d between the atom and ion traps for $a_{\text{sc}} = 2000\,a_0$. The trap-induced resonances show up as avoided crossings between the bound and vibrational trap states. The TIR associated with the crossing between the bound and lowest trap state is at $d \approx 2.59\,l_z$. As the separation between the atom and ion traps increases, the molecular bound state becomes resonant with the higher-lying vibrational trap states resulting in more avoided crossings. After the resonance, i. e., for larger separations, the atom-ion pair acquires noninteracting harmonic oscillator states represented by the horizontal lines. The energies and the separation distance have been correspondingly scaled by ω_z and l_z. The basis set used for the calculation is specified in Table E.1.

splitting behavior can be understood from the analysis of the corresponding eigenstates of the branches. Depending on the symmetry of the state, the rising (lowering) branch corresponds to the antisymmetric (symmetric) eigenstate where the atom-ion pair is localized in trap regions where they experience attraction (repulsion) [72]. The rel.-motion eigenstates corresponding to the two lowest states with positive $E/\ \omega_z$ in Figure 6.3 are shown in Figure 6.6. The full 6D-wavefunctions cuts along the z axis for the lowest splitting states is given in Figure 6.7 for $a_{\text{sc}} = 4000\,a_0$. The 6D wavefunctions in the absolute coordinates offers the visualization of the two particles in the two branches. The wavefunction for the branch splitting upwards with increasing energy is given by the plot on the right in Figure 6.7. It is observed that the atom-ion

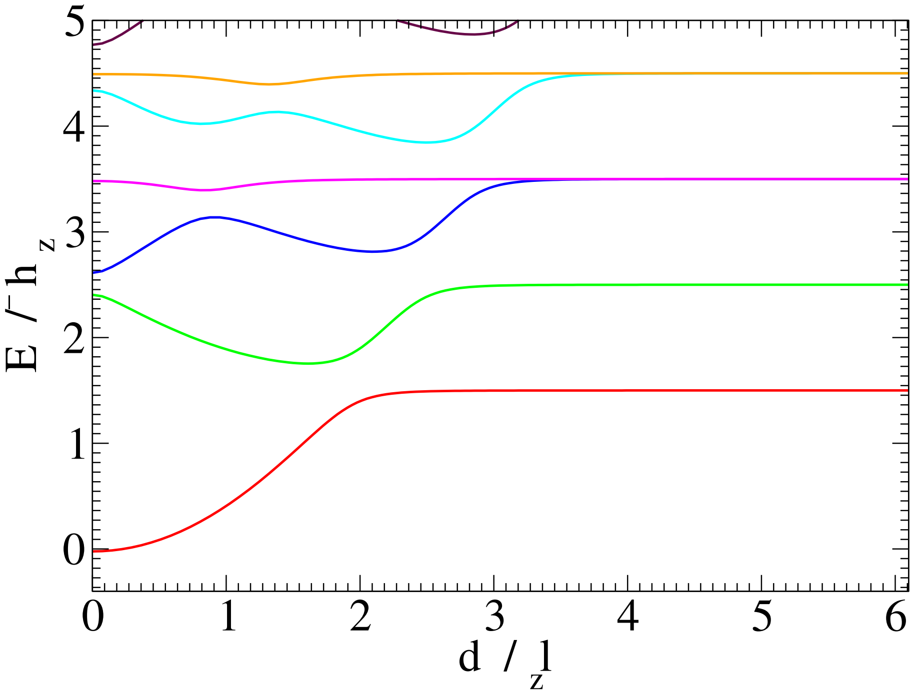

Figure 6.3: Similar to Figure 6.2 but with $a_{\mathrm{sc}} = 4000\,a_0$. A trap-induced resonance occurs at $d \approx 1.95\,l_z$. The energy gap between the resonant states are much larger compared to the case of $a_{\mathrm{sc}} = 2000\,a_0$ shown in Figure 6.2. The basis set used for the calculation is specified in Table E.2.

pair are close together implying an attraction between them while on the left, which corresponds to the lowering branch, the two particles are repelling and far from each other. Figure 6.8 shows the relative motion wavefunction for zero trap separation on the left and the right panel shows the case when the traps are separated by $3.67\,l_z$ with $a_{\mathrm{sc}} = 4000\,a_0$. At zero trap separation, the least bound state of the atom-ion pair is highly oscillating, after crossing the trap-induced resonance position, the two particles become noninteracting and the wavefunction become that of harmonic oscillator centered at $3.67\,l_z$. This explains the horizontal lines in the eigenenergy spectra after the avoided crossings where the atom and ion do not interact and see only their respective trap potentials.

Next, the analysis of the energy spectra for various interaction strengths at fixed trap separations is considered. When the distance between the two traps is fixed, and the interaction strength between the atom and the ion is varied from strongly attractive ($a_{\mathrm{sc}} \ll 0$) to strongly repulsive ($a_{\mathrm{sc}} \gg 0$), the spectrum exhibits a different structure compared to when the interaction strength is fixed for varying separations. Figure 6.10 presents the energy spectrum of the relative motion for spherically symmetric harmonic trap potential for

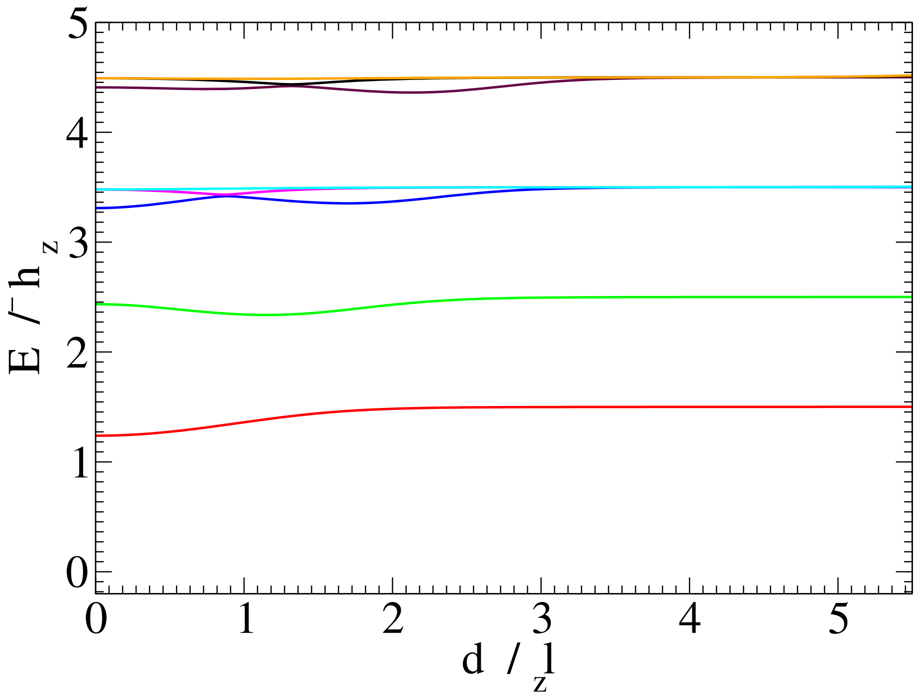

Figure 6.4: The relative motion energy spectrum for $a_{\rm sc} = -1000\,a_0$. The trap-induced resonances are not observed because the least molecular bound state is far from the threshold. The basis set used for the calculation is specified in Table E.1.

separations $d/l_z = 0, 0.3, 1.8$, and 3.6. If the separation distance between the two traps becomes comparable to or larger than the trap length l_z, the bound state (black line bending downwards to negative infinity for $l_z/a_{\rm sc} \to +\infty$) is pushed up and forms avoided crossings with the trap state as seen in Figure 6.10 for $d/l_z = 1.8$ and 3.6 where the separation distance is larger than the trap length. Figures 6.11 and 6.12 shows the energy spectra when anisotropy in introduced in the transversal direction such that $\omega_x = \omega_y = 5\,\omega_z$. Spectra for $\omega_x = \omega_y = 10\,\omega_z$ are given in Figures 6.13 and 6.14. For these anisotropic geometry, additional resonances which are induced by the trap anisotropy are observed in the excited states.

The cuts of the full 6D wavefunctions along the z direction for the first trap-induced state for $d/l_z = 0$, 0.37, 1.83, and 3.67 given in Figure 6.9. When the two traps are not separated, the neutral atom and the ion share the same location but since the interaction is repulsive ($a_{\rm sc} = 4000\,a_0$), the density plot shows two regions of large probability of finding the atom-ion pair away from the $z_1 = z_2$ diagonal. As the separation between the two particles increases, the pair begins to occupy regions closer to the diagonal and at $3.67\,l_z$ each particle resides in different regions along the z direction.

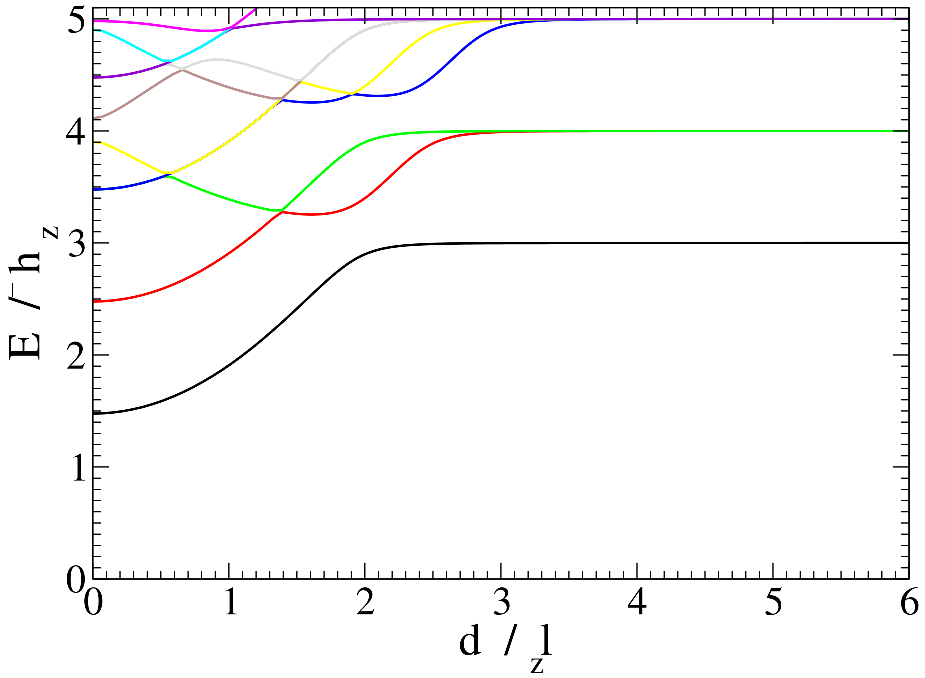

Figure 6.5: The CI energy spectrum for $a_{\rm sc} = 4000\,a_0$. The energy spectrum is similar to that of the relative motion in Figure 6.3 but the eigenstates are shifted up by the center-of-mass excitations.

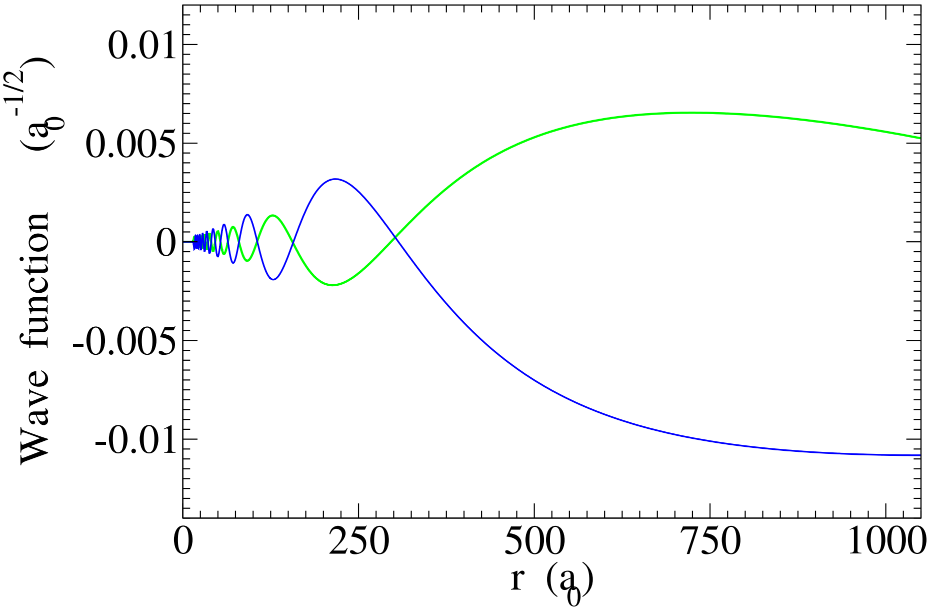

Figure 6.6: Eigenstates of the relative motion of the atom-ion pair at trap separation $d = 0.66\,l_z$ for the two lowest states with positive $E/\;\omega_z$ in Figure 6.3. The blue (green) eigenfunction corresponds to the rising (lower) state represented by the blue (green) line in the eigenenergy spectrum for $a_{\rm sc} = 4000\,a_0$.

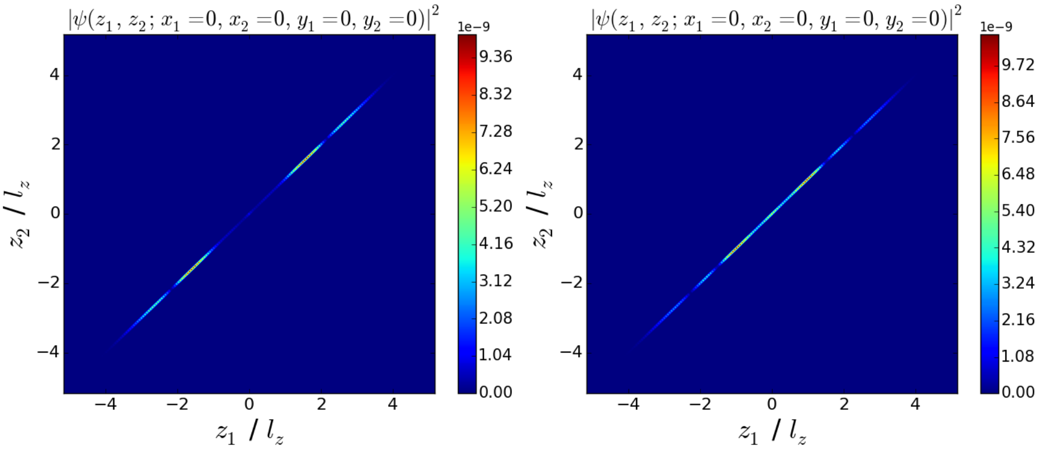

Figure 6.7: Cuts along the direction of the trap displacement through the six-dimensional *ab initio* wavefunction for the first (left) and second (right) trap states for trap separation $d = 0.66\, l_z$ when $a_{\rm sc} = 4000\, a_0$. The left plot shows the atom-ion pair in the region where they repel each other. This is the state corresponding to the lowering branch. On the right, the atom-ion are in the region of attraction hence closer to each other along the z direction. This is the state represented by the rising branch.

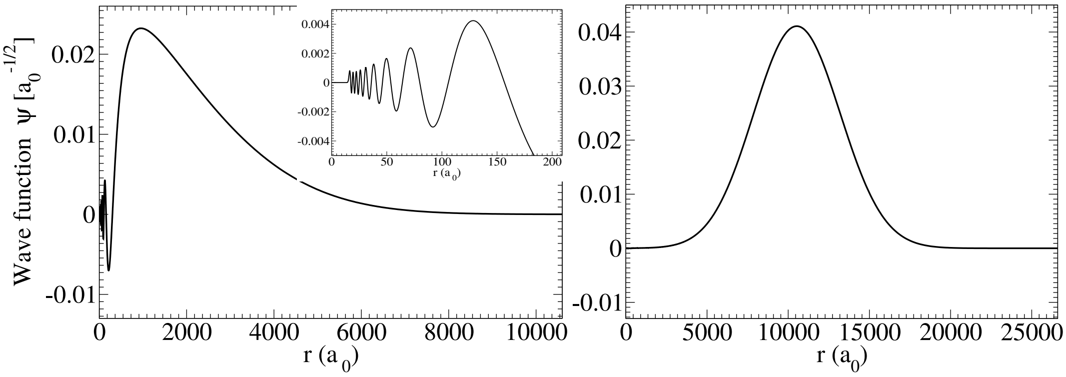

Figure 6.8: Scaled wavefunction of the relative motion of the least bound state at zero trap separation (left figure) and the first trap state (right) for trap separation $d = 3.67\, l_z$ for $a_{\rm sc} = 4000\, a_0$. The insert on the left figure shows the magnified view for the least bound state.

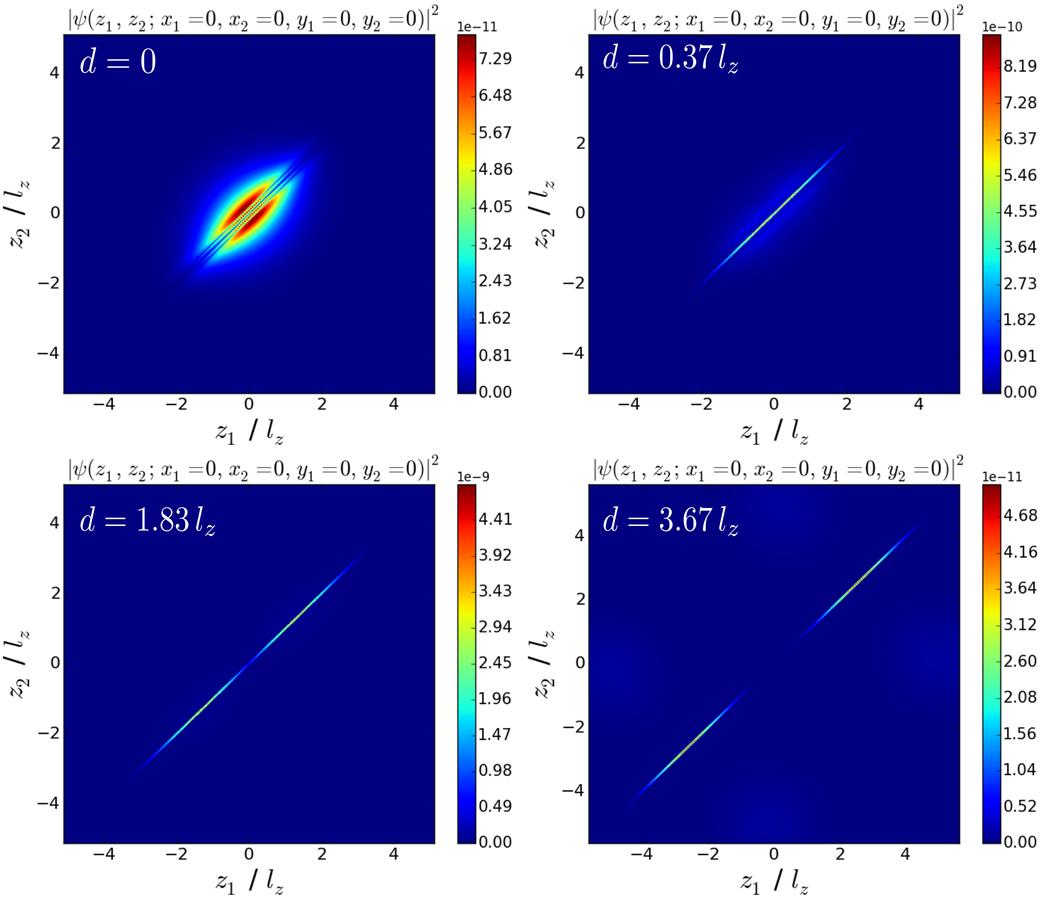

Figure 6.9: Cuts along the z direction through the full six-dimensional *ab initio* eigenstates for the atom-ion pair at separation distances $d/l_z = 0,\ 0.37,\ 1.83,\ 3.67$ for $a_{\mathrm{sc}} = 4000\, a_0$. From these wavefunctions, it is observed how the atom-ion pair initially close together when the traps are not separated become separated in space at large trap separation distances where they are only bound by the traps.

6.3 Conclusion

In this chapter, the description of a system comprising of a neutral ultracold atom and a single ion trapped in spatially separated harmonic traps has been presented. The atom-ion interaction has been treated in a realistic fashion using Born-Oppenheimer potential curve of Li_2^+. As an application of the developed method to study atom-ion systems, the energy spectrum against separation distance between the atom and the ion confined in a harmonic trap has been analyzed and the expected trap-induced resonances have been observed. This is consistent with previous studies on the atom-ion systems. The key feature of the approach is that it allows for treating the atom-ion interactions in a

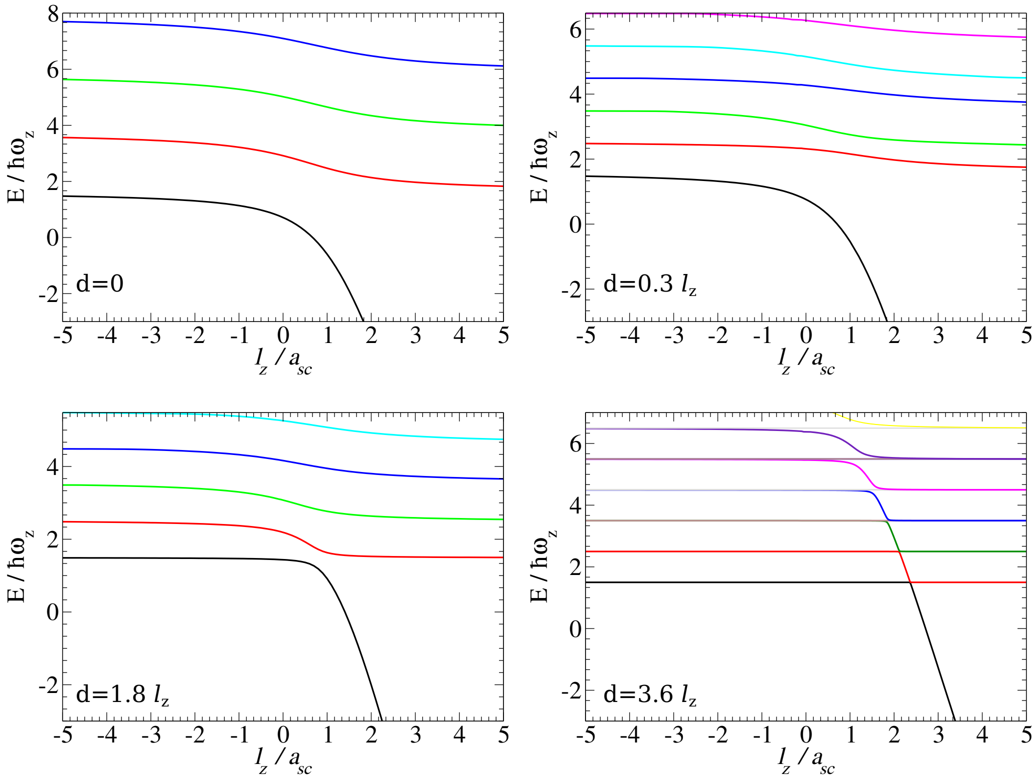

Figure 6.10: The eigenenergy spectrum for the hybrid atom-ion system of Li_2^+ confined in an isotropic spherical harmonic trap potential as a function of the inverse scattering length for trap separations $d/l_z = 0, 0.3, 1.8, 3.6$. $l_z = \sqrt{\quad /(\mu\omega_z)}$ is the relative motion trap length along z direction. The spectrum for $d = 0$ was obtained with the basis set specified in Table E.3, while the basis set in Table E.4 was used for the remaining three calculations.

realistic manner. The interaction between the atom-ion pair can be controlled using the TIRs. It is possible to pass through the resonance adiabatically by slowly varying the distance between the two traps thus converting the trap vibrational states into molecular bound states. Another application of this kind of resonances is in the production of ultracold molecular ions for species where sympathetic cooling using ultracold neutral atoms is not effective or possible.

Even though only the case for the identical trap frequency for the atom and ion traps have been discussed, the basic feature of the trap-induced resonance should remain unchanged when trap frequencies are different. In fact, for the most general case of different trap frequencies, the center-of-mass and relative-motions are coupled already at zero separation. This coupling of the r.m and

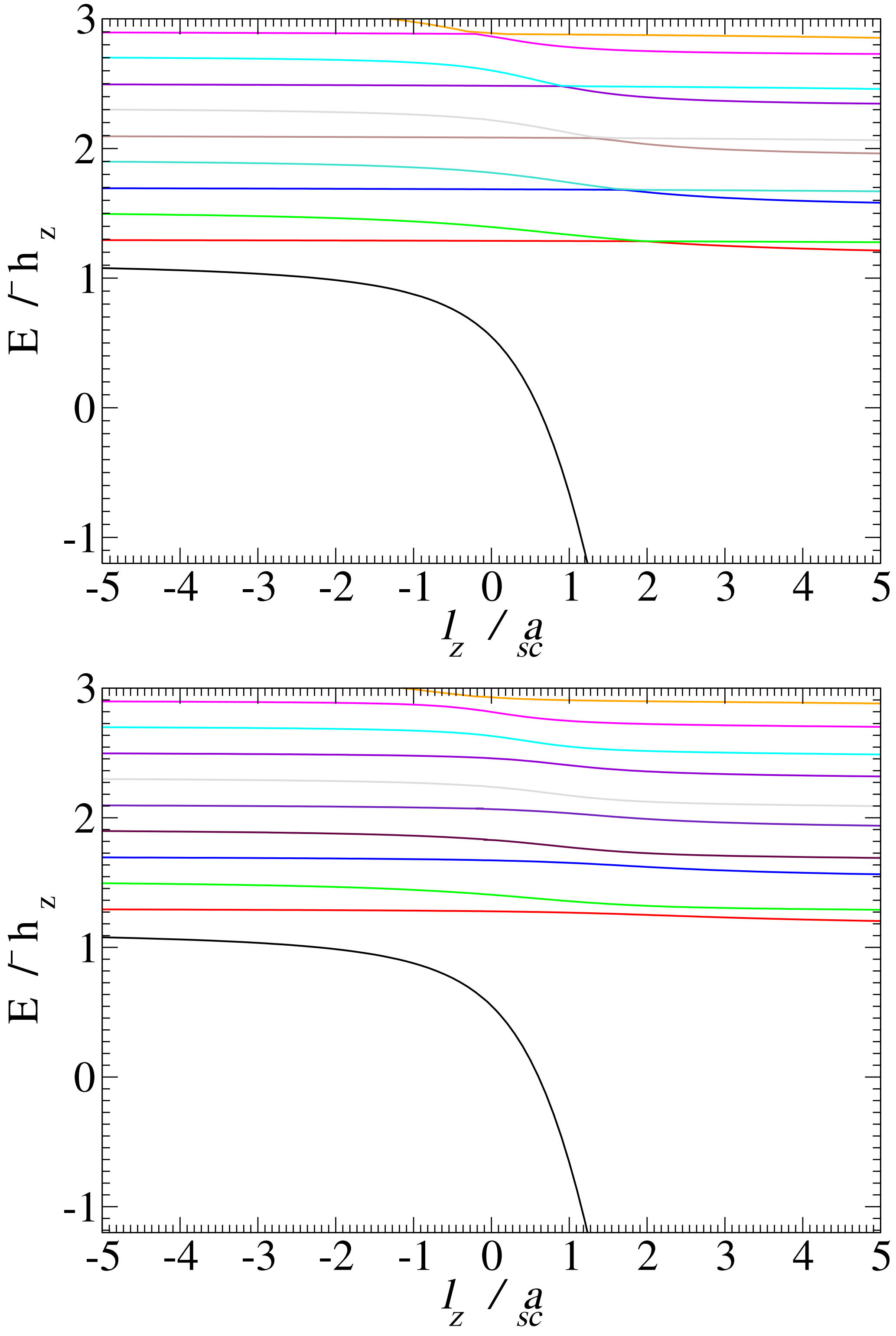

Figure 6.11: Energy spectrum for interacting atom-ion pair in harmonic traps for $\omega_x = \omega_y = 5\,\omega_z$ and trap separations $d = 0$ (top) and $d = 0.3\,l_z$ (bottom). Both spectra were calculated using the basis set specified in Table E.4.

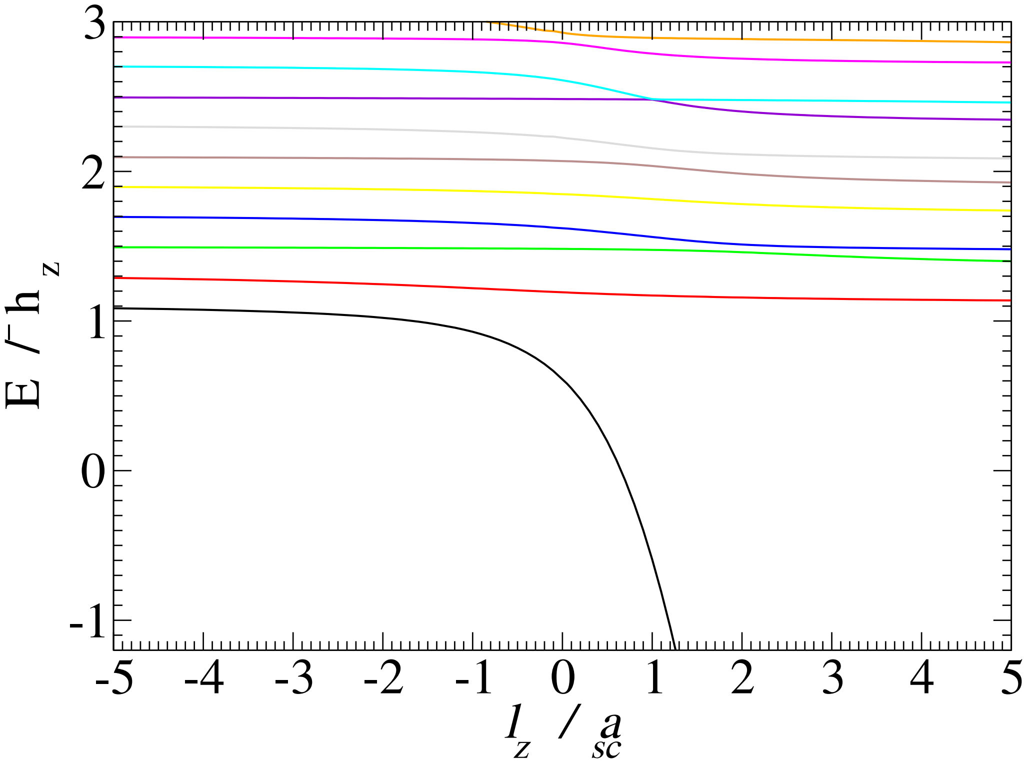

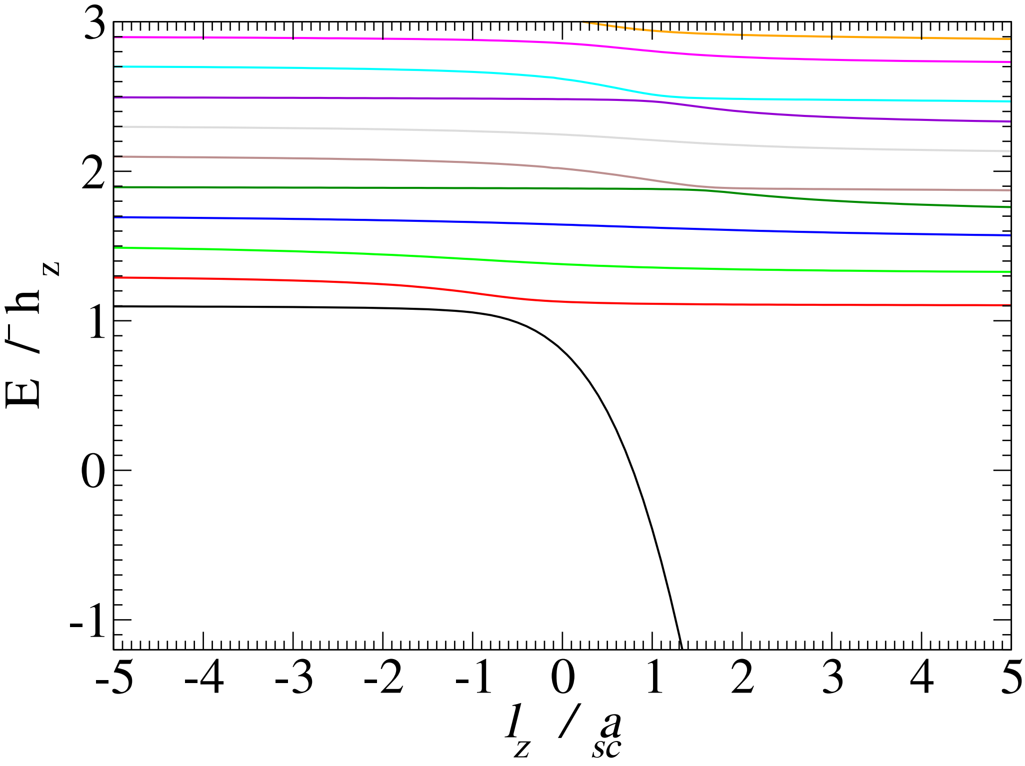

Figure 6.12: Energy spectrum for interacting atom-ion pair in harmonic traps for $\omega_x = \omega_y = 5\,\omega_z$ and trap separations $d = 1.8\,l_z$ (top) and $d = 3.6\,l_z$ (bottom). The spectrum for $d = 0$ and $d = 0.3\,l_z$ were calculated using the basis set specified in Tables E.5 and E.6, respectively.

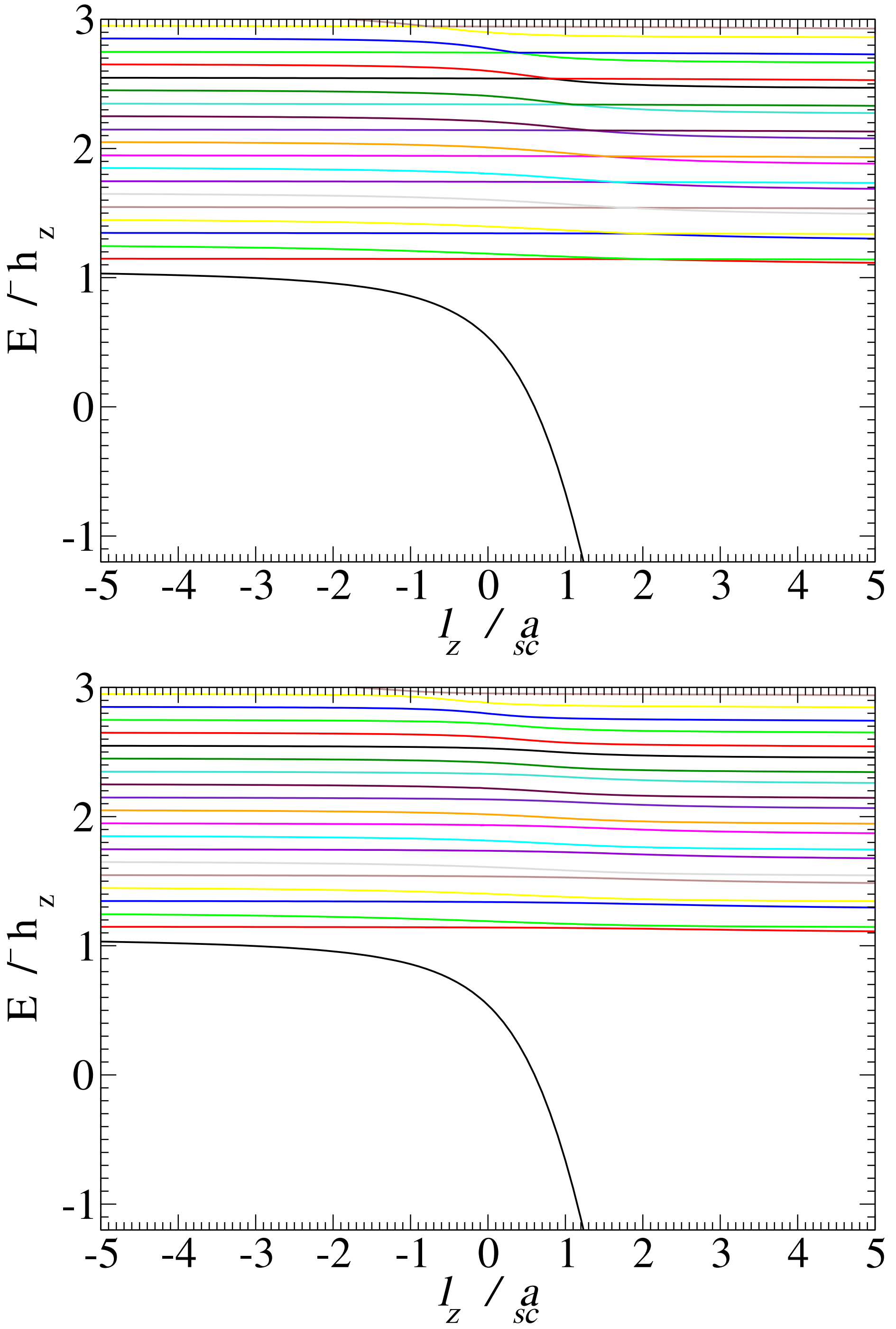

Figure 6.13: Energy spectrum for interacting atom-ion pair in harmonic traps for $\omega_x = \omega_y = 10\,\omega_z$ and trap separations $d = 0$ (top) and $d = 0.3\,l_z$ (bottom). The spectrum for $d = 0$ and $d = 0.3\,l_z$ were calculated using the basis set specified in Tables E.4 and E.6, respectively.

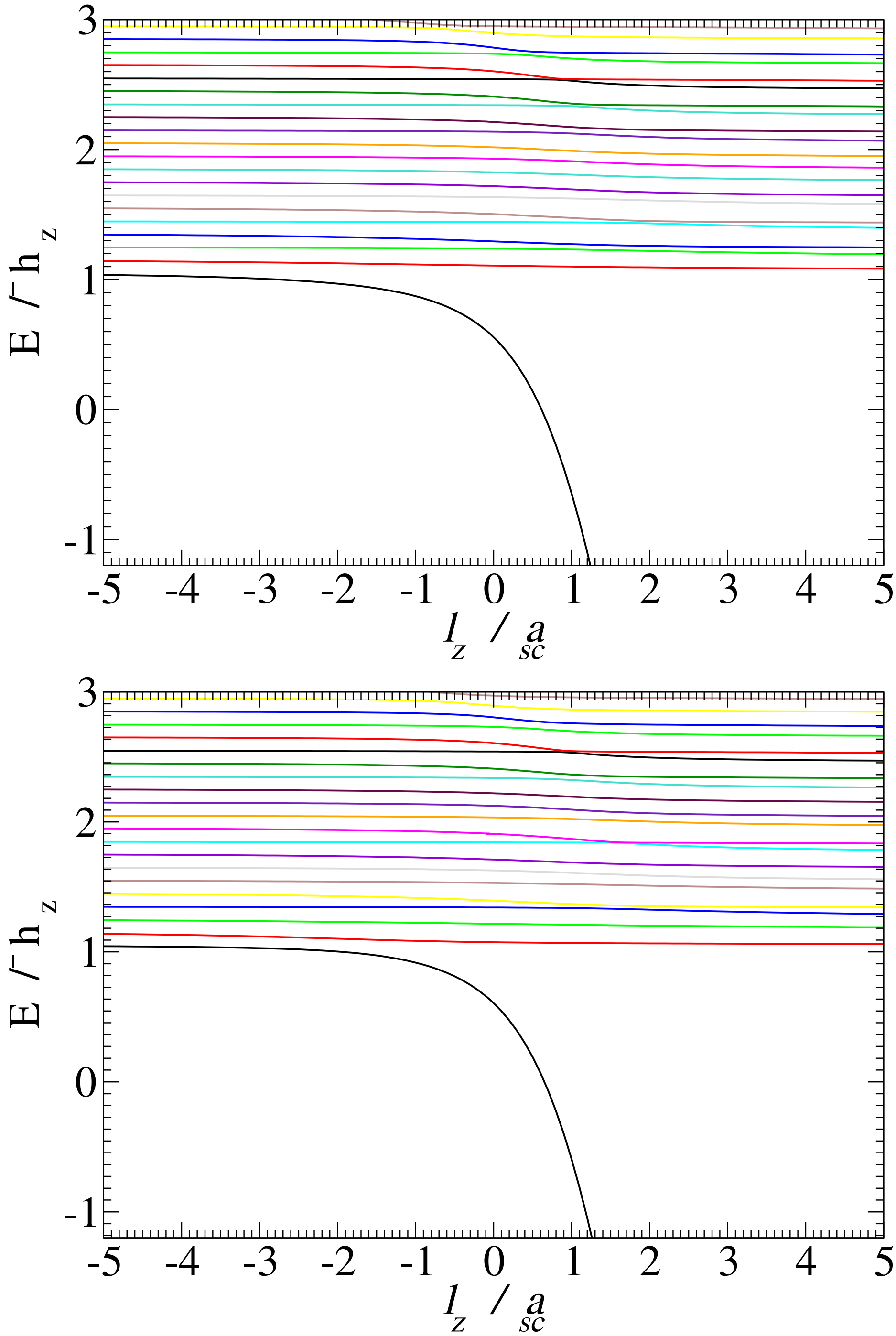

Figure 6.14: Energy spectrum for interacting atom-ion pair in harmonic traps for $\omega_x = \omega_y = 10\,\omega_z$ and trap separations $d = 1.8\,l_z$ (top) and $d = 3.6\,l_z$ (bottom). Both spectra were calculated using the basis set specified in Table E.7.

c.m. leads to another kind of resonance known as the inelastic confinement-induced resonances. These inelastic confinement-induced resonances have been reported in ultracold neutral atoms [125, 126], dipolar gases [127] and Coulombic systems [128]. It is shown in the next chapter that they are also present in atom-ion systems.

Chapter 7

Atom-Ion Inelastic Confinement-Induced Resonances

It has been shown that the coupling of center-of-mass and relative motion for a system of two ultracold neutral atoms in single-well potentials leads to *inelastic* confinement-induced resonances (ICIRs) [125]. These resonances were confirmed in a dedicated experiment [126] where it was established that the c.m.-rel. coupling leads to coherent molecule formation, losses, and heating in ultracold neutral atomic gases. The ICIRs are universal and have since been demonstrated to be present in collisions of atomic species with dipolar magnetic interactions [127], and in Coulomb-interacting systems such as excitons in quantum-dot systems [128]. In this chapter, the existence of ICIRs in atom-ion systems is demonstrated. The significance of these ICIRs relies on their potential use as a tool to control the interactions between ultracold neutral atoms and ions. In addition, the ICIRs can be manipulated via a variation of the scattering length and the geometry of the trap. Therefore, they could provide an alternative strategy that can be used to experimentally determine the atom-ion scattering length in the vicinity of the ICIR.

In the following discussions, the coupling between the center-of-mass and relative motion is realized in two ways: sextic potentials resulting from a Taylor expansion of a $\sin^2$-like potential up to the sixth degree, and harmonic trapping potentials with different frequencies. The atom and the ion traps are both centered at the origin and the original method [73] reviewed in Chapter 3 is used to describe the two particles. Since it has been established that the most pronounced ICIRs are contained in the lowest-lying state [129], and that the ICIR involving the ground trap state are contained in the A_{g} spectrum, only the spectra of A_{g} symmetry are presented in this chapter. Like in the previous chapter, a generic example for the realistic atom-ion interaction is modeled using the *ungerade* electronic state of the Li_2^+ potential.

The remainder of the chapter is organized as follows. First, the basic concepts of confinement-induced resonance (CIR) [130] are recapitulated in section 7.1. This kind of resonance will be referred to as *elastic* CIR following [129] to distinguish it from the *inelastic* CIR which will be described in section 7.2. The results are discussed in section 7.3 where the *ab initio* calculations showing the presence of *inelastic* CIR in hybrid mixture of an ultracold neutral atom and an ion in sextic and harmonic traps are discussed in sections 7.3.1 and 7.3.2, respectively. Finally, the chapter ends with a brief summary and an outlook in section 7.4.

7.1 Elastic confinement-induced resonances

The interest in low-dimensional quantum systems arises from their fascinating phenomena not encountered in three dimensions e. g., a one-dimensional (1D) gas of impenetrable Bosons, the Tonks-Girardeau (TG) gas [131, 132], acquires Fermionic properties [133–135]. In 1998, Olshanii considered a two-body s-wave scattering problem in a quasi-1D harmonic trap with symmetric transversal confinement. He developed a mapping of the relative-motion Hamiltonian

$$h_{\rm rel.} = -\frac{\hbar^2}{2\mu}\nabla_r^2 + \frac{1}{2}\,\mu\Big[\omega_\perp^2\rho^2 + \omega_z^2 z^2\Big] + \frac{4\pi\hbar^2 a_{\rm sc}}{m}\delta(\mathbf{r})\frac{\partial}{\partial r}r\,, \tag{7.1}$$

where $\rho^2 = x^2+y^2$ and $\omega_\perp$ is the transversal confinement onto the corresponding pure 1D Hamiltonian

$$h_{\rm 1D} = -\frac{\hbar^2}{2\mu}\nabla_z^2 + \frac{1}{2}\mu\,\omega_z^2 z^2 + g_{\rm 1D}\,\delta(z)\,, \tag{7.2}$$

where $g_{\rm 1D}$ is the coupling strength defined by [130]

$$g_{\rm 1D} = -\frac{\hbar^2}{\mu\,a_{\rm 1D}} = \frac{2\,a_{\rm sc}\,\hbar^2}{\mu\,d_\perp^2}\frac{1}{1+\zeta(\frac{1}{2})\frac{a_{\rm sc}}{d_\perp}}\,. \tag{7.3}$$

Here, $d_\perp = \sqrt{\hbar/(m\,\omega_\perp)}$ is the harmonic-oscillator trap length along the transversal direction, $a_{\rm 1D}$ is the one-dimensional scattering length, and $\zeta(x)$ is the Hurwitz zeta function. In equation (7.1), $a_{\rm sc}$ is the 3D s-wave scattering length as before, while m is the atomic mass, and the last term is the atom-atom interaction which is approximated by a contact Fermi pseudopotential.

In a quasi-1D confinement, $\omega_\perp \gg \omega_z$, therefore, only the ground state of the transversal motion is significantly populated. The Hamiltonian for a pure 1D confinement say along the z direction is given by (7.2). An elastic CIR resonance occurs when the three-dimensional scattering length $a_{\rm sc}$ approaches the characteristic trap length $d_\perp$ i. e., when one maps the effective 1D coupling strength constant $g_{\rm 1D}$ of 1D to the 3D s-wave scattering length $a_{\rm sc}$, then at the specific ratio

$$\frac{d_\perp}{a_{\rm sc}} = -\zeta\left(\frac{1}{2}\right) \approx 1.4603\ldots\,, \tag{7.4}$$

the coupling constant $g_{\rm 1D}$ in equation (7.3) diverges leading to the (elastic) *confinement-induced resonance* [130, 136]. These elastic CIRs are universal and independent of the atomic species. They depend solely on the geometry of the trap and can be used to tune the effective interparticle interaction. An analogous derivation of the effective two-dimensional interaction strength $g_{2\mathrm{D}}$ by Petrov et al. in Ref. [137] showed similar divergence behavior. The experimental evidence of elastic CIRs have since been reported for bosonic [133–135] and fermionic [138] systems. These elastic CIRs are characterized by the properties of the relative-motion energy spectrum of systems of reduced dimensionality.

Recently, a study of elastic confinement-induced resonance for ultracold atom-ion systems was reported in Ref. [139]. In that work, elastic CIR in a system consisting of a tightly trapped ion and a moving neutral atom in a waveguide was theoretically investigated. The conditions for the appearance of elastic CIR in ultracold atom-ion systems is investigated for two regimes. First, when the characteristic interaction length is much less than the length of the transverse harmonic trap, i. e., when $R^* \ll d_\perp$, the position of the elastic CIR is at

$$\frac{d_\perp}{a_{\mathrm{sc}}} = 1.4603 - 0.6531\left(\frac{m_{\mathrm{a}}}{\mu}\right)\left(\frac{E_{||}}{\omega_\perp}\right). \tag{7.5}$$

The second case when $R^* \gg d_\perp$, the CIR position is given by

$$\frac{d_\perp}{a_{\mathrm{sc}}} = 1.4603 + \Delta\left(\frac{R^*}{d_\perp}\right) - 0.32655\left(\frac{m_{\mathrm{a}}}{\mu}\right)\left(\frac{d_\perp}{R^*}\right)^2\left(\frac{E_{||}}{E^*}\right) \tag{7.6}$$

where m_{a} is the atomic mass, μ is the reduced mass for the atom-ion pair, $E_{||}$ is the longitudinal energy, while R^* and E^* denote the characteristic length and energy, see equations (2.48) and (2.47). The term $\Delta\Big(R^*/d_\perp\Big)$ in equation (7.6) denotes the shift in the position of elastic CIR with increase in the ratio $R^*/d_\perp$. Unlike the resonance position given by (7.4), the position of the elastic CIR given by equations (7.5) and (7.6) for an atom-ion pair depends on the ratio of the masses between the two species.

7.2 Inelastic confinement-induced resonances

The origin of the inelastic CIRs can be traced back to the debate initiated from the observations of the experiment reported in Ref. [140]. In that experiment, loss features close to the elastic CIR were observed in strongly interacting quantum gas of ^{133}Cs atoms in an isotropic quasi-1D confinement. However, when an anisotropy was introduced in the transversal confinement, a splitting of the CIR was observed, (as shown in Figure 7.1). This splitting could not be explained by the theory of elastic CIR [130, 136] that predicts only one elastic CIR, red dashed line in Figure 7.1, regardless on how large the transverse anisotropy. Also, in the same experiment of Haller et al. [140], a resonance was observed for repulsive ($a_{\mathrm{sc}} > 0$) interaction in quasi-2D confinement. In another

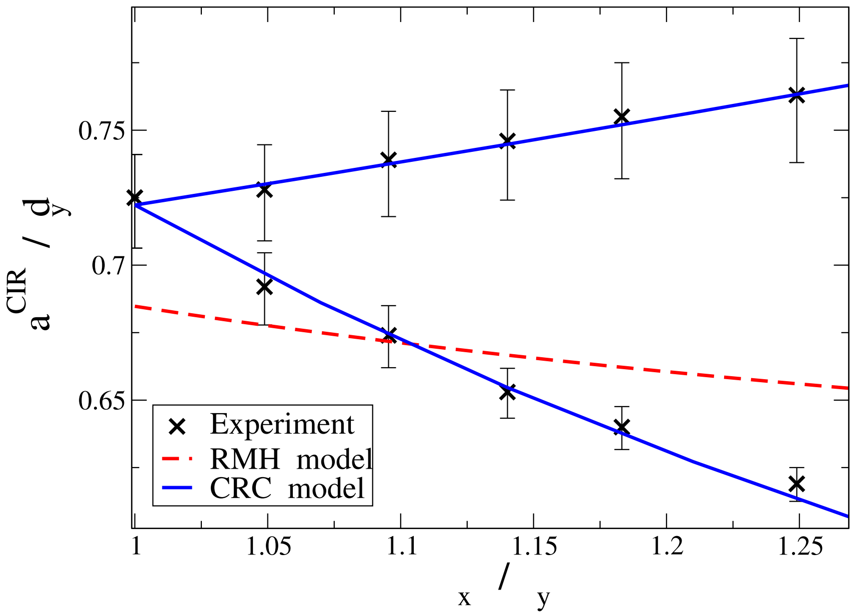

Figure 7.1: Positions of confinement-induced resonances as a function of the scattering length for different values of transversal anisotropy in quasi-1D. The experimental positions are compared to the predicted confinement-induced resonance positions of the Olshanii model of elastic confinement-induced resonance (RMH model) [130] and the inelastic confinement-induced resonance (CRC model) [125]. Plot taken from [125].

experiment adopting radio-frequency spectroscopy by Fröhlich et al. [141], a resonance was observed for attractive ($a_{\mathrm{sc}} < 0$) interactions in quasi-2D confinement. The observation of the resonance for positive scattering length in quasi-2D confinement in Ref. [140] was in contradiction to previous theoretical studies on 2D systems that predicted the appearance of an elastic CIR only for attractive but not repulsive interactions [137, 142]. Furthermore, a theoretical investigation of elastic CIR under transversely anisotropic confinement [97] found a discrepancy between Olshanii's model [130, 136] and experiment [140].

These contradictions between theory and experiment, namely, the splitting of the elastic CIR for transversal anisotropy in quasi-1D and the observed resonance for quasi-2D confinement for repulsive interactions were eventually explained using the theoretical model, denoted by CRC (blue line) in Figure 7.1, first introduced in [125]. This model agreed with the observed splitting of the resonance with increasing anisotropy in the transversal confinement in Ref. [140]. It was established that the observed resonances originated from the possible molecule (dimer) formation due to the coupling of the center-of-mass and relative-motions. The splitting of the resonance was established to be due to the transversal anisotropy of the trap states that make the crossings nondegenerate.

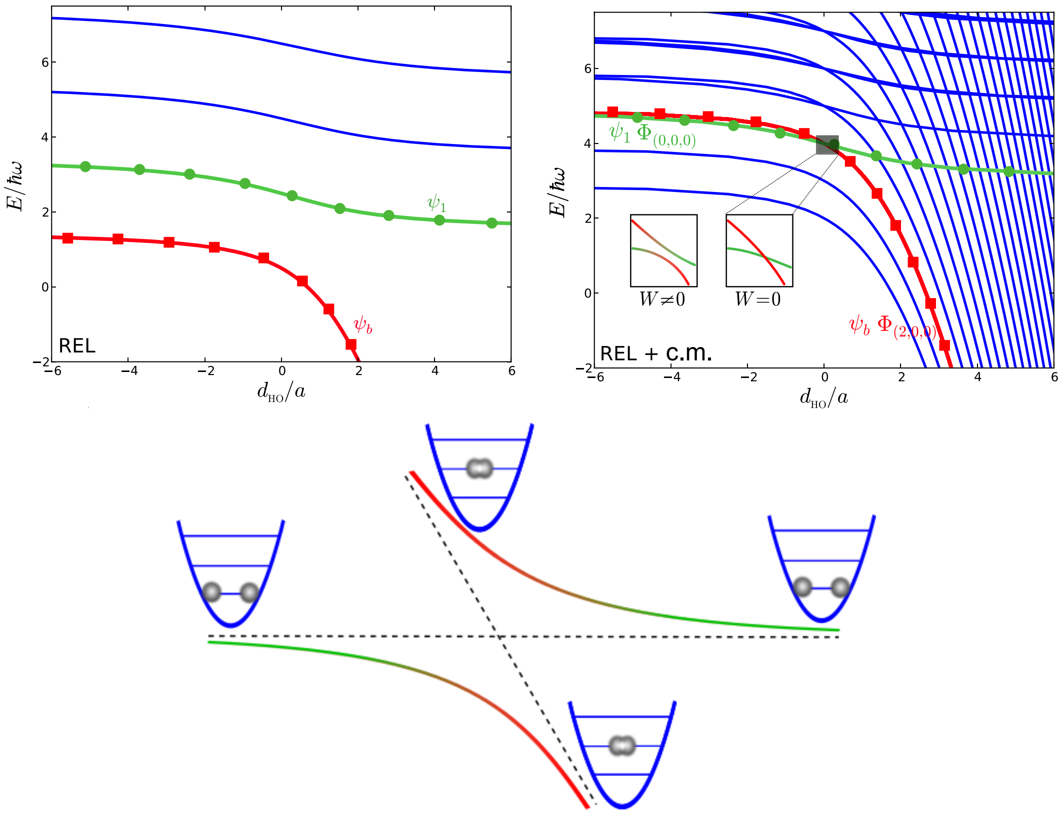

Figure 7.2: The energy spectrum illustrating the mechanisms of inelastic confinement-induced resonances. Top left plot shows the relative-motion eigenenergy spectrum for two neutral atoms interacting via a δ pseudopotential and confined in a 3D harmonic trapping potential as a function of inverse scattering length scaled by the harmonic oscillator length d_{H0}. Top right is the complete spectrum that includes the center-of-mass excitations. When the c.m.-rel. coupling $W = 0$, the trap and the molecular bound states with the c.m. excitations cross diabatically. A non vanishing coupling between the c.m. and rel. makes the crossings between the trap and the c.m. excitations become avoided. Lower plot shows a sketch of an avoided energy crossing between a trap state and a molecular bound state with c.m. excitation. Plots adopted from Ref. [129].

The plots in Figure 7.2 can be used to understand the mechanism of the ICIRs. The top left plot shows the eigenenergy spectrum of the relative-motion Hamiltonian (3.12) for a pair of ultracold neutral atoms confined in an isotropic harmonic trapping potential and interacting via the δ pseudopotential (2.42). The spectrum consists of a bound state (red line labeled ψ_b) and the trap states (the almost horizontal lines, with the green line labeled ψ_1 being the lowest-lying trap state). The plot on the top right shows the spectrum for the full Hamiltonian (3.10) where the center-of-mass energies have been included. From the inserts of the complete energy spectrum (top right), when the coupling $W = 0$, the trap states and the molecular bound states with center-of-mass excitations cross diabatically. However, when a coupling is introduced, i. e., $W \neq 0$, for example two identical particles confined in harmonic trapping potentials with different frequencies, the crossings become avoided allowing for an adiabatic transition of the trap state into a molecular state (see bottom panel of Figure 7.2). It is this c.m.-rel. coupling that leads to the *inelastic confinement-induced resonances* [125, 129]. The molecular states at the ICIR are true eigenstates of the full Hamiltonian (3.10) and couple with the trap state with c.m. excitations. Unlike the elastic CIRs where only a single resonance is present, a number of resonances occur in the case of inelastic CIRs due to the infinite number of center-of-mass excitations [129]. A detailed description of the theory of the inelastic confinement-induced resonances for a pair of ultracold neutral atoms in single- and multi-well potentials can be found in Ref. [143].

7.3 Results and discussion

Having described the basics of the ICIRs, the *ab initio* results are discussed in this section. Following previous studies [125–129] of the ICIRs in single-well potentials, it is natural to consider the effects of the anharmonicity of the trap potential by using sextic potentials (see Figure 3.1). Sextic potentials provide a good approximation for describing the c.m.-rel. coupling in single-well potentials [113]. Moreover, sextic potentials are well suited for the description involving an all optical trapping of the ions e. g., 3D optical trapping of single ions in OL [66]. As has already been pointed out, the c.m.-rel. coupling is also present in the case of identical particles seeing different trapping potentials and in heteronuclear atoms [144] in harmonic confinement. This particular case is investigated by considering a neutral atom and a single ion both confined in harmonic trapping potentials with different trap frequencies.

7.3.1 Quasi-1D sextic trapping potential

The sextic potentials are obtained by Taylor expanding the $\sin^2$-like potential equation (3.2) up to the sixth degree. The corresponding trap potential in c.m.-rel. coordinates (for zero trap separation) is expressed as

$$V(\mathbf{R}\,,\mathbf{r}\,) = V_{\text{c.m.}}(\mathbf{R}\,) + V_{\text{rel.}}(\mathbf{r}\,) + W(\mathbf{R},\mathbf{r}\,)\,, \tag{7.7}$$

with the individual components given by

$$V_{\text{c.m.}}(\mathbf{R}\,) = \sum_{c=x,y,z} V_c \left[2k_c^2R_c^2 - \frac{2}{3}k_c^4R_c^4 + \frac{4}{45}k_c^6R_c^6\right], \tag{7.8}$$

$$V_{\text{rel.}}(\mathbf{r}\,) = \sum_{c=x,y,z} V_c \left[\frac{1}{2}k_c^2r_c^2 - \frac{1}{24}k_c^4r_c^4 + \frac{1}{720}k_c^6r_c^6\right], \tag{7.9}$$

$$W(\mathbf{R},\mathbf{r}\,) = \sum_{c=x,y,z} V_c \left[-k_c^4R_c^2r_c^2 + \frac{1}{3}k_c^6R_c^4r_c^2 + \frac{1}{12}k_c^6R_c^2r_c^4\right]. \tag{7.10}$$

The full six-dimensional description of the atom-ion problem is performed following the procedure outlined in Chapter 3, i. e., the trap potentials equations (7.8) and (7.9) are respectively substituted in the Hamiltonian equations (3.11) - (3.12) then transformed to spherical coordinates. The product of the solutions (orbitals) of the resulting Schrödinger equations are then used to form configuration for incorporating the coupling part (7.10) of the full Hamiltonian (3.10).

7.3.1.1 Eigenenergy spectrum

In Figure 7.3 the eigenenergy spectrum of the relative-motion Hamiltonian equation (3.12) as a function of the inverse scattering length a_{sc} (scaled by the trap length $\text{d}_\perp$) for trap potential (7.9) is shown. The variation of the scattering length is done by continuously varying the repulsive steep inner wall part of the *ungerade* electronic state of $^7\text{Li}^+ - {}^7\text{Li}$ potential curve as described in Chapter 5. This variation represents a single-channel model for mimicking the variation of the s-wave scattering length at a Feshbach resonance [100]. The trap specification parameters gives an anisotropy ratio of $\omega_x = \omega_y = 10\,\omega_z$ which is well within the quasi-1D regime [95]. The relative-motion spectrum has a bound state (red line) bending downwards to negative infinity as $a_{\text{sc}} \to 0^+$ and trap states represented by the almost horizontal lines. The green line in Figure 7.3 is the first trap state.

Figure 7.4 shows the energy spectrum of the full coupled Hamiltonian (3.10). The c.m. energies are added to each of the relative-motion energies leading to an infinite number molecular bound states (all states bending downwards to $-\infty$).

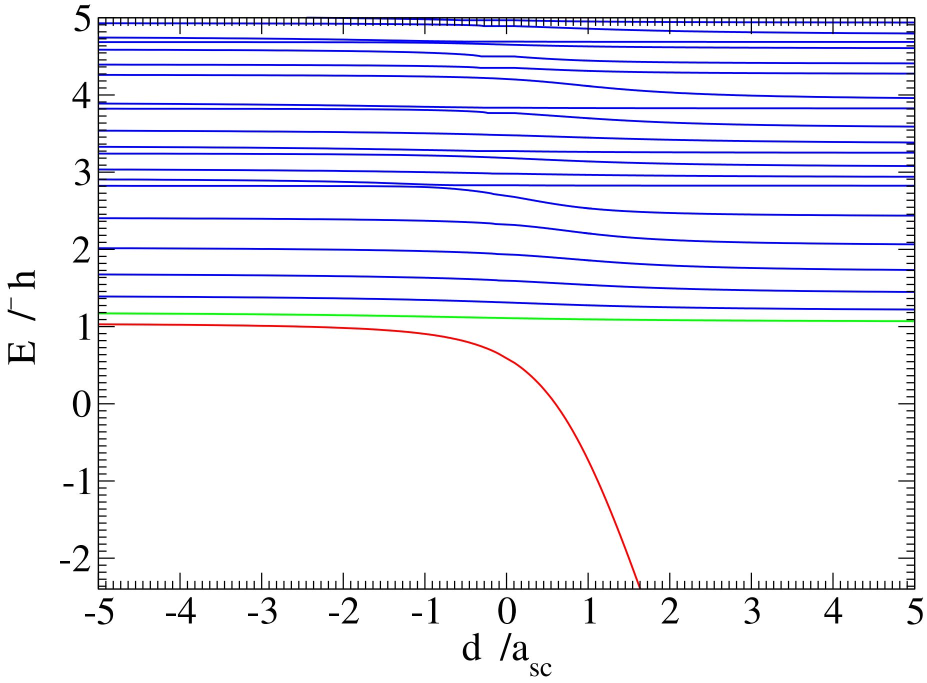

Figure 7.3: Relative-motion eigenenergy spectrum for the hybrid atom-ion system of ^{7}Li$^+$ - ^{7}Li pair confined in sextic trap potential for a varying s-wave scattering length. The parameters for the trap potential are: wavelength $\lambda_x = \lambda_y = \lambda_z = 1000$ nm, intensity $I_x = I_y = 5000$ W cm^{-2} and $I_z = 50$ W cm^{-2} giving a potential depth of $29.477\,E_r$ in the x and y directions and $0.295\,E_r$ in the z direction. The basis set used for the calculation is specified in Table E.8.

The plot on the right is the magnified part showing the avoided crossing that is responsible for the inelastic CIR. The labels (a) - (b) on the zoomed part of Figure 7.4 are only used to denote the positions of the wavefunctions for the atom-ion pair to be discussed later in section 7.3.1.2. The crossings between the ground trap state and the transversely excited bound state becomes avoided at around $\mathrm{d}_\perp/a_{\mathrm{sc}} \approx 1.007$, the approximate position of the ICIR. If one presumes a loss experiment involving a single ultracold neutral atom and an ion, when an inelastic CIR is observed for example when the ratio of the trap length to the scattering length is say 1.007, then the value of the scattering length can be determined using this information.

In this example calculation, an isotropic transversal confinement trapping has been used hence only a single resonance is observed due to the degeneracy of the transversal excitation. If a transition is made to the nondegenerate case, i. e., an anisotropic transverse confinement where $\omega_x \neq \omega_y \gg \omega_z$, then a splitting of the resonance is observed in the eigenenergy spectrum. This transition to anisotropic confinement can be applied in understanding the

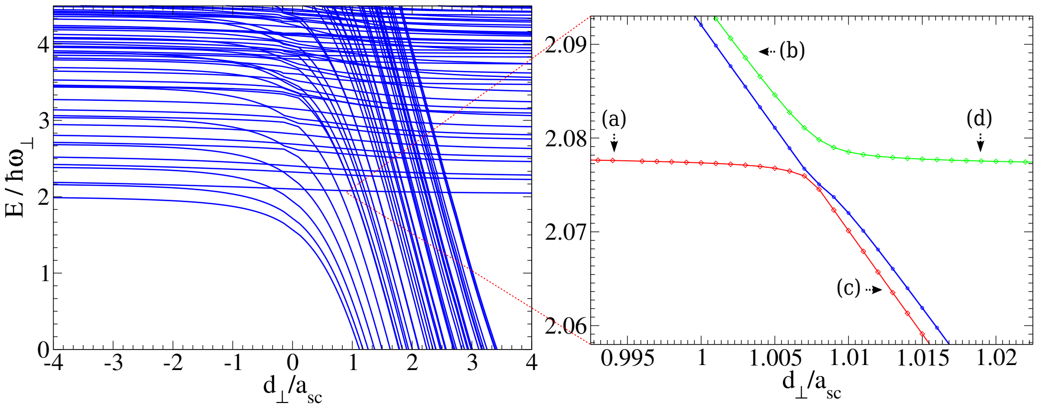

Figure 7.4: Eigenenergy spectrum of the full Hamiltonian for Li_2^+ pair confined in identical sextic trapping potentials. The magnified view on the right shows the avoided crossings that causes the inelastic CIRs. For this particular example, the most pronounced resonance occurs at $\mathrm{d}_\perp/a_{\mathrm{sc}} \approx 1.007$. Converged CI calculations were obtained using the basis specifications given in Table E.8.

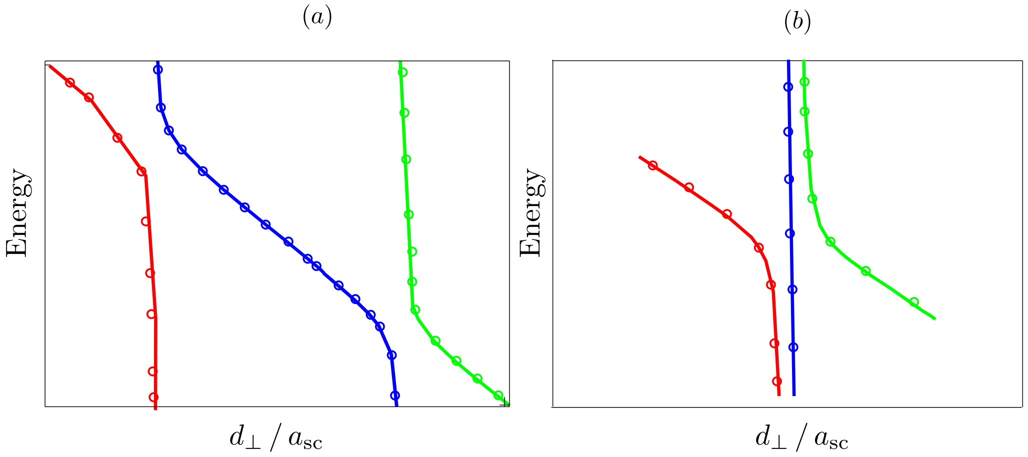
(a)

(b)

Figure 7.5: Sketch illustrating the transition from an anisotropic transverse confinement (a) to the case of isotropic confinement (b).

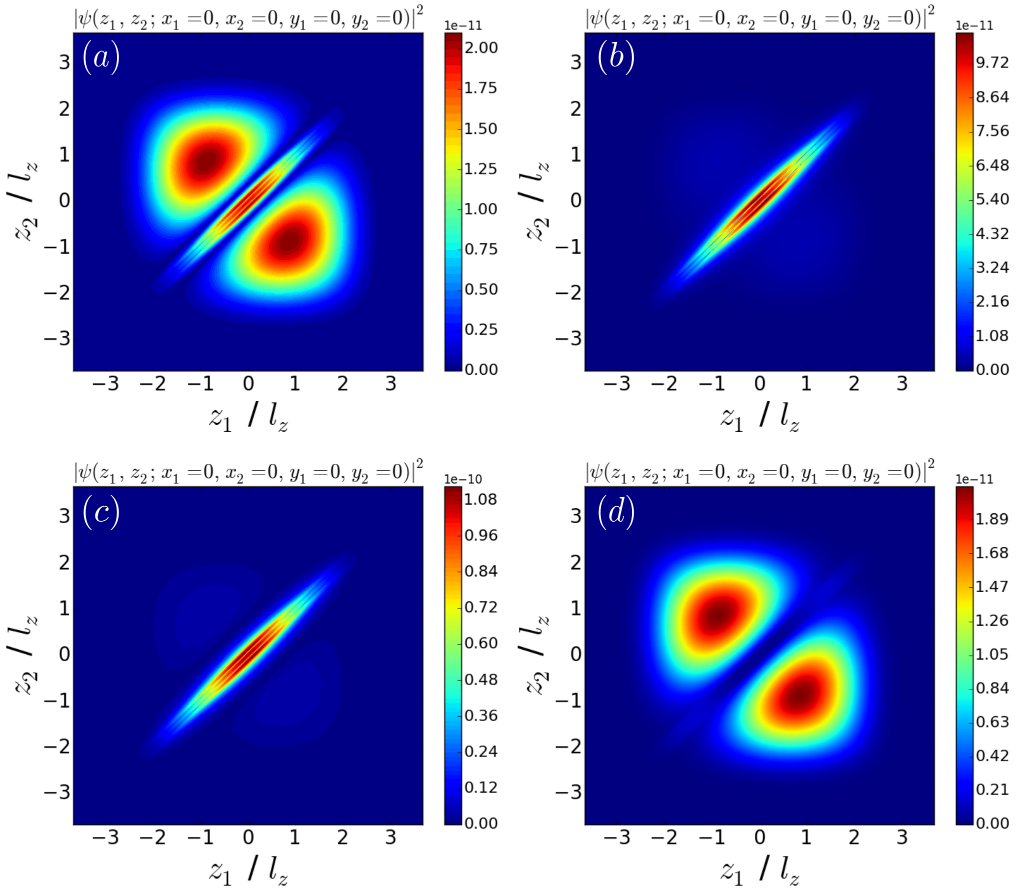

Figure 7.6: Cuts through the wavefunction density along the x-y plane ($|\Psi(z_1, z_2; x_1 = x_2 = y_1 = y_2 = 0|^2$) for the states labeled (a)-(d) in Figure 7.4. The plots have been scaled by the trap length l_z along the z direction. In (a) and (d), the atom-ion pair are unbound. When the two particles pass through the crossing adiabatically, they transform into bound states, marked (b) and (c) and they posses no c.m. excitations.

physical interpretation of the almost vertical blue line going through the avoided crossing in Figure 7.4. To visualize how the almost vertical line arise, consider the sketch shown in Figure 7.5. On the left side is a case of nondegerate transverse excitation where the transversal confinement is anisotropic. As the degeneracy is lifted, the bending curve (blue line in Figure 7.5 (a)) is squeezed together until it becomes almost vertical (Figure 7.5 (b)) in the case of full degeneracy of the transverse excitation i. e., when the particles are experience a transverse isotropic confinement.

7.3.1.2 Wavefunction analysis

To conclude the discussions about the sextic trap confinement, the behavior of the *ab initio* wavefunctions are investigated for the states labeled (a) - (d) in Figure 7.4. These states are expressed by their corresponding six-dimensional wavefunctions in absolute coordinates as shown in Figure 7.6. The atom-ion pair in the state labeled (a) in Figure 7.4 are unbound when the ratio of the transversal confinement to scattering length $\mathrm{d}_\perp/a_{\mathrm{sc}} = 0.994$. This is seen in the cut though the trap state density along the z direction of the full 6D *ab initio* wavefunction in the top panel (Figure 7.6 (a)). For this interaction strength, the atom-ion pair exhibit a large probability to be off-diagonal i. e., they are separated from each other away from the trap elongation direction. As the interaction strength reduces, the repulsion between the atom-ion pair decreases and they get closer and closer forming a molecular bound state at $\mathrm{d}_\perp/a_{\mathrm{sc}} = 1.013$ (plot labeled (c)). The occupation of bound state is only possible because the excess binding energy can be transferred into the center-of-mass excitation energy [125, 129]. This redistribution of the binding energy is an inelastic process and that is why the resonances induced by the c.m.-rel. coupling are called inelastic CIRs [125]. From the states labeled (a) and (c), one sees how the unbound atom-ion pair transforms into a bound pair after passing through the crossing adiabatically. Similar observations hold for the state labeled (b) and (d) where $\mathrm{d}_\perp/a_{\mathrm{sc}} = 1.003$ and $\mathrm{d}_\perp/a_{\mathrm{sc}} = 1.019$, respectively. In this case, the bound atom-ion pair become unbound after crossing the resonance. Noteworthy, the bound atom-ion pair (Figure 7.6 (b) and (c)) posses no center-of-mass excitations in the z direction.

7.3.2 Quasi-1D harmonic trapping potential

In the following, the phenomena of inelastic CIRs is explored in atom-ion systems within the harmonic approximation of the trapping potentials. The coupling between the c.m. and rel. motions is achieved by considering two traps with different frequencies. Even though the typical values of the frequency in atom and ion traps are quite different, the considered coupling between the c.m. and rel. is relatively weak. This is because the coupled Hamiltonian matrices become much larger and harder to diagonalize with the increase in the coupling. The chosen ratio between the ion and atom trap frequencies ω_i/ω_a of 1.4 and 2 considered here were chosen such that the computational efforts are manageable.

To obtain the harmonic confinement for the atom and the ion, the $\sin^2$-like potential (3.2) is Taylor expanded around the origin up to the second order. The resulting form of the trap potential in c.m.-rel. coordinates takes a similar form as given in [144, 145] and is expressed as

$$V(\mathbf{R},\mathbf{r}) = \left[\frac{m_a}{2}\omega_a^2+\frac{m_i}{2}\omega_i^2\right]R^2+\left[\frac{m_a}{2}\omega_a^2\mu_i^2+\frac{m_i}{2}\omega_i^2\mu_a^2\right]r^2+\mu\left(\omega_a^2-\omega_i^2\right)Rr \quad (7.11)$$

where $\omega_j^2 = 2I_j\alpha_j k_j^2/m_j$ is the trap frequency for particle j, and the last term is the coupling part. Clearly, the coupling is present whenever $\omega_a \neq \omega_i$. In general, a difference in trap frequencies can be simulated by varying either the polarizability, intensity, or wavelength. Since the model atom-ion interaction considered involves homonuclear atoms, it is realistic to consider varying either the wavelength or the intensity. Either way, since the inelastic CIR is a phenomenon purely due to c.m.-rel. coupling, the results are independent of which parameter is modified to simulate different frequencies of the two traps. In the present case, the same intensity is used for both the atom and the ion while varying the wavelength of the two traps.

A case similar to that of sextic confinement discussed above is considered, i. e., an isotropic quasi-1D confinement with $\omega_x = \omega_y = 10\,\omega_z$. This is obtained using harmonic potential with parameters $I_x = I_y = 5000$ W cm^{-2} and $I_z = 50$ W cm^{-2} for both the atom and the ion. A wavelength $\lambda = 1000$ nm for the atom trap and $\lambda = 500$ nm for the ion trap results in a frequency difference $\omega_i/\omega_a = 2$. The relative-motion eigenenergy spectrum shown in Figure 7.7 is similar to that of the sextic trap (Figure 7.3). It has a single bound state (the state bending downwards to negative infinity as $a_{\text{sc}} \to 0^+$) and trap states represented by the almost horizontal lines. In Figure 7.8 the eigenenergy spectrum for the full Hamiltonian incorporating the c.m.-rel. coupling is shown. Again, the spectrum is similar to that of the sextic confinement and exhibits an infinite number of c.m. excitations. Because the two particles are trapped at different frequencies, the c.m. and rel. motions couple even within the harmonic approximation leading to an inelastic CIR. This is shown in the zoomed part on the right of Figure 7.8 where the coupling between rel. and c.m. motions makes the crossings avoided leading to an inelastic CIR at $\mathrm{d}_\perp/a_{\text{sc}} \approx 1.078$.

The existence of the inelastic CIR within harmonic approximation of the trap potential further demonstrates that the ICIRs are universal and occur whenever the c.m. and rel. motions do not separate. In Figure 7.9, a case when the atom and ion are trapped in harmonic potentials whose frequencies differ by a factor of 1.4 is presented. The potentials are modeled using the wavelengths of 1000 nm and 714 nm for the atoms and ion traps, respectively, and the same values of intensity I as the case of $\omega_i/\omega_a = 2$ above. For this ratio, the eigenenergy spectrum Figure 7.9 shows an inelastic CIR located at $\mathrm{d}_\perp/a_{\text{sc}} \approx 1.054$. The ICIR occurs at slightly stronger repulsive interactions when ratio ω_i/ω_a is 1.4 compared to when it is 2.0. Moreover, the resonance when the ratio $\omega_i/\omega_a = 2$ is slightly broader (0.01145 $\omega_\perp$) compared to when the ratio $\omega_i/\omega_a = 1.4$ which produces a resonance whose width is approximately

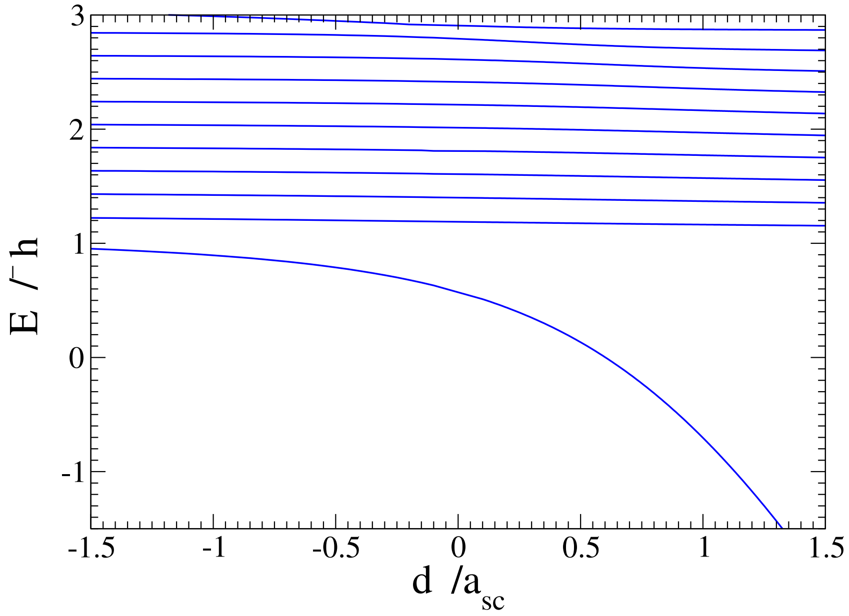

Figure 7.7: Relative-motion energy spectrum of an atom-ion of ^{7}Li$^+$-^{7}Li pair confined in harmonic trap potentials with the frequency ratio $\omega_i/\omega_a = 2$. The basis set used in the calculation is specified in Table E.9.

0.00181 $\omega_\perp$. In general, a stronger c.m.-rel. motion coupling of the c.m. excited bound states with trap states should lead to more broader inelastic resonances. The dependence of the ICIR position on the frequency is similar to that of the atom-ion elastic CIR that depends on the ratio of the masses. The wavefunction analysis for harmonic confinement is analogous to those presented for the sextic trap confinement in section 7.3.1. They are therefore not repeated. Finally, the adiabatic spectrum for two neutral ^{7}Li atoms confined in isotropic quasi-1D harmonic traps whose frequencies differ by a factor of two is shown in Figure 7.10. The inelastic CIR occurs at a larger ratio $\mathrm{d}_\perp/a_{\mathrm{sc}} \approx 1.348$ for the neutral atoms compared to the atom-ion case where the resonance is at $\mathrm{d}_\perp/a_{\mathrm{sc}} \approx 1.054$. This could be attributed to the long-range nature of atom-ion interactions compared to the neutral atom case.

7.4 Conclusion and remarks

In conclusion, it has been demonstrated that inelastic confinement-induced resonances are present in systems composed of ultracold neutral atoms and ions. The resonances occur due to the c.m.-rel. coupling of trap states and center-of-mass excited bound states. The coupling in the single-well potentials has been explored by considering anharmonic sextic traps as well as harmonic traps with

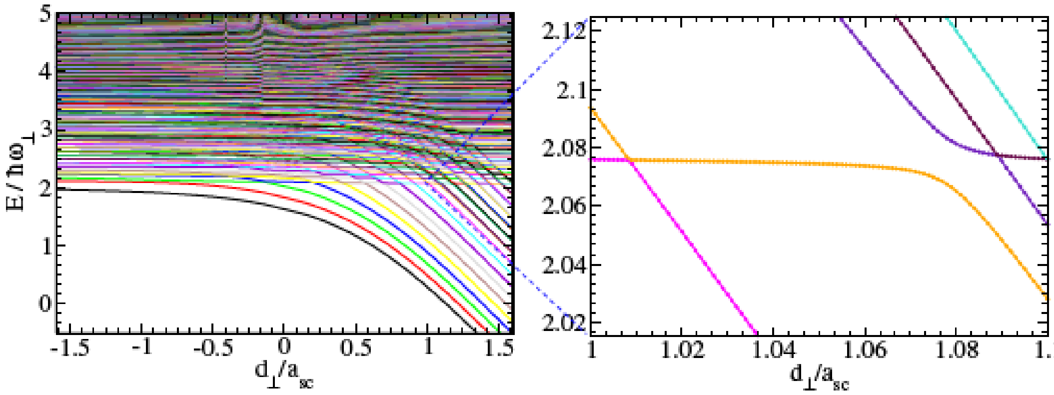

Figure 7.8: *Ab initio* energy spectrum for the full Hamiltonian of a neutral atom and an ion of ^{7}Li atom confined in a harmonic trap potential with $\omega_i = 2\omega_a$. The magnified part on the right shows the avoided crossing responsible for the inelastic CIR that occurs at $\mathrm{d}_\perp/a_{\rm sc} \approx 1.078$. The basis set used in the calculation is specified in Table E.9.

different frequencies. In both cases, the inelastic CIR has been observed in the *ab initio* eigenenergy spectrum as avoided crossings between the transversally excited bound and lowest trap states. Even though the discussions have focused only on single-well potentials with traversal isotropy, the features of inelastic CIRs are universal and analogous observations like those of the neutral atoms should be expected, for example, a splitting of the resonance in the case of an anisotropic trap confinement. These inelastic CIRs could be useful in offering an alternative means of controlling the interactions between neural atoms and ions especially now that the s-wave scattering regime has not been accessed experimentally. They can be used e. g., for the controlled transfer of atom-ion pair into a bound molecular state. The current study of the ICIR in atom-ion systems however, did not investigate in detail the relationships between the coupling of c.m.-rel. and resonance positions. It would be interesting to extend the studies towards developing a model that can predict the position and coupling strength of the inelastic confinement-induced resonances. Such a model could be useful compared to the numerically demanding full six-dimensional treatment used in this work. Also, it is important to remind that there exists an infinite number of center-of-mass excitations. Therefore, the a plethora of resonances occur where a bound state with a c.m. excitation crosses a trap state [129]. The inelastic confinement-induced resonances presented in Figures 7.9 and 7.4 are the most prominent ones.

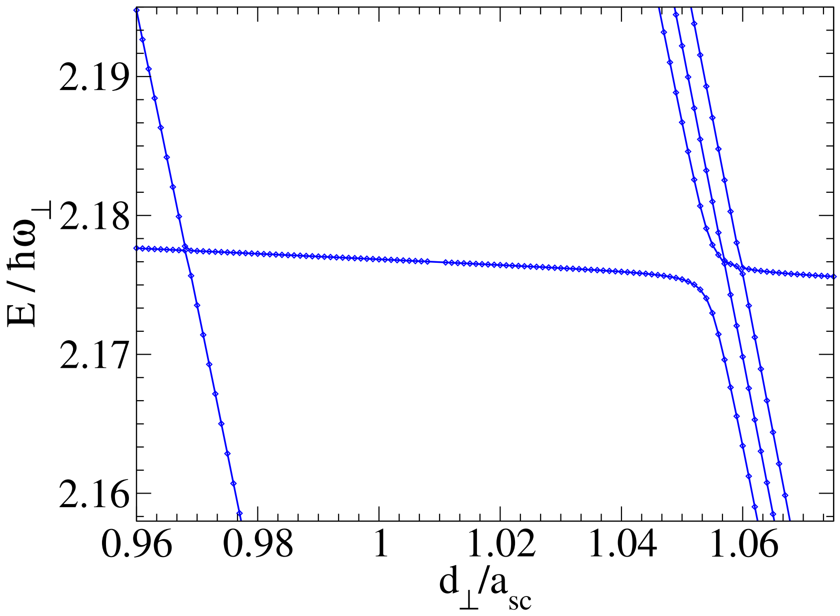

Figure 7.9: Similar to the enlarged view on the right of Figure 7.8 but with $\omega_i/\omega_a = 1.4$. The inelastic CIR occurs at $\mathrm{d}_\perp/a_{\mathrm{sc}} \approx 1.054$. The basis set used in the calculation is specified in Table E.10.

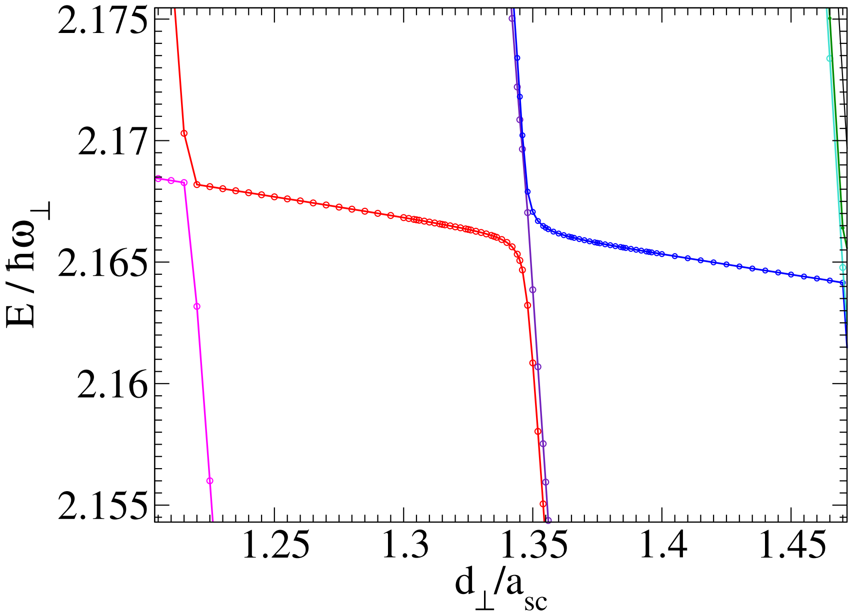

Figure 7.10: *Ab initio* energy spectrum for two *neutral* ^{7}Li atoms confined in isotropic quasi-1D harmonic trap with frequency between the two traps differing by a factor of 2. The ICIR occurs at $\mathrm{d}_\perp/a_{\mathrm{sc}} \approx 1.348$. The basis set used in the calculation is specified in Table E.11.

Chapter 8

Summary and Outlook

A theoretical model that allows for an accurate description of the controlled motion of a single ion through an optical lattice with ultracold neutral atoms was developed. The model eliminates the need to approximate the unknown short-range interaction details of the atom-ion pair. This is achieved by treating the interaction between the neutral atom and the ion using realistic interatomic interaction potentials given by Born-Oppenheimer curves. The coupling between center-of-mass and relative motion degrees of freedom due to the external trapping potentials is incorporated in a configuration-interaction fashion to solve the full six-dimensional Schrödinger equation.

The developed approach is based on the original model in [73]. However, in the original, both ultracold particles (atoms) were supposed to be trapped in optical lattices formed by the same standing laser fields. In order to simulate trapping conditions for an atom-ion pair where the trapping frequencies are generally different, the code was modified in such a way that the ion may be trapped in a tighter ion trap, while the neutral atom is positioned in a (finite) optical lattice. With this modification, it is possible to achieve different trap geometries for the atom and the ion. A convergence study was performed to explore the numerical stability of the code for various trapping frequency ratios. By comparing the analytical and numerical ground state energy for two noninteracting particles in harmonic trapping potentials with different frequencies, it was found that the convergence of the numerical eigenvalues improves with an increase of the CI basis. Furthermore, in order to account for the coupling, all symmetries have to be considered while forming the CI expansion. It was established that the coupled Hamiltonian matrices become much larger and harder to diagonalize with the increase in the ratio between the two traps.

A methodological achievement of the present study is the extension and implementation of the original code to incorporate the spatial displacement of the trap potentials. Even though higher and more efficient $D_{\infty h}$ and $C_{\infty v}$ symmetries could have been used in the symmetry implementation in the code, coding and implementing the C_{2v} symmetry was reasonably not so demanding because the original method that was designed for orthorhombic symmetry of the optical lattice. Using this new code to study a system of ultracold neutral atom and an ion in harmonic trap potentials

The interaction between a neutral atom and a single ion was modeled using the *ungerade* electronic state of Li_2^+ potentials recently published in [81]. The choice for this particular state was motivated by the fact that it is shallow supporting few bound states thus relatively less number of B splines are required to describe the interaction range with this state. The other reason why this state was chosen is because its s-wave scattering length value, calculated from the point of intersection of extrapolated radial asymptotic wavefunction and the r axis compares well with those reported in literature [45, 122]. A code was developed to mimic the single-channel approach [100] for the Li_2^+ potentials. This stage took a considerable amount of time while mapping the inner shift to the corresponding scattering length values. It was established that the construction of the complete potential curves has to be done carefully to obtain a smooth fit between the short- and long-range parts of the interaction.

An application of the modified codes to the case of atom-ion systems was performed in which the two particles are confined in separated harmonic trapping potentials. The eigenenergy spectrum for the hybrid atom-ion system of the $^7\mathrm{Li}$ isotope reveals the expected trap-induced resonances. These resonances show up as avoided crossings between the molecular and vibrational trap states in the energy spectrum as a function of the trap separation. The findings are consistent with other theoretical studies based on quantum defect theory [72] thus validating the developed approach.

The other finding from the present study is the realization of the inelastic confinement-induced resonances in atom-ion systems. It was shown that this resonance exists even within harmonic approximation of the trapping potential when the trap frequencies for the two particles are different. This inelastic confinement-induced resonances could presently be useful in providing an alternative means of controlling the atom-ion interactions since the s-wave scattering regime has not been accessed experimentally. They could also offer a means of producing molecular ions for species where sympathetic cooling is not effective or possible.

Even though it was not feasible to simulate realistic atom-ion trapping like in experiments where the frequencies of the two particles differ by several orders of magnitude, the findings of the present study gives an overview on possible trap frequencies that can be handled by the program. One perspective that can be explored in future is how the inelastic confinement-induced resonances behave when the trap potentials are displaced relative to each other. This can be straightforwardly be performed without any modification to code. A similar study could be on the influence of the trap-induced resonances from the coupling of the center-of-mass and relative-motions. Generally, its observed features should remain but, as established for the inelastic confinement-induced resonances, the position and the size of the resonance are expected to change for different frequency ratio. A model that predicts the position and widths of the resonance would be useful compared to performing the time consuming and computationally demanding *ab initio* calculations.

Another interesting application where the method incorporating the trap displacement can be used is simulating a system of neutral atoms in polarization-synthesized optical lattices [117] where state-selective optical lattice shift can be realized by varying the lattice spacing between the atoms such that they are in different hyperfine states. This way, the lattice sites acts as storage and shift registers in atom-sorting schemes [118]. The developed model can be used to simulate a hybrid atom-ion simulator [55] where the quantum dynamics of a neutral atom in a double-well potential interacting with an ion in a single well can be investigated. The adiabatic simulation should in principle be straightforward even though this was not investigated and the present studies focused mainly on single-well potentials. Finally, a more natural extension of the program for the displaced traps is to include time-dependence. This is however not trivial but such an extension would go in hand in simulating for example a universal quantum gate by calculating the paths diabatically. A starting point could be the time-dependent extension of the original method [73] provided in Ref. [146].

Appendix A

Separation of the center of mass coordinates for a N-electron atom

Consider an atom (or an ion) whose nucleus has a charge Z and mass M, with N electrons of mass m. The kinetic energy operator of the atom can be written as

$$\hat{\mathrm{T}} = -\frac{{}^{2}}{2M}\,\nabla^2_{\mathbf{R}_0} + \sum_{i=1}^{N}\left(-\frac{{}^{2}}{2m}\,\nabla^2_{\mathbf{R}_i}\right) \tag{A.1}$$

where $\mathbf{R}_0$ denote the coordinates of the nucleus with respect to a fixed origin and $\mathbf{R}_i$ represent the coordinates of the electrons.

Introducing the relative-motion coordinates of the electrons with respect to the nucleus according to,

$$\mathbf{r}_i = \mathbf{R}_i - \mathbf{R}_0\,, \tag{A.2}$$

and the center-of-mass system of coordinates,

$$\mathbf{R} = \frac{M\mathbf{R}_0 + m\,\mathbf{R}_1 + m\,\mathbf{R}_2 + \cdots + m\,\mathbf{R}_N}{M + Nm}\,, \tag{A.3}$$

in the expansion of the first order Laplace operators appearing in equation (A.1), it can be shown using chain rule that

$$\nabla_{\mathbf{R}_0} \;=\; \left(\frac{M}{M+Nm}\right)\nabla_{\mathbf{R}} - \sum_{i=1}^{N}\nabla_{\mathbf{r}_i} \equiv \mu_M\,\nabla_{\mathbf{R}} - \sum_{i=1}^{N}\nabla_{\mathbf{r}_i}\,, \tag{A.4}$$

$$\nabla_{\mathbf{R}_i} \;=\; \left(\frac{m}{M+Nm}\right)\nabla_{\mathbf{R}} + \nabla_{\mathbf{r}_i} \equiv \mu_m\,\nabla_{\mathbf{R}} + \nabla_{\mathbf{r}_i}\,, \tag{A.5}$$

hence, the second order partial derivative become

$$\nabla^2_{\mathbf{R}_0} \;=\; \mu_M^2\nabla^2_{\mathbf{R}} - 2\,\mu_M\sum_{i=1}^{N}\nabla_{\mathbf{R}}\cdot\nabla_{\mathbf{r}_i} + \left(\sum_{i=0}^{N}\nabla_{\mathbf{r}_i}\right)^2 \tag{A.6}$$

$$\nabla^2_{\mathbf{R}_i} \;=\; \mu_m^2\nabla^2_{\mathbf{R}} + 2\,\mu_m\nabla_{\mathbf{R}}\cdot\nabla_{\mathbf{r}_i} + \nabla^2_{\mathbf{r}_i}\,. \tag{A.7}$$

Substituting the Laplace operator equations (A.6) and (A.7) into the kinetic energy equation (A.1) gives

$$\begin{aligned}
\hat{\mathrm{T}} &= -\frac{{}^{2}}{2M}\left[\mu_M^2\nabla_{\mathbf{R}}^2 - 2\,\mu_M\sum_{i=1}^{N}\nabla_{\mathbf{R}}\cdot\nabla_{\mathbf{r}_i} + \left(\sum_{i=0}^{N}\nabla_{\mathbf{r}_i}\right)^2\right]\\
&\quad + \sum_{i=1}^{N}\left[-\frac{{}^{2}}{2m}\left(\mu_m^2\nabla_{\mathbf{R}}^2 + 2\,\mu_m\nabla_{\mathbf{R}}\cdot\nabla_{\mathbf{r}_i} + \nabla_{\mathbf{r}_i}^2\right)\right]\\
&= -\frac{{}^{2}}{2}\left(\frac{1}{M+Nm}\,\nabla_{\mathbf{R}}^2 + \sum_{i=1}^{N}\frac{1}{\mu_i}\,\nabla_{\mathbf{r}_i}^2 + \underbrace{\frac{1}{M_{\mathrm{tot}}}\sum_{i,j>i}^{N}\nabla_{\mathbf{r}_i}\cdot\nabla_{\mathbf{r}_j}}_{\hat{\mathrm{H}}_{\mathrm{mp}}}\right) \qquad \text{(A.8)}
\end{aligned}$$

where, M_{tot} is the total mass of all nuclei, the first term identifies the kinetic energy of the center-of-mass and the second term denotes the kinetic energy of the individual independent particles, while the last term under the brace is the *mass polarization*. The mass polarization is a kinetic energy correction term that results from the coupling of correlated particle motion. For identical particles, equation (A.8) reduces to that given in [147].

Appendix B

Spherical Harmonic Projections

The presentations given here are taken from the original work [73]. The contents presented contains the details for calculating the projection coefficients of the expansion of the spherical harmonics. The auxiliary functions of the spherical harmonics are the same for both the original code reviewed in Chapter 3 and the extension of the code to incorporate the trap displacement in Chapter 4. For completeness the calculation details of these coefficients are reproduced in this appendix.

Any function of angular arguments can be presented as

$$F(\theta, \phi) = \sum_{l=0}^{\infty} \sum_{m=-l}^{l} {}_{lmt} Y_l^m(\theta, \phi)\,, \tag{B.1}$$

with the coefficients ${}_{lmt}$ defined as

$${}_{lmt} = (-1)^m A_{l-m} \int\limits_0^\pi d\theta \int\limits_0^{2\pi} d\phi \sin(\theta) F(\theta, \phi) P_l^{-m}(\cos(\theta)) e^{-\mathbf{i}m\phi}\,. \tag{B.2}$$

There are three ${}_{lmt}$ coefficients for each Cartesian coordinate (index c):

$$\begin{aligned}
{}^{x}_{lmt} &= (-1)^m A_{l-m} \int\limits_0^\pi d\theta \int\limits_0^{2\pi} d\phi \sin(\theta) \cos^{2t}(\phi) \sin^{2t}(\theta) \\
&\quad \times P_l^{-m}(\cos(\theta)) e^{-\mathbf{i}m\phi}\,, && \text{(B.3)} \\
{}^{y}_{lmt} &= (-1)^m A_{l-m} \int\limits_0^\pi d\theta \int\limits_0^{2\pi} d\phi \sin(\theta) \sin^{2t}(\phi) \sin^{2t}(\theta) \\
&\quad \times P_l^{-m}(\cos(\theta)) e^{-\mathbf{i}m\phi}\,, && \text{(B.4)} \\
{}^{z}_{lmt} &= (-1)^m A_{l-m} \int\limits_0^\pi d\theta \int\limits_0^{2\pi} d\phi \sin(\theta) \cos^{2t}(\theta) \\
&\quad \times P_l^{-m}(\cos(\theta)) e^{-\mathbf{i}m\phi}. && \text{(B.5)}
\end{aligned}$$

Using the Euler formula for $\cos^{2t}(\phi)$ together with the Binomial theorem, ${}^{x}_{lmt}$ is evaluated as follows

$$
\begin{aligned}
{}^{x}_{lmt} &= (-1)^m A_{l-m} \frac{1}{2^{2t}} \sum_{k=0}^{2t} \binom{2t}{k} \int_{0}^{\pi} d\,\theta \sin(\theta) \sin^{2t}(\theta) P_l^{-m}(\cos(\theta)) \\
&\quad \times \int_{0}^{2\pi} d\phi\, e^{\mathbf{i}(2k-2t-m)\phi} \\
&= (-1)^m A_{l-m} \quad \frac{\pi}{2^{2t-1}} \sum_{k=0}^{2t} \binom{2t}{k} \int_{-1}^{1} dx (1-x^2)^t P_l^{-m}(x) \delta_{2k-2t-m,\,0} \\
&= (-1)^m A_{l-m} \quad \frac{\pi}{2^{2t-1}} 2tt + \frac{m}{2} \int_{-1}^{1} dx (1-x^2)^t P_l^{-m}(x). \qquad \text{(B.6)}
\end{aligned}
$$

Since the index k is an integer and $0 \leq k \leq 2t$, then $-2t \leq m \leq 2t$ and m is always even. Since the integrand in the integral of (B.6) is symmetric around zero in $[-1,\, 1]$, then it is non-zero only if the integrand is a symmetric function. If it is antisymmetric then it is zero. The parity property of the associated Legendre function $P_l^m(x)$ is the following. It is even if $l+|m|$ is even and it is odd if $l+|m|$ odd. Once m is even, then the only possible case is when l is even. Physical restrictions on l are $l \geq 0$ and $|m| \leq l$. The functions $P_{l>2t}^{|m|\leq l, |m|\leq 2t}(x)$ are oscillatory and the contributions of the negative and the positive parts of the integrand within the interval $[-1,\, 1]$ are equal and the integral is zero. Therefore, another restriction on l is $l \leq 2t$. Such combination of l, m, t indices allow for the analytical calculation of integral (B.6). Using the formula [148]

$$
\int_{0}^{1} x^{\lambda} P_{2m}(x) dx = \frac{(-1)^m \Gamma[m - \frac{1}{2}\lambda] \Gamma[\frac{1}{2} + \frac{1}{2}\lambda]}{2\Gamma[-\frac{1}{2}\lambda] \Gamma[m + \frac{3}{2} + \frac{1}{2}\lambda]}, \text{ with } [Re\,\lambda > -1] \qquad \text{(B.7)}
$$

and from the relations between gamma functions and the factorials one obtains

$$\begin{aligned}
{}^{x}_{lmt} &= (-1)^m A_{l-m} \frac{\pi}{2^{2t-1}} \binom{2t}{t+\frac{m}{2}} \\
&\quad \times \frac{\pi 2^{-m} \Gamma[t+1-\frac{1}{2}m]\Gamma[t+1+\frac{1}{2}m]}{\Gamma[t+1+\frac{1}{2}l+\frac{1}{2}]\Gamma[t+1-\frac{1}{2}l]\Gamma[\frac{1}{2}m+\frac{1}{2}l+1]\Gamma[\frac{1}{2}m-\frac{1}{2}l+\frac{1}{2}]} \\
&= (-1)^{\frac{l+m}{2}} 2^{-\frac{m}{2}-t+2} A_{l-m}\, \pi \binom{2t}{t+\frac{m}{2}} \frac{(t-\frac{m}{2})!(t+\frac{m}{2})!(l-m-1)!!}{(t-\frac{l}{2})!(\frac{l}{2}+\frac{m}{2})!(2t+l+1)!!},
\end{aligned}$$

with (B.8)

$$\begin{aligned}
& l, m - \text{even integers}, \\
& -2t \leq m \leq 2t, \\
& |m| \leq l, \\
& l \leq 2t. \qquad \text{(B.9)}
\end{aligned}$$

Here, due to the limitations on the indices, there are no “problematic” Gamma functions. The last term in denominator is calculated with using the formula [148]

$$\Gamma\left[\frac{1}{2}-n\right] = (-1)^n \frac{2^n\sqrt{\pi}}{(2n-1)!!}, \quad n \geq 0 \in \text{Integers} \quad . \qquad \text{(B.10)}$$

For integral ${}^{y}_{lmt}$ derivation is the following

$$\begin{aligned}
{}^{y}_{lmt} &= (-1)^m A_{l-m} \frac{(-1)^t}{2^{2t}} \sum_{k=0}^{2t} \binom{2t}{k} (-1)^{2t-k} \int_0^{\pi} d\,\theta \sin(\theta) \sin^{2t}(\theta) \\
&\quad \times P_l^{-m}(\cos(\theta)) \int_0^{2\pi} d\phi\, e^{\mathbf{i}(2k-2t-m)\phi} \\
&= (-1)^m A_{l-m} \quad \frac{(-1)^t \pi}{2^{2t-1}} \sum_{k=0}^{2t} \binom{2t}{k} (-1)^{2t-k} \int_{-1}^{1} dx (1-x^2)^t \\
&\quad \times P_l^{-m}(x) \delta_{2k-2t-m,\,0} \\
&= (-1)^m A_{l-m} (-1)^{2t-\frac{m}{2}} \frac{\pi}{2^{2t-1}} \binom{2t}{t+\frac{m}{2}} \int_{-1}^{1} dx (1-x^2)^t P_l^{-m}(x) \\
&= (-1)^{\frac{m}{2}} \; {}^{x}_{lmt} \,. \qquad \text{(B.11)}
\end{aligned}$$

Using equation (B.7) for ${}^{z}_{lmt}$, one can derive

$$
\begin{aligned}
{}^{z}_{lmt} &= (-1)^m A_{l-m} \int\limits_{-1}^{1} dx\, x^{2t} P_l^{-m}(x) \int\limits_{0}^{2\pi} d\phi\; e^{-\mathbf{i}m\phi} \\
&= A_{l0}\, 4\pi\delta_{m,0} \int\limits_{0}^{1} dx\, x^{2t} P_l^{0}(x) \\
&= A_{l0} 2\pi\delta_{m,0} \frac{(-1)^{\frac{l}{2}}\Gamma[\frac{l}{2}-\frac{1}{2}2t]\Gamma[\frac{1}{2}+\frac{1}{2}2t]}{\Gamma[-\frac{1}{2}2t]\Gamma[\frac{l}{2}+\frac{3}{2}+\frac{1}{2}2t]} \\
&= A_{l0}\, 2\pi\delta_{m,0} \frac{(-1)^{\frac{l}{2}}\Gamma[\frac{l}{2}-t]\Gamma[\frac{1}{2}+t]}{\Gamma[-t]\Gamma[\frac{l}{2}+\frac{3}{2}+t]} \\
&= A_{l0}\, 2\pi(-1)^{\frac{l}{2}}\delta_{m,0} \frac{\Gamma[\frac{1}{2}+t]\prod_{i=0}^{l/2-1}(-t+i)}{\Gamma[\frac{l}{2}+\frac{3}{2}+t]} \\
&= A_{l0}\, (-1)^{\frac{l}{2}}\pi\delta_{m,0} \frac{2^{\frac{l}{2}+2}(2t-1)!!}{(l+2t+1)!!} \prod_{i=0}^{l/2-1}(-t+i)\,. \qquad \text{(B.12)}
\end{aligned}
$$

Here, the formula

$$
P_l^{-m} = (-1)^m \frac{(l-m)!}{(l+m)!} P_l^m \qquad \text{(B.13)}
$$

is applied to $\Gamma\left[-t+\dfrac{l}{2}\right]$ because $\dfrac{l}{2}$ is a natural number. l is even because x^{2t} is an even function and the Legendre polynomial must also be even. Due to the symmetry of the integrand, the limitation on l index is $l \leq 2t$. For the coupling terms (4.9), the expansion coefficients are the same for the terms $R_c^{2k} r_c^{2t}$ and different for $R_c^{2i+1} r_c^{2j+1}$. There are three new coefficients to be derived:

$$
\begin{aligned}
\tilde{}^{\,x}_{lmj} = (-1)^m A_{l-m} \int\limits_{0}^{\pi} d\theta \int\limits_{0}^{2\pi} d\phi \sin(\theta)\cos^{2j+1}(\phi)\sin^{2j+1}(\theta) \\
\times\; P_l^{-m}(\cos(\theta)) e^{-\mathbf{i}m\phi}\,, \qquad \text{(B.14)}
\end{aligned}
$$

$$
\begin{aligned}
\tilde{}^{\,y}_{lmj} = (-1)^m A_{l-m} \int\limits_{0}^{\pi} d\theta \int\limits_{0}^{2\pi} d\phi \sin(\theta)\sin^{2j+1}(\phi)\sin^{2j+1}(\theta) \\
\times\; P_l^{-m}(\cos(\theta)) e^{-\mathbf{i}m\phi}\,, \qquad \text{(B.15)}
\end{aligned}
$$

$$
\begin{aligned}
\tilde{}^{\,z}_{lmj} = (-1)^m A_{l-m} \int\limits_{0}^{\pi} d\theta \int\limits_{0}^{2\pi} d\phi \sin(\theta)\cos^{2j+1}(\theta) \\
\times\; P_l^{-m}(\cos(\theta)) e^{-\mathbf{i}m\phi}. \qquad \text{(B.16)}
\end{aligned}
$$

Applying Euler formula for $\cos^{2j+1}(\phi)$ and Binomial theorem, the coefficient $\tilde{}^{x}_{lmj}$ can be found after evaluation of the following integral

$$\begin{aligned}
\tilde{}^{x}_{lmj} &= (-1)^m A_{l-m} \frac{1}{2^{2j+1}} \sum_{k=0}^{2j+1} \binom{2j+1}{k} \int\limits_0^{\pi} d\theta \sin(\theta) \sin^{2j+1}(\theta) P_l^{-m}(\cos(\theta)) \\
&\quad \times \int\limits_0^{2\pi} d\phi \; e^{\mathbf{i}k\phi} e^{-\mathbf{i}(2j+1-k)\phi} e^{-\mathbf{i}m\phi} (-1)^m A_{l-m} \frac{1}{2^{2j+1}} \sum_{k=0}^{2j+1} \binom{2j+1}{k} \\
&\quad \times \int\limits_{-1}^{1} dx (1-x^2)^{j+\frac{1}{2}} P_l^{-m}(x) \times 2\pi \, \delta_{2k-2j-m-1,0} \\
&= (-1)^m A_{l-m} \frac{\pi}{2^{2j}} \binom{2j+1}{j+\frac{m+1}{2}} \int\limits_{-1}^{1} dx \, (1-x^2)^{j+\frac{1}{2}} P_l^{-m}(x) \, . \qquad \text{(B.17)}
\end{aligned}$$

- Since $0 \leq k \leq 2j+1$ is an integer, then m can only be an odd integer $-2j-1 \leq m \leq 2j+1$.
- Since $(1-x^2)^{j+1}$ is an even function in $[-1,1]$, then $l+|m|$ must be even therefore l is odd.
- Character of integrand is such that negative and positive contributions of constituent functions give zero overlap in the integration interval when $l > 2j+1$.

With these limitation of indices, the formula (B.7) can be applied leading to the equation

$$\begin{aligned}
\tilde{}^{x}_{lmj} &= (-1)^m A_{l-m} \frac{\pi}{2^{2j}} \binom{2j+1}{j+\frac{m+1}{2}} \\
&\quad \times \frac{\pi 2^m \Gamma[j+\frac{3}{2}+\frac{m}{2}]\Gamma[j+\frac{3}{2}-\frac{m}{2}]}{\Gamma[j+\frac{l}{2}+2]\Gamma[j+\frac{3}{2}-\frac{l}{2}]\Gamma[-\frac{m}{2}+\frac{l}{2}+1]\Gamma[-\frac{m}{2}-\frac{l}{2}+\frac{1}{2}]} \\
&= (-1)^m A_{l-m} (-1)^{\frac{l-m}{2}} \frac{\pi}{2^{2j}} \binom{2j+1}{j+\frac{m+1}{2}} \\
&\quad \times \frac{2^{\frac{2j+3-m}{2}} (\frac{2j+1-m}{2})!(\frac{2j+1+m}{2})!(l-m-1)!!}{(2j+l+2)!!(\frac{2j+1-l}{2})!(\frac{m+l}{2})!} \, . \qquad \text{(B.18)}
\end{aligned}$$

Again, due to limitations for indices there are no problematic gamma functions and factorials. For integral $\tilde{}^{y}_{lmj}$ derivations are similar giving to the following result

$$\tilde{}^{y}_{lmj} = \mathbf{i} \, (-1)^{\frac{m-3}{2}} \tilde{}^{x}_{lmj} \, , \qquad \text{(B.19)}$$

with the same limitations for indices for $\tilde{}^{\,x}_{lmj}$. Finally for the z component coefficient is

$$
\begin{aligned}
\tilde{}^{\,z}_{lmj} &= A_{l0} 2\pi \delta_{m,0} \int\limits_{-1}^{1} dx\, x^{2j+1} P_l^0(x) = A_{l0} 4\pi \delta_{m,0} \int\limits_{0}^{1} dx\, x^{2j+1} P_l^0(x) \\
&= A_{l0} 4\pi \delta_{m,0} (-1)^{\frac{l-1}{2}} \frac{\Gamma[-j + \frac{l-1}{2}]\Gamma[j + \frac{3}{2}]}{2\Gamma[-j]\Gamma[\frac{l}{2} + j + 2]} \\
&= A_{l0} 4\pi \delta_{m,0} (-2)^{\frac{l-1}{2}} \frac{(2j+1)!!}{(2j+l+2)!!} \prod_{i=0}^{\frac{l-3}{2}} (-j+i)\,. \qquad \text{(B.20)}
\end{aligned}
$$

Appendix C

Matrix elements

The contents presented in this appendix are taken from section 3 (a) in [73]. The extension of the original method to incorporate the spatial separation of the trap potential affects only the trapping potential component of the code. The other parts remain the same and they are given in this appendix for completeness purposes.

After the transformation to spherical coordinates, the matrices corresponding to the eigenvalue problems in equations (3.13), (3.14), and (3.17) are

$$h^{\text{rel.}}_{\mathbf{a},\mathbf{a}'} = \langle \varphi_{\mathbf{a}} | \hat{\mathrm{h}}_{\text{rel.}} | \varphi_{\mathbf{a}'} \rangle \,, \qquad s^{\text{rel.}}_{\mathbf{a},\mathbf{a}'} = \langle \varphi_{\mathbf{a}} | \varphi_{\mathbf{a}'} \rangle \,, \tag{C.1}$$

$$h^{\text{c.m.}}_{\mathbf{b},\mathbf{b}'} = \langle \psi_{\mathbf{b}} | \hat{\mathrm{h}}_{\text{c.m.}} | \psi_{\mathbf{b}'} \rangle \,, \qquad s^{\text{c.m.}}_{\mathbf{b},\mathbf{b}'} = \langle \psi_{\mathbf{b}} | \psi_{\mathbf{b}'} \rangle \tag{C.2}$$

and

$$H_{\kappa,\kappa'} = \langle \Phi_\kappa | \hat{\mathrm{H}} | \Phi_{\kappa'} \rangle. \tag{C.3}$$

The overlap matrix elements between configurations is

$$\begin{aligned} S_{\kappa,\kappa'} &= \langle \Phi_\kappa | \Phi_{\kappa'} \rangle \\ &= \langle \varphi_{i_\kappa} \psi_{j_\kappa} | \varphi_{i_{\kappa'}} \psi_{j_{\kappa'}} \rangle = \delta_{i_\kappa, i_{\kappa'}} \, \delta_{j_\kappa, j_{\kappa'}} = \delta_{\kappa,\kappa'} \,. \end{aligned} \tag{C.4}$$

For compactness reasons, the integrals over B splines and their derivatives are denoted as

$${}^{\lambda}_{\partial^\mu \alpha \, \partial^\nu \alpha'} = \int\limits_0^\infty dr \, r^\lambda \frac{\partial^\mu B_\alpha(r)}{\partial r^\mu} \frac{\partial^\nu B_{\alpha'}(r)}{\partial r^\nu} \tag{C.5}$$

and

$${}^{\lambda}_{\partial^\mu \beta \, \partial^\nu \beta'} = \int\limits_0^\infty dR \, R^\lambda \frac{\partial^\mu B_\beta(R)}{\partial R^\mu} \frac{\partial^\nu B_{\beta'}(R)}{\partial R^\nu} \tag{C.6}$$

for c.m. and rel. motion, respectively. The integrals that occur in the Hamiltonian are described in the following.

C.1 Overlap

The overlap matrices between the basis functions of the center-of-mass and relative motions are not identity because of the nonorthogonality of B Splines. They are given by

$$s^{\text{rel.}}_{\mathbf{a},\mathbf{a}'} = {}_{\alpha\alpha'} \int_\Omega d\Omega \, Y_l^{m*}(\theta,\phi) Y_{l'}^{m'}(\theta,\phi) = {}_{\alpha\alpha'} \delta_{ll'} \delta_{mm'} \tag{C.7}$$

and, similarly,

$$s^{\text{c.m.}}_{\mathbf{b},\mathbf{b}'} = {}_{\beta\beta'} \delta_{LL'} \delta_{MM'} \,. \tag{C.8}$$

C.2 Kinetic energy

Using the solutions of the angular momentum squared operators of the spherical harmonics, $\hat{\mathbf{l}}^2_{\text{rel.}} Y_l^m(\theta,\phi) = l(l+1) Y_l^m(\theta,\phi)$ and $\hat{\mathbf{l}}^2_{\text{c.m.}} Y_L^M(\Theta,\Phi) = L(L+1) Y_L^M(\Theta,\Phi)$, the kinetic-energy operators for the relative motions is

$$\begin{aligned} t^{\text{rel.}}_{\mathbf{a},\mathbf{a}'} &= -\frac{1}{2\mu} \; {}_{\partial^2 \alpha\, \alpha'} \, \delta_{ll'} \delta_{mm'} + \frac{1}{2\mu} l(l+1) \; {}^{-2}_{\alpha\alpha'} \, \delta_{ll'} \delta_{mm'} \\ &= \frac{1}{2\mu} \left(\; {}_{\partial^1 \alpha\, \partial^1 \alpha'} + l(l+1) \; {}^{-2}_{\alpha\alpha'} \right) \delta_{ll'} \delta_{mm'} \end{aligned} \tag{C.9}$$

and analogously

$$t^{\text{c.m.}}_{\mathbf{b},\mathbf{b}'} = \frac{1}{2\text{M}} \left(\; {}_{\partial^1 \beta\, \partial^1 \beta'} + L(L+1) \; {}^{-2}_{\beta\beta'} \right) \delta_{LL'} \delta_{MM'} \tag{C.10}$$

for the center-of-mass motion.

C.3 Interparticle interaction

The matrix elements of the interparticle interaction potential are

$$u_{\mathbf{a},\mathbf{a}'} = \delta_{ll'} \delta_{mm'} \int\limits_0^\infty dr \;\, u(r) B_\alpha(r) \, B_{\alpha'}(r) \,. \tag{C.11}$$

C.4 Trap potential

Using the identity $Y_{l_t}^{m_t *}(\theta,\phi) = (-1)^{m_t}\, Y_{l_t}^{-m_t}(\theta,\phi)$, the product of two spherical harmonics can be expressed as a sum of products between a spherical harmonic and the 3j-Wigner symbols,

$$Y_l^m(\theta,\phi)\, Y_{l_t}^{m_t}(\theta,\phi) = \sum_{l_t,m_t} {}^{0}_{l_t\, l\, l_t} \begin{pmatrix} l_t & l & l_t \\ m_t & m & m_t \end{pmatrix} \begin{pmatrix} l_t & l & l_t \\ 0 & 0 & 0 \end{pmatrix} Y_{l_t}^{m_t *}(\theta,\phi) \quad \text{(C.12)}$$

where the coefficient ${}^{a}_{b\,c\,d}$ is defined in equation (4.41).

The Gaunt coefficient is then obtained as [149, 150]

$$\begin{aligned} \int_\Omega d\Omega\, Y_l^m(\theta,\phi) Y_{l_t}^{m_t}(\theta,\phi) Y_{l'}^{m'^*}(\theta,\phi) &= \sum_{l_t,m_t} {}^{m_t}_{l_t\, l\, l_t} \begin{pmatrix} l_t & l & l_t \\ m_t & m & m_t \end{pmatrix} \begin{pmatrix} l_t & l & l_t \\ 0 & 0 & 0 \end{pmatrix} \\ &\quad \times \underbrace{\int_\Omega d\Omega\, Y_{l_t}^{-m_t}(\theta,\phi) Y_{l'}^{m'^*}(\theta,\phi)}_{\delta_{l_t l'}\, \delta_{-m_t m'}} \\ &= {}^{m'}_{l_t\, l\, l'} \begin{pmatrix} l_t & l & l' \\ m_t & m & -m' \end{pmatrix} \begin{pmatrix} l_t & l & l' \\ 0 & 0 & 0 \end{pmatrix}. \quad \text{(C.13)} \end{aligned}$$

Using equation (C.13), the angular parts for the matrix elements of the c.m. and rel. motion trapping potential equations (3.6) and (3.7) can be calculated according to

$$\begin{aligned} V_{\mathbf{b},\mathbf{b}'}^{\text{c.m.}} &= -\frac{1}{2} \sum_{s=1}^{2} \sum_{c=x,y,z} V_c^s \sum_{k=1}^{n} {}^{\cos}_{0kcs} \; {}^{2k}_{\beta\,\beta'} \sum_{L_k=0,\{2\}}^{2k} \; \sum_{M_k=-L_k,\{2\}}^{L_k} \\ &\quad \times {}^{c}_{L_k M_k k} \; {}^{M'}_{L_k\, L\, L'} \begin{pmatrix} L_k & L & L' \\ M_k & M & -M' \end{pmatrix} \begin{pmatrix} L_k & L & L' \\ 0 & 0 & 0 \end{pmatrix} \end{aligned} \quad \text{(C.14)}$$

and

$$\begin{aligned} v_{\mathbf{a},\mathbf{a}'}^{\text{rel.}} &= -\frac{1}{2} \sum_{s=1}^{2} \sum_{c=x,y,z} V_c^s \sum_{t=1}^{n} {}^{\cos}_{t0cs} \; {}^{2t}_{\alpha\,\alpha'} \sum_{l_t=0,\{2\}}^{2t} \; \sum_{m_t=-l_t,\{2\}}^{l_t} \\ &\quad \times {}^{c}_{l_t m_t t} \; {}^{m'}_{l_t\, l\, l'} \begin{pmatrix} l_t & l & l' \\ m_t & m & -m' \end{pmatrix} \begin{pmatrix} l_t & l & l' \\ 0 & 0 & 0 \end{pmatrix} \end{aligned} \quad \text{(C.15)}$$

for the c.m. and rel. matrix elements, respectively. The relative overlap and Hamiltonian matrices in equation (C.1) can then be obtained using equations (C.7), (C.9), (C.11), and (C.15). Using these matrices in the eigenvalue equation (3.14) yields the uncoupled eigenenergies and eigenfunctions of the rel. motion after diagonalization. Similarly, equations (C.8), (C.10), and (C.14) provide the overlap and Hamiltonian matrices in equation (3.13), thus the eigenenergies and eigenfunctions of the uncoupled c.m. motion can be found.

C.5 Matrix elements of the coupled Hamiltonian

The total Hamiltonian is given by the sum of the uncoupled Hamiltonians of rel. and c.m. motion, and the coupling term $\hat{\mathrm{W}}$ (3.10). The contributions of the separated parts is given by

$$\begin{aligned} \langle \Phi_\kappa | \hat{\mathrm{h}}_{\mathrm{c.m.}} + \hat{\mathrm{h}}_{\mathrm{rel.}} | \Phi_{\kappa'} \rangle &= \langle \varphi_{i_\kappa} \psi_{j_\kappa} | \hat{\mathrm{h}}_{\mathrm{c.m.}} + \hat{\mathrm{h}}_{\mathrm{rel.}} | \varphi_{i_{\kappa'}} \psi_{j_{\kappa'}} \rangle \\ &= (\epsilon^{\mathrm{rel.}}_{i_\kappa} + \epsilon^{\mathrm{c.m.}}_{j_\kappa}) \, \delta_{i_\kappa, i_{\kappa'}} \, \delta_{j_\kappa, j_{\kappa'}} \, . \end{aligned} \tag{C.16}$$

The Hamiltonian matrix elements $H_{\kappa,\kappa'}$ in equation (C.3) is obtained after determining the coupling matrix $\hat{\mathrm{W}}$

$$\begin{aligned}
W_{\kappa,\kappa'} \;=\;& \frac{1}{2}\sum_{s=1}^{2}\sum_{c=x,y,z} V_c^s \Bigg\{ (-1)^{\eta_s} \sum_{j=0}^{n-1} (-1)^j \frac{(2k_c\mu_{\eta_s})^{2j+1}}{(2j+1)!} \sum_{\alpha=2}^{N_r-1}\sum_{l=0}^{N_l}\sum_{m=-l}^{l} \tilde{c}^{\text{rel.}}_{p_\kappa,\mathbf{a}} \\
& \times \sum_{\alpha'=2}^{N_r-1}\sum_{l'=0}^{N_l}\sum_{m'=-l}^{l} \tilde{c}^{\text{rel.}}_{p_{\kappa'},\mathbf{a}'} \;\; {}^{2j+1}_{\alpha\,\alpha'} \sum_{l_j=1,\{2\}}^{2j+1} \Bigg\{ \Bigg[\tilde{\ }^{c}_{l_j0j} \begin{pmatrix} l_j & l & l' \\ 0 & m & m' \end{pmatrix} \\
& \qquad\qquad + \sum_{m_j=-l_j,\{2\}}^{l_j} \tilde{\ }^{c}_{l_jm_jj} \begin{pmatrix} l_j & l & l' \\ m_j & m & -m' \end{pmatrix} \Bigg] \;\; {}^{m'}_{l_jll'} \begin{pmatrix} l_j & l & l' \\ 0 & 0 & 0 \end{pmatrix} \Bigg\} \\
& \times \sum_{i=0}^{n-1-j} (-1)^i \frac{(2k_c)^{2i+1}}{(2i+1)!} \sum_{\beta=2}^{N_R-1}\sum_{L=0}^{N_L}\sum_{M=-L}^{L} \tilde{c}^{\text{c.m.}}_{q_\kappa,\mathbf{b}} \sum_{\beta'=2}^{N_R-1}\sum_{L'=0}^{N_L}\sum_{M'=-L'}^{L'} \tilde{c}^{\text{c.m.}}_{q_{\kappa'},\mathbf{b}'} \\
& \times \;{}^{2i+1}_{\beta\,\beta'} \sum_{L_i=1,\{2\}}^{2i+1} \Bigg\{ \Bigg[\tilde{\ }^{c}_{L_i0i} \begin{pmatrix} L_i & L & L' \\ 0 & M & M' \end{pmatrix} \\
& \qquad + \sum_{M_i=-L_i,\{2\}}^{L_i} \tilde{\ }^{c}_{L_iM_ii} \begin{pmatrix} L_i & L & L' \\ M_i & M & -M' \end{pmatrix} \Bigg] \;\; {}^{M'}_{L_iLL'} \begin{pmatrix} L_i & L & L' \\ 0 & 0 & 0 \end{pmatrix} \Bigg\} \\
& - \sum_{t=1}^{n} (-1)^t \frac{(2k_c\mu_{\eta_s})^{2t}}{(2t)!} \sum_{\alpha=2}^{N_r-1}\sum_{l=0}^{N_l}\sum_{m=-l}^{l} \tilde{c}^{\text{rel.}}_{p_\kappa,\mathbf{a}} \sum_{\alpha'=2}^{N_r-1}\sum_{l'=0}^{N_l}\sum_{m'=-l}^{l} \tilde{c}^{\text{rel.}}_{p_{\kappa'},\mathbf{a}'} \;\; {}^{2t}_{\alpha\,\alpha'} \\
& \times \sum_{l_t=0,\{2\}}^{2t} \sum_{m_t=-l_t,\{2\}}^{l_t} \;\; {}^{c}_{l_tm_tt} \;\; {}^{m'}_{l_tll'} \begin{pmatrix} l_t & l & l' \\ m_t & m & -m' \end{pmatrix} \begin{pmatrix} l_t & l & l' \\ 0 & 0 & 0 \end{pmatrix} \\
& \times \sum_{k=1}^{n-t} (-1)^k \frac{(2k_c)^{2k}}{(2k)!} \sum_{\beta=2}^{N_R-1}\sum_{L=0}^{N_L}\sum_{M=-L}^{L} \tilde{c}^{\text{c.m.}}_{q_\kappa,\mathbf{b}} \sum_{\beta'=2}^{N_R-1}\sum_{L'=0}^{N_L}\sum_{M'=-L'}^{L'} \tilde{c}^{\text{c.m.}}_{q_{\kappa'},\mathbf{b}'} \;\; {}^{2k}_{\beta\,\beta'} \\
& \times \sum_{L_k=0,\{2\}}^{2k} \sum_{M_k=-L_k,\{2\}}^{L_k} \;\; {}^{c}_{L_kM_kk} \;\; {}^{M'}_{L_kLL'} \begin{pmatrix} L_k & L & L' \\ M_k & M & -M' \end{pmatrix} \begin{pmatrix} L_k & L & L' \\ 0 & 0 & 0 \end{pmatrix} \Bigg\} .
\end{aligned} \tag{C.17}$$

Appendix D

Code Description

This appendix contains the details of the input files for the orbital and configuration interaction codes described in section 3.3. Examples of how to control the programs are presented in the following sections. More instructions can be obtained from the script files that run the programs and the input files in the corresponding code directories.

D.1 Orbital calculations

This part of the program is located in ∼`/TwoAtInOL/d2h/orbit` and can be launched from the console using for example the following command line

```
otagsd2h.csh Li7Li7_b_x20000_y20000_z20000_110rm8g1l0m0_110CM8g1L0M0 no_interaction
Li7a164_Li7a164_k1_1000_1000_1000_k2_1000_1000_1000_i1_1000_1000_1000_i2_1000_1000_1000_222_222
D V m64 X clea
```

D.1.1 Basis file

`TwoAtInOL/d2h/orbit/basis/`
`Li7Li7_b_x20000_y20000_z20000_110rm8g1l0m0_110CM8g1L0M0.dba`

```
*******************************************************************
*
 START
*-----
*
 BASIS SPECIFICATION:
*--------------------
*
 Maximum value of x                        : 20000   !Box in x (in a.u)
 Maximum value of y                        : 20000   !Box in y (in a.u)
 Maximum value of z                        : 20000   !Box in z (in a.u)
 Order of the B-spline for r               : 8
 Number of B-splines for r                 : 110
 Type of knot vector for r                 : 1       !1 linear
 Parameter for the grid specification      : 15.50
 Maximum value of the angular momentum l : 0
*
 Order of the B-spline for R               : 8
 Number of B-splines for R                 : 110
 Type of knot vector for R                 : 1       !1 linear
 Parameter for the grid specification      : 15.50
 Maximum value of the angular momentum L : 0
*
 Maximum value of the angular momentum m : 0  !r.m. angular momentum
 Maximum value of the angular momentum M : 0  !c.m. angular momentum
*
 PARAMETERS OF THE ATOMS:
*-----------------------
 Statistics                                : 2           !Bosons
 Name of the first element                 : Li7
 Name of the second element                : Li7
 Mass of the first particle                : 7.01600455  !In Daltons
 Mass of the second particle               : 7.01600455  !In Daltons
*
 PARAMETERS OF THE MOLECULAR POTENTIAL:
*-------------------------------------
 Range of rotational quantum numbers J (begin, end)    : 0  0
 Electronic angular and spin momenta (projected on z) : 0  0
*
 END
*******************************************************************
```

D.1.2 Generic trap potential input file

The Taylor expansion coefficient file have the following structure.

```
Name of atom 1
Name of atom 2
Polarizability of atom 1
Polarizability of atom 2
Total number of coefficients
Order of the Taylor expansion trap 1 in the x direction
Order of the Taylor expansion trap 1 in the y direction
Order of the Taylor expansion trap 1 in the z direction
Order of the Taylor expansion trap 2 in the x direction
Order of the Taylor expansion trap 2 in the y direction
Order of the Taylor expansion trap 2 in the z direction
Coefficient of order 0 in X (c.m.)
Coefficient of order 1 in X (c.m.)
Coefficient of order 2 in X (c.m.)
Coefficient of order 3 in X (c.m.)
   ⋮
Coefficient of order 0 in x (rel.)
Coefficient of order 1 in x (rel.)
Coefficient of order 2 in x (rel.)
Coefficient of order 3 in x (rel.)
   ⋮
Coefficient of order 0 in Y (c.m.)
Coefficient of order 1 in Y (c.m.)
Coefficient of order 2 in Y (c.m.)
Coefficient of order 3 in Y (c.m.)
   ⋮
Coefficient of order 0 in y (rel.)
Coefficient of order 1 in y (rel.)
Coefficient of order 2 in y (rel.)
Coefficient of order 3 in y (rel.)
   ⋮
Coefficient of order 0 in Z (c.m.)
Coefficient of order 1 in Z (c.m.)
Coefficient of order 2 in Z (c.m.)
Coefficient of order 3 in Z (c.m.)
   ⋮
Coefficient of order 0 in z (rel.)
Coefficient of order 1 in z (rel.)
Coefficient of order 2 in z (rel.)
Coefficient of order 3 in z (rel.)
   ⋮
```

The following is an example of coefficient file for harmonic trap with $\lambda = I = 1000$ in x, y, and z directions. The wavelength is in units of nanometer (nm) while the units of intensity is W cm^{-2}. The Taylor expansion coefficients are given by the set of equations (3.9).

```
TwoAtInOL/d2h/orbit/trap/
Li7a164_Li7a164_k1_1000_1000_1000_k2_1000_1000_1000_i1_1000_1000_1000_i2_1000_1000_1000_222_222.coeff
```

```
Li7     ! Name of the first element
Li7     ! Name of the second element
164     ! Polarizability of first element
164     ! Polarizability of second element
18      ! Total number of coefficients
2       ! Maximum order Taylor expansion trap 1 in the x direction
2       ! Maximum order Taylor expansion trap 1 in the y direction
2       ! Maximum order Taylor expansion trap 1 in the z direction
2       ! Maximum order Taylor expansion trap 2 in the x direction
2       ! Maximum order Taylor expansion trap 2 in the y direction
2       ! Maximum order Taylor expansion trap 2 in the z direction
5.63368020268997689705643226709439533949238702423 55e-18
0
0
1.40842005067249422426410806677359883487309675605 89e-18
0
0
5.63368020268997689705643226709439533949238702423 55e-18
0
0
1.40842005067249422426410806677359883487309675605 89e-18
0
0
5.63368020268997689705643226709439533949238702423 55e-18
0
0
1.40842005067249422426410806677359883487309675605 89e-18
```

These coefficients are calculated using a Mathematica script located in `TwoAtInOL/d2h/input_files/mathematica_coeff_script`

D.1.3 Orbital sample calculation

The output from the orbital calculations using the basis and the generic trap potential in sections D.1.1 and D.1.2, respectively, corresponding to the command line given at the beginning of the section D.1 is shown below.

```
 REL VECTOR LENGTH:          108
 COM VECTOR LENGTH:          108
      diagonalization took:                       0 s.
 rm:Ag
           1   1.50000000000000       3.148200444094844E-011
           2   3.50000000000037       7.345801036222093E-011
           3   5.50000000000845       1.154340162836552E-010
           4   7.50000000008834       1.574100222065966E-010
           5   9.50000000060652       1.993860281387368E-010
           6   11.5000000031319       2.413620341130038E-010
           7   13.5000000131166       2.833380402438285E-010
           8   15.5000000468122       3.253140468722967E-010
           9   17.5000001473125       3.672900549028619E-010
          10   19.5000004188899       4.092660665239930E-010

      diagonalization took:                       0 s.
 CM:Ag
           1   1.50000000000000       3.148200444094854E-011
           2   3.50000000000044       7.345801036222244E-011
           3   5.50000000000855       1.154340162836573E-010
           4   7.50000000008829       1.574100222065955E-010
           5   9.50000000060642       1.993860281387347E-010
           6   11.5000000031318       2.413620341130025E-010
           7   13.5000000131167       2.833380402438302E-010
           8   15.5000000468124       3.253140468722990E-010
           9   17.5000001473127       3.672900549028644E-010
          10   19.5000004188899       4.092660665239939E-010
```

The eigenvalues in the first columns have been scaled using the harmonic oscillator trap frequency ω_{rel} for rel. motion and $\omega_{\text{c.m.}}$ for c.m. values while the second column are the unscaled energies in Hartree for this example of $l = m = 0$ only the A_g symmetry results are present. The analytical values for an isotropic 3D harmonic oscillator is $\left(n + \frac{3}{2}\right)\ \omega$ where $n = 0, 1, 2, \cdots$ as shown below (the c.m. and rel. motion eigenvalue are the same).

```
           1   1.50000000000000   3.148200444094851E-011
           2   3.50000000000000   7.345801036221318E-011
           3   5.50000000000000   1.154340162834779E-010
           4   7.50000000000000   1.574100222047425E-010
           5   9.50000000000000   1.993860281260072E-010
           6   11.5000000000000   2.413620340472719E-010
           7   13.5000000000000   2.833380399685366E-010
           8   15.5000000000000   3.253140458898012E-010
           9   17.5000000000000   3.672900518110659E-010
          10   19.5000000000000   4.092660577323306E-010
```

D.2 Configuration-interaction calculations

Program is located in ∼`/TwoAtInOL/d2h/config` and can be launched with the command

```
citaold2hm.csh Li7Li7_b_x20000_y20000_z20000_110rm8g1l0m0_110CM8g1L0M0
no_interaction Li7a164_Li7a164_kx1000_ky1000_kz1000_ix1000_iy1000_iz1000
sin sin sin 2 2 2 Ag_vs_Li7Li7_1-10_1_10 D V m64 X clea
```

D.2.1 Configuration input file

`TwoAtInOL/d2h/config/input/Ag_vs_Li7Li7_1-10_1_10.dci`

```
*****************************************************
*
 ACTIVE ORBITALS:
*-----------------
*
 RELATIVE COORDINATE:
*--------------------
 ag:   [1->10] ! include Ag r.m. eigenstates 1 to 10
 b1g:  [0]
 b2g:  [0]
 b3g:  [0]
 au:   [0]
 b1u:  [0]
 b2u:  [0]
 b3u:  [0]
*
 CENTER-OF-MASS COORDINATE:
*--------------------------
 Ag:   [1->10] ! include Ag c.m. eigenstates 1 to 10
 B1g:  [0]
 B2g:  [0]
 B3g:  [0]
 Au:   [0]
 B1u:  [0]
 B2u:  [0]
 B3u:  [0]
*
 END
*****************************************************
```

D.2.2 CI sample calculation

The CI results from the configuration input file given above for the orbital calculations in section D.1.3 is given below.

```
CI VECTOR LENGTH:          100
NUMBER OF rm ACTIVE ORBITALS:          10
NUMBER OF CM ACTIVE ORBITALS:          10
     diagonalization took:                        0 s.

           1   3.00000000000000      6.296400888189698E-011
           2   5.00000000000037      1.049400148031695E-010
           3   5.00000000000044      1.049400148031709E-010
           4   7.00000000000081      1.469160207244434E-010
           5   7.00000000000845      1.469160207246038E-010
           6   7.00000000000855      1.469160207246057E-010
           7   9.00000000000889      1.888920266458776E-010
           8   9.00000000000892      1.888920266458782E-010
           9   9.00000000008829      1.888920266475440E-010
          10   9.00000000008834      1.888920266475451E-010
          11   11.0000000000170      2.308680325673125E-010
          12   11.0000000000887      2.308680325688165E-010
          13   11.0000000000888      2.308680325688190E-010
          14   11.0000000006064      2.308680325796831E-010
          15   11.0000000006065      2.308680325796853E-010
          16   13.0000000000967      2.728440384902507E-010
          17   13.0000000000969      2.728440384902538E-010
          18   13.0000000006068      2.728440385009556E-010
          19   13.0000000006070      2.728440385009592E-010
          20   13.0000000031318      2.728440385539510E-010
```

The analytical eigenvalues for the full Hamiltonian is the total of the c.m. and rel. motion eigenvalues since there is no coupling. They are given below where the first column has been scaled by the rel. motion trap frequency.

```
           1   3.00000000000000      6.296400888189701E-11
           2   5.00000000000000      1.049400148031617E-10
           3   5.00000000000000      1.049400148031617E-10
           4   7.00000000000000      1.469160207244264E-10
           5   7.00000000000000      1.469160207244264E-10
           6   7.00000000000000      1.469160207244264E-10
           7   9.00000000000000      1.888920266456910E-10
           8   9.00000000000000      1.888920266456910E-10
           9   9.00000000000000      1.888920266456910E-10
          10   9.00000000000000      1.888920266456910E-10
          11   11.0000000000000      2.308680325669557E-10
          12   11.0000000000000      2.308680325669557E-10
          13   11.0000000000000      2.308680325669557E-10
          14   11.0000000000000      2.308680325669557E-10
          15   11.0000000000000      2.308680325669557E-10
          16   13.0000000000000      2.728440384882204E-10
          17   13.0000000000000      2.728440384882204E-10
          18   13.0000000000000      2.728440384882204E-10
          19   13.0000000000000      2.728440384882204E-10
          20   13.0000000000000      2.728440384882204E-10
```

D.3 C_{2v} Program

The run procedure for both the orbital and the CI calculation for the new programs `otagsc2vm` and `citagsc2vm` are similar like the one for D_{2h} symmetry adapted codes described in the previous section. The two programs correspondingly solves the orbital and configuration-interaction parts of the problem. The basis file structure for this new code is exactly the same as that described in section D.1.1. The trap potential form is also similar to the generic version in section D.1.2 but includes the trap separation component as shown below.

```
Name of atom 1
Name of atom 2
Polarizability of atom 1
Polarizability of atom 2
Total number of coefficients
Order of the Taylor expansion trap 1 in the x direction
Order of the Taylor expansion trap 1 in the y direction
Order of the Taylor expansion trap 1 in the z direction
Order of the Taylor expansion trap 2 in the x direction
Order of the Taylor expansion trap 2 in the y direction
Order of the Taylor expansion trap 2 in the z direction
Trap separation in z direction
Coefficient of order 0 in X (c.m.)
Coefficient of order 1 in X (c.m.)
Coefficient of order 2 in X (c.m.)
Coefficient of order 3 in X (c.m.)
  ⋮
Coefficient of order 0 in x (rel.)
Coefficient of order 1 in x (rel.)
Coefficient of order 2 in x (rel.)
Coefficient of order 3 in x (rel.)
  ⋮
Coefficient of order 0 in Y (c.m.)
Coefficient of order 1 in Y (c.m.)
Coefficient of order 2 in Y (c.m.)
Coefficient of order 3 in Y (c.m.)
  ⋮
Coefficient of order 0 in y (rel.)
Coefficient of order 1 in y (rel.)
Coefficient of order 2 in y (rel.)
Coefficient of order 3 in y (rel.)
  ⋮
Coefficient of order 0 in Z (c.m.)
Coefficient of order 1 in Z (c.m.)
Coefficient of order 2 in Z (c.m.)
Coefficient of order 3 in Z (c.m.)
  ⋮
Coefficient of order 0 in z (rel.)
Coefficient of order 1 in z (rel.)
Coefficient of order 2 in z (rel.)
Coefficient of order 3 in z (rel.)
  ⋮
```

These coefficients are calculated using Mathematica script located in `TwoAtInOL/c2v/input_files/mathematica_coeff_script` for the $\mathrm{C}_{2\mathrm{v}}$ code. The following commands

```
TwoAtInOL/c2v/orbit> otagsc2vm.csh Li7Li7_b_x20000_y20000_z20000_110rm8g1l0m0_110CM8g1L0M0 no_interaction
Li7a164_Li7a164_k1_1000_1000_1000_k2_1000_1000_1000_i1_1000_1000_1000_i2_1000_1000_1000_222_222_d4000
D V m64 X clea
```

```
TwoAtInOL/c2v/config> citagsc2vm.csh Li7Li7_b_x20000_y20000_z20000_110rm8g1l0m0_110CM8g1L0M0 no_interaction
Li7a164_Li7a164_k1_1000_1000_1000_k2_1000_1000_1000_i1_1000_1000_1000_i2_1000_1000_1000_222_222_d4000
Ag_vs_Li7Li7_1-10_1_10 D V m64 X clea
```

can be used as an example, for performing the orbital and CI calculations, respectively. Sample input file for the generic trap potential for two harmonic traps separated by a distance of $4000\,a_0$ along the z direction takes the following structure.

```
Li7      ! Name of the first element
Li7      ! Name of the second element
164      ! Polarizability of first element
164      ! Polarizability of second element
18       ! Total number of coefficients
2        ! Maximum order Taylor expansion trap 1 in the x direction
2        ! Maximum order Taylor expansion trap 1 in the y direction
2        ! Maximum order Taylor expansion trap 1 in the z direction
2        ! Maximum order Taylor expansion trap 2 in the x direction
2        ! Maximum order Taylor expansion trap 2 in the y direction
2        ! Maximum order Taylor expansion trap 2 in the z direction
4000     ! Trap separation in z direction
2.2534720810759907588225729068377581357969548096942e-11
0
5.6336802026899768970564322670943953394923870242355e-18
0
0
1.4084200506724942242641080667735988348730967560589e-18
2.2534720810759907588225729068377581357969548096942e-11
0
5.6336802026899768970564322670943953394923870242355e-18
0
0
1.4084200506724942242641080667735988348730967560589e-18
2.2534720810759907588225729068377581357969548096942e-11
0
5.6336802026899768970564322670943953394923870242355e-18
-1.1267360405379953794112864534188790678984774048471e-14
0
1.4084200506724942242641080667735988348730967560589e-18
```

Appendix E

Basis Sets

Relative motion basis set	
B splines	
Number	240
Order	8
Knot sequence	30.50 (linear+geometric)
Spherical harmonics	
$l_{\max}$	60
$m_{\max}$	0
Center-of-mass motion basis set	
B splines	
Number	160
Order	8
Knot sequence	linear
Spherical harmonics	
L_{MAX}	60
M_{MAX}	0
Box size and atomic specification	
Box size [a.u.]	$\sqrt{12} \cdot 40000$
Mass of ^{7}Li in Dalton	7.01600455
Polarizability [a.u.]	164

Table E.1: Basis set No. E.1.

Relative motion basis set	
B splines	
Number	240
Order	8
Knot sequence	30.50 (linear+geometric)
Spherical harmonics	
l_{max}	60
m_{max}	0
Center-of-mass motion basis set	
B splines	
Number	240
Order	8
Knot sequence	linear
Spherical harmonics	
L_{MAX}	60
M_{MAX}	0
Box size and atomic specification	
Box size [a.u.]	$\sqrt{12} \cdot 40000$
Mass of ^{7}Li in Dalton	7.01600455
Polarizability [a.u.]	164
Configuration interaction	
Relative motion active orbitals	
Number of bound states	1
Total number of states	20
Symmetry	a_1
Center-of-mass active orbitals	
A_1 symmetry	20

Table E.2: Basis set No. E.2.

Relative motion basis set	
B splines	
Number	200
Order	8
Knot sequence	30.50 (linear+geometric)
Spherical harmonics	
l_{max}	0
m_{max}	0
Center-of-mass motion basis set	
B splines	
Number	200
Order	8
Knot sequence	linear
Spherical harmonics	
L_{MAX}	0
M_{MAX}	0
Box size and atomic specification	
Box size [a.u.]	$\sqrt{12} \cdot 20000$
Mass of ^{7}Li in Dalton	7.01600455
Polarizability [a.u.]	164

Table E.3: Basis set No. E.3.

Relative motion basis set	
B splines	
Number	240
Order	8
Knot sequence	30.50 (linear+geometric)
Spherical harmonics	
$l_{\max}$	50
$m_{\max}$	0
Center-of-mass motion basis set	
B splines	
Number	160
Order	8
Knot sequence	linear
Spherical harmonics	
L_{MAX}	50
M_{MAX}	0
Box size and atomic specification	
Box size [a.u.]	$\sqrt{12} \cdot 40000$
Mass of ^{7}Li in Dalton	7.01600455
Polarizability [a.u.]	164

Table E.4: Basis set No. E.4.

Relative motion basis set	
B splines	
Number	240
Order	8
Knot sequence	30.50 (linear+geometric)
Spherical harmonics	
l_{max}	60
m_{max}	0
Center-of-mass motion basis set	
B splines	
Number	160
Order	8
Knot sequence	linear
Spherical harmonics	
L_{MAX}	60
M_{MAX}	0
Box size and atomic specification	
Box size [a.u.]	$\sqrt{12} \cdot 40000$
Mass of ^{7}Li in Dalton	7.01600455
Polarizability [a.u.]	164

Table E.5: Basis set No. E.5.

Relative motion basis set	
B splines	
Number	240
Order	8
Knot sequence	30.50 (linear+geometric)
Spherical harmonics	
$l_{\max}$	80
$m_{\max}$	0
Center-of-mass motion basis set	
B splines	
Number	180
Order	8
Knot sequence	linear
Spherical harmonics	
L_{MAX}	80
M_{MAX}	0
Box size and atomic specification	
Box size [a.u.]	$\sqrt{12} \cdot 40000$
Mass of ^{7}Li in Dalton	7.01600455
Polarizability [a.u.]	164

Table E.6: Basis set No. E.6.

Relative motion basis set	
B splines	
Number	240
Order	8
Knot sequence	30.50 (linear+geometric)
Spherical harmonics	
$l_{\max}$	100
$m_{\max}$	0
Center-of-mass motion basis set	
B splines	
Number	180
Order	8
Knot sequence	linear
Spherical harmonics	
L_{MAX}	100
M_{MAX}	0
Box size and atomic specification	
Box size [a.u.]	$\sqrt{12} \cdot 40000$
Mass of ^{7}Li in Dalton	7.01600455
Polarizability [a.u.]	164

Table E.7: Basis set No. E.7.

Relative motion basis set	
B splines	
Number	160
Order	8
Knot sequence	30.50 (linear+geometric)
Spherical harmonics	
l_{max}	60
m_{max}	0
Center-of-mass motion basis set	
B splines	
Number	100
Order	8
Knot sequence	linear
Spherical harmonics	
L_{MAX}	60
M_{MAX}	0
Box size and atomic specification	
Box size [a.u.]	$\sqrt{12} \cdot 15000$
Mass of ^{7}Li in Dalton	7.01600455
Polarizability [a.u.]	164
Configuration interaction	
Relative motion active orbitals	
Number of bound states	1
Total number of states	100
Symmetry	a_{g}
Center-of-mass active orbitals	
A_g symmetry	41

Table E.8: Basis set No. E.8.

Relative motion basis set	
B splines	
Number	180
Order	8
Knot sequence	30.50 (linear+geometric)
Spherical harmonics	
l_{max}	70
m_{max}	2
Center-of-mass motion basis set	
B splines	
Number	100
Order	8
Knot sequence	linear
Spherical harmonics	
L_{MAX}	70
M_{MAX}	2
Box size and atomic specification	
Box size [a.u.]	$\sqrt{12} \cdot 15000$
Mass of ^{7}Li in Dalton	7.01600455
Polarizability [a.u.]	164
Configuration interaction	
Relative motion active orbitals	
Number of bound states	1
Total number of states	256
Symmetry	a_{g}
Center-of-mass active orbitals	
A_g symmetry	240

Table E.9: Basis set No. E.9.

Relative motion basis set	
B splines	
Number	160
Order	8
Knot sequence	30.50 (linear+geometric)
Spherical harmonics	
l_{max}	60
m_{max}	2
Center-of-mass motion basis set	
B splines	
Number	100
Order	8
Knot sequence	linear
Spherical harmonics	
L_{MAX}	60
M_{MAX}	2
Box size and atomic specification	
Box size [a.u.]	$\sqrt{12} \cdot 15000$
Mass of ^{7}Li in Dalton	7.01600455
Polarizability [a.u.]	164
Configuration interaction	
Relative motion active orbitals	
Number of bound states	1
Total number of states	176
Symmetry	a_{g}
Center-of-mass active orbitals	
A_g symmetry	160

Table E.10: Basis set No. E.10.

Relative motion basis set	
B splines	
Number	120
Order	8
Knot sequence	15.50 (linear+geometric)
Spherical harmonics	
l_{max}	50
m_{max}	2
Center-of-mass motion basis set	
B splines	
Number	80
Order	8
Knot sequence	linear
Spherical harmonics	
L_{MAX}	50
M_{MAX}	2
Box size and atomic specification	
Box size [a.u.]	$\sqrt{12} \cdot 15000$
Mass of ^{7}Li in Dalton	7.01600455
Polarizability [a.u.]	164
Configuration interaction	
Relative motion active orbitals	
Number of bound states	1
Total number of states	256
Symmetry	a_{g}
Center-of-mass active orbitals	
A_g symmetry	240

Table E.11: Basis set No. E.11.

Abbreviations

AMO	Arbeitsgruppe Moderne Optik
a.u.	Atomic unit
BEC	Bose-Einstein condensate
BO	Born-Oppenheimer
c.m.	Center-of-mass
CI	Configuration interaction
CIR	Confinement-induced resonance
ICIR	Inelastic confinement-induced resonance
IR	Irreducible representation
MC	Multi-channel
OL	Optical lattice
QDT	Quantum defect theory
rel.	Relative motion
RKR	Rydberg-Klein-Rees
SE	Schrödinger equation
SC	Single-channel
TISE	Time-independent Schrödinger equation
TIR	Trap-induced resonance

List of Figures

List of Tables

Bibliography

[1] M. H. Anderson, J. R. Ensher, M. R. Matthews, C. E. Wieman, and E. A. Cornell. Observation of Bose-Einstein condensation in a dilute atomic vapor. *Science*, 269:198, 1995.

[2] K. B. Davis, M. O. Mewes, M. R. Andrews, N. J. van Druten, D. S. Durfee, D. M. Kurn, and W. Ketterle. Bose-Einstein condensation in a gas of sodium atoms. *Phys. Rev. Lett.*, 75:3969, 1995.

[3] B. DeMarco and D. S. Jin. Onset of Fermi Degeneracy in a Trapped Atomic Gas. *Science*, 285(5434):1703, 1999.

[4] Cheng Chin, Rudolf Grimm, Paul Julienne, and Eite Tiesinga. Feshbach resonances in ultracold gases. *Rev. Mod. Phys.*, 82:1225, 2010.

[5] Ren Zhang, Yanting Cheng, Hui Zhai, and Peng Zhang. Orbital Feshbach Resonance in Alkali-Earth Atoms. *Phys. Rev. Lett.*, 115:135301, 2015.

[6] G. Pagano, M. Mancini, G. Cappellini, L. Livi, C. Sias, J. Catani, M. Inguscio, and L. Fallani. Strongly Interacting Gas of Two-Electron Fermions at an Orbital Feshbach Resonance. *Phys. Rev. Lett.*, 115:265301, 2015.

[7] M. Höfer, L. Riegger, F. Scazza, C. Hofrichter, D. R. Fernandes, M. M. Parish, J. Levinsen, I. Bloch, and S. Fölling. Observation of an Orbital Interaction-Induced Feshbach Resonance in ^{173}Yb. *Phys. Rev. Lett.*, 115: 265302, 2015.

[8] D. Jaksch, C. Bruder, J. I. Cirac, C. W. Gardiner, and P. Zoller. Cold Bosonic atoms in optical lattices. *Phys. Rev. Lett.*, 81:3108, 1998.

[9] M. Greiner, O. Mandel, T. Esslinger, T.W. Hänsch, and I. Bloch. Exploring phase coherence in a 2D lattice of Bose-Einstein condensates. *Phys. Rev. Lett.*, 87:160405, 2002.

[10] Immanuel Bloch. Ultracold quantum gases in optical lattices. *Nat. Phys.*, 1:23, 2005.

[11] Ivan Kozyryev, Louis Baum, Kyle Matsuda, Benjamin L. Augenbraun, Loic Anderegg, Alexander P. Sedlack, and John M. Doyle. Sisyphus Laser Cooling of a Polyatomic Molecule. *Phys. Rev. Lett.*, 118:173201, 2017.

[12] Mahdi Hosseini, Yiheng Duan, Kristin M. Beck, Yu-Ting Chen, and Vladan Vuletić. Cavity Cooling of Many Atoms. *Phys. Rev. Lett.*, 118: 183601, 2017.

[13] H. P. Büchler, E. Demler, M. Lukin, A. Micheli, N. Prokof'ev, G. Pupillo, and P. Zoller. Strongly Correlated 2D Quantum Phases with Cold Polar Molecules: Controlling the Shape of the Interaction Potential. *Phys. Rev. Lett.*, 98:060404, 2007.

[14] Immanuel Bloch, Jean Dalibard, and Wilhelm Zwerger. Many-body physics with ultracold gases. *Rev. Mod. Phys.*, 80:885, 2008.

[15] M. L. Wall and L. D. Carr. Hyperfine molecular Hubbard Hamiltonian. *Phys. Rev. A*, 82:013611, 2010.

[16] Alexey V. Gorshkov, Salvatore R. Manmana, Gang Chen, Jun Ye, Eugene Demler, Mikhail D. Lukin, and Ana Maria Rey. Tunable Superfluidity and Quantum Magnetism with Ultracold Polar Molecules. *Phys. Rev. Lett.*, 107:115301, 2011.

[17] G. Wilpers, T. Binnewies, C. Degenhardt, U. Sterr, J. Helmcke, and F. Riehle. Optical Clock with Ultracold Neutral Atoms. *Phys. Rev. Lett.*, 89: 230801, 2002.

[18] Masao Takamoto, Feng-Lei Hong, Ryoichi Higashi, and Hidetoshi Katori. An optical lattice clock. *Nature*, 435:321, 2005.

[19] P. S. Jessen, D. L. Haycock, G. Klose, and G. A. Smith. Quantum control and information processing in optical lattices. *Quant. Inf. Comp*, 1:20, 2001.

[20] A. Micheli, G. K. Brennen, and P. Zoller. A toolbox for lattice-spin models with polar molecules. *Nat. Phys.*, 2:341, 2006.

[21] P. Rabl, D. DeMille, J. M. Doyle, M. D. Lukin, R. J. Schoelkopf, and P. Zoller. Hybrid quantum processors: Molecular ensembles as quantum memory for solid state circuits. *Phys. Rev. Lett.*, 97:033003, 2006.

[22] Philipp-Immanuel Schneider and Alejandro Saenz. Quantum computation with ultracold atoms in a driven optical lattice. *Phys. Rev. A*, 85:050304, 2012.

[23] D. Jaksch and P. Zoller. The cold atom hubbard toolbox. *Ann. of Phys.*, 315:52, 2005.

[24] Jonathan Simon, Waseem S. Bakr, Ruichao Ma, M. Eric Tai, Philipp M. Preiss, and Markus Greiner. Quantum simulation of antiferromagnetic spin chains in an optical lattice. *Nature*, 472:307, 2011.

[25] Simon Sala, Johann Förster, and Alejandro Saenz. Ultracold-atom quantum simulator for attosecond science. *Phys. Rev. A*, 95:011403, 2017.

[26] Artur Widera, Olaf Mandel, Markus Greiner, Susanne Kreim, Theodor W. Hänsch, and Immanuel Bloch. Entanglement interferometry for precision measurement of atomic scattering properties. *Phys. Rev. Lett.*, 92:160406, 2004.

[27] T. Zelevinsky, S. Kotochigova, and Jun Ye. Precision test of mass-ratio variations with lattice-confined ultracold molecules. *Phys. Rev. Lett.*, 100: 043201, 2008.

[28] M de Angelis, A. Bertoldi, L. Cacciapuoti, A. Giorgini, G. Lamporesi, M. Prevedelli, G. Saccorotti, F. Sorrentino and G. M. Tino. Precision gravimetry with atomic sensors. *Measurement Science and Technology*, 20(2):022001, 2009.

[29] D. Leibfried, R. Blatt, C. Monroe, and D. Wineland. Quantum dynamics of single trapped ions. *Rev. Mod. Phys.*, 75:281, 2003.

[30] Rainer Blatt and David Wineland. Entangled states of trapped atomic ions. *Nature*, 453:1008, 2008.

[31] J. I. Cirac and P. Zoller. Quantum Computations with Cold Trapped Ions. *Phys. Rev. Lett.*, 74:4091, 1995.

[32] Anders Sørensen and Klaus Mølmer. Entanglement and quantum computation with ions in thermal motion. *Phys. Rev. A*, 62:022311, 2000.

[33] Michael Johanning, Andrés F Varón, and Christof Wunderlich. Quantum simulations with cold trapped ions. *J. Phys. B: At. Mol. Opt. Phys.*, 42 (15):154009, 2009.

[34] B. P. Lanyon, C. Hempel, D. Nigg, M. Müller, R. Gerritsma, F. Zähringer, P. Schindler, J. T. Barreiro, M. Rambach, G. Kirchmair, M. Hennrich, P. Zoller, R. Blatt, C. F. Roos. Universal Digital Quantum Simulation with Trapped Ions. *Science*, 334(6052):57, 2011.

[35] R. Blatt and C. F. Roos. Quantum simulations with trapped ions. *Nature Physics*, 8:277, 2012.

[36] N. Huntemann, C. Sanner, B. Lipphardt, Chr. Tamm, and E. Peik. Single-Ion Atomic Clock with 3×10^{-18} Systematic Uncertainty. *Phys. Rev. Lett.*, 116:063001, 2016.

[37] J. I. Cirac and P. Zoller P. Zoller. A scalable quantum computer with ions in an array of microtraps. *Nature*, 404:579, 2000.

[38] D. Kielpinski, C. Monroe and D. J. Wineland. Architecture for a large-scale ion-trap quantum computer. *Nature*, 417:709, 2002.

[39] R. Côté and A. Dalgarno. Ultracold atom-ion collisions. *Phys. Rev. A*, 62: 012709, 2000.

[40] Robin Côté. From Classical Mobility to Hopping Conductivity: Charge Hopping in an Ultracold Gas. *Phys. Rev. Lett.*, 85:5316, 2000.

[41] Oleg P. Makarov, R. Côté, H. Michels, and W. W. Smith. Radiative charge-transfer lifetime of the excited state of $(\mathrm{NaCa})^+$. *Phys. Rev. A*, 67: 042705, 2003.

[42] Winthrop W. Smith, Oleg P. Makarov, and Jian Lin. Cold ion-neutral collisions in a hybrid trap. *J. Mod. Opt.*, 52(16):2253, 2005.

[43] Andrew T. Grier, Marko Cetina, Fedja Oručević, and Vladan Vuletić. Observation of Cold Collisions between Trapped Ions and Trapped Atoms. *Phys. Rev. Lett.*, 102:223201, 2009.

[44] A. Härter and J. Hecker Denschlag. Cold atom-ion experiments in hybrid traps. *Contemporary Physics*, 55:33, 2014.

[45] Robin Côté. Chapter Two - Ultracold Hybrid Atom-Ion Systems. volume 65 of *Advances In Atomic, Molecular, and Optical Physics*, pages 67–126. Academic Press, 2016.

[46] Zbigniew Idziaszek, Tommaso Calarco, Paul S. Julienne, and Andrea Simoni. Quantum theory of ultracold atom-ion collisions. *Phys. Rev. A*, 79:010702(R), 2009.

[47] Humberto da Silva Jr, Maurice Raoult, Mireille Aymar and Olivier Dulieu. Formation of molecular ions by radiative association of cold trapped atoms and ions. *New J. Phys.*, 17:045015, 2015.

[48] Michał Krych, Wojciech Skomorowski, Filip Pawłowski, Robert Moszynski, and Zbigniew Idziaszek. Sympathetic cooling of the Ba^+ ion by collisions with ultracold Rb atoms: Theoretical prospects. *Phys. Rev. A*, 83:032723, 2011.

[49] Christoph Zipkes, Stefan Palzer, Carlo Sias, and Michael Köhl. A trapped single ion inside a Bose-Einstein condensate. *Nature*, 464:388, 2010.

[50] Christoph Zipkes, Stefan Palzer, Lothar Ratschbacher, Carlo Sias, and Michael Köhl. Cold Heteronuclear Atom-Ion Collisions. *Phys. Rev. Lett.*, 105:133201, 2010.

[51] Christoph Zipkes, Lothar Ratschbacher, Stefan Palzer, Carlo Sias and Michael Köhl. Hybrid quantum systems of atoms and ions. *J. Phys. Conf. Ser.*, 264:012019, 2011.

[52] Arne Härter, Artjom Krükow, Andreas Brunner, Wolfgang Schnitzler, Stefan Schmid, and Johannes Hecker Denschlag. Single Ion as a Three-Body Reaction Center in an Ultracold Atomic Gas. *Phys. Rev. Lett.*, 109: 123201, 2012.

[53] R. Gerritsma, A. Negretti, H. Doerk, Z. Idziaszek, T. Calarco, and F. Schmidt-Kaler. Bosonic Josephson Junction Controlled by a Single Trapped Ion. *Phys. Rev. Lett.*, 109:080402, 2012.

[54] U. Bissbort, D. Cocks, A. Negretti, Z. Idziaszek, T. Calarco, F. Schmidt-Kaler, W. Hofstetter, and R. Gerritsma. Emulating Solid-State Physics with a Hybrid System of Ultracold Ions and Atoms. *Phys. Rev. Lett.*, 111: 080501, 2013.

[55] J. Joger, A. Negretti, and R. Gerritsma. Quantum dynamics of an atomic double-well system interacting with a trapped ion. *Phys. Rev. A*, 89: 063621, 2014.

[56] Hauke Doerk, Zbigniew Idziaszek, and Tommaso Calarco. Atom-ion quantum gate. *Phys. Rev. A*, 81:012708, 2010.

[57] Corinna Kollath, Michael Köhl, and Thierry Giamarchi. Scanning tunneling microscopy for ultracold atoms. *Phys. Rev. A*, 76:063602, 2007.

[58] Stefan Schmid, Arne Härter, and Johannes Hecker Denschlag. Dynamics of a Cold Trapped Ion in a Bose-Einstein Condensate. *Phys. Rev. Lett.*, 105:133202, 2010.

[59] Felix H. J. Hall and Stefan Willitsch. Millikelvin Reactive Collisions between Sympathetically Cooled Molecular Ions and Laser-Cooled Atoms in an Ion-Atom Hybrid Trap. *Phys. Rev. Lett.*, 109:233202, 2012.

[60] P. C. Stancil, S. Lepp, and A. Dalgarno. The Lithium Chemistry of the Early Universe. *Astrophys. J.*, 458:401, 1996.

[61] Felix H.J. Hall, Pascal Eberle, Gregor Hegi, Maurice Raoult, Mireille Aymar, Olivier Dulieu, and Stefan Willitsch. Ion-neutral chemistry at ultralow energies: dynamics of reactive collisions between laser-cooled Ca^+ ions and Rb atoms in an ion-atom hybrid trap. *Mol. Phys.*, 111: 2020, 2013.

[62] M. G. Raizen, J. M. Gilligan, J. C. Bergquist, W. M. Itano, and D. J. Wineland. Ionic crystals in a linear Paul trap. *Phys. Rev. A*, 45:6493, 1992.

[63] D. J. Berkeland, J. D. Miller, J. C. Bergquist, W. M. Itano, and D. J. Wineland. Minimization of ion micromotion in a Paul trap. *J. Appl. Phys.*, 83:5025, 1998.

[64] R Schmied, T Roscilde, V Murg, D Porras and J I Cirac. Quantum phases of trapped ions in an optical lattice. *New J. Phys.*, 10:045017, 2008.

[65] Ch. Schneider, M. Enderlein, T. Huber, and T. Schaetz. Optical trapping of an ion. *Nature Photonics*, 4:772, 2010.

[66] Martin Enderlein, Thomas Huber, Christian Schneider, and Tobias Schaetz. Single Ions Trapped in a One-Dimensional Optical Lattice. *Phys. Rev. Lett.*, 109:233004, 2012.

[67] Rasmus B. Linnet, Ian D. Leroux, Mathieu Marciante, Aurélien Dantan, and Michael Drewsen. Pinning an Ion with an Intracavity Optical Lattice. *Phys. Rev. Lett.*, 109:233005, 2012.

[68] Leon Karpa, Alexei Bylinskii, Dorian Gangloff, Marko Cetina, and Vladan Vuletić. Suppression of Ion Transport due to Long-Lived Subwavelength Localization by an Optical Lattice. *Phys. Rev. Lett.*, 111:163002, 2013.

[69] Christoph Zipkes, Lothar Ratschbacher, Carlo Sias, and Michael Köhl. Kinetics of a single trapped ion in an ultracold buffer gas. *New J. Phys.*, 13(5):053020, 2011.

[70] Marko Cetina, Andrew T. Grier, and Vladan Vuletić. Micromotion-Induced Limit to Atom-Ion Sympathetic Cooling in Paul Traps. *Phys. Rev. Lett.*, 109:253201, 2012.

[71] Ziv Meir, Tomas Sikorsky, Ruti Ben-shlomi, Nitzan Akerman, Yehonatan Dallal, and Roee Ozeri. Dynamics of a Ground-State Cooled Ion Colliding with Ultracold Atoms. *Phys. Rev. Lett.*, 117:243401, 2016.

[72] Zbigniew Idziaszek, Tommaso Calarco, and Peter Zoller. Controlled collisions of a single atom and an ion guided by movable trapping potentials. *Phys. Rev. A*, 76:033409, 2007.

[73] Sergey Grishkevich, Simon Sala, and Alejandro Saenz. Theoretical description of two ultracold atoms in finite three-dimensional optical lattices using realistic interatomic interaction potentials. *Phys. Rev. A*, 84:062710, 2011.

[74] Nobuhiro Yamanaka. Calculation of mass polarization for the $1s^2 2s\ ^2S$ and $1s^2 2p\ ^2P$ states in Li-like ions. *J. Phys. B: At. Mol. Opt. Phys.*, 32 (6):1597, 1999.

[75] John C. Tully. Diatomics-in-molecules potential energy surfaces. II. Nonadiabatic and spin-orbit interactions. *J. Chem. Phys*, 59(9):5122, 1973.

[76] T. G. Heil, S. E. Butler, and A. Dalgarno. Charge transfer of multiply charged ions at thermal energies. *Phys. Rev. A*, 23:1100, 1981.

[77] Frank J. Zeleznik. Numerical Calculation of Potential-Energy Curves by the Rydberg-Klein-Rees Method. *J. Chem. Phys.*, 42(8):2836, 1965.

[78] Yulian V. Vanne and Alejandro Saenz. Numerical treatment of diatomic two-electron molecules using a B-spline based CI method. *J. Phys. B: At. Mol. Opt. Phys.*, 37(20):4101, 2004.

[79] I. Dumitriu, Y. V. Vanne, M. Awasthi, and A. Saenz. Photoionization of the alkali dimer cations Li_2^+, Na_2^+, and $LiNa^+$. *J. Phys. B*, 40:1821, 2007.

[80] A. R. Janzen and R. A. Aziz. An accurate potential energy curve for helium based on ab initio calculations. *The Journal of Chemical Physics*, 107(3):914, 1997.

[81] F. Bouchelaghem and M. Bouledroua. Quantum effects in the case of $^6Li^+$ and $^7Li^+$ ions evolving in a neutral ^6Li gas at a wide range of temperatures. *Phys. Chem. Chem. Phys.*, 16:1875, 2014.

[82] Rudolf Grimm, Matthias Weidemüller and Yurii B. Ovchinnikov. Optical Dipole Traps for Neutral Atoms. *Adv. At. Mol. Opt. Phys.*, 42:95, 2000.

[83] Claude Cohen-Tannoudji, Bernard Diu and Frank Laloë. *Quantum Mechanics*, volume 2. Wiley, New York, 1977.

[84] J. J. Sakurai. *Modern Quantum Mechanics*. Addison Wesley, Second edition, 1994.

[85] Vladimir V. Meshkov, Andrey V. Stolyarov and Robert J. Le Roy. Rapid, accurate calculation of the s-wave scattering length. *J. Chem. Phys.*, 135 (15):154108, 2011.

[86] John Weiner, Vanderlei S. Bagnato, Sergio Zilio, and Paul S. Julienne. Experiments and theory in cold and ultracold collisions. *Rev. Mod. Phys.*, 71:1, 1999.

[87] Claude Cohen-Tannoudji and David Guéry-Odelin. *Advances in Atomic Physics: An Overview*. World Scientific Publishing, Singapore, 2011.

[88] G. F. Gribakin and V. V. Flambaum. Calculation of the scattering length in atomic collisions using the semiclassical approximation. *Phys. Rev. A*, 48:546, 1993.

[89] V. V. Flambaum, G. F. Gribakin, and C. Harabati. Analytical calculation of cold-atom scattering. *Phys. Rev. A*, 59:1998, 1999.

[90] Boris Mikhailovich Karnakov and Vladimir Pavlovich Krainov. *WKB Approximation in Atomic Physics*. Springer-Verlag Berlin Heidelberg, 2013.

[91] Enrico Fermi. *Ric. Sci.*, 7:13, 1936.

[92] Kerson Huang and C. N. Yang. Quantum-Mechanical Many-Body Problem with Hard-Sphere Interaction. *Phys. Rev.*, 105:767, 1957.

[93] Thomas Busch, Berthold-Georg Englert, Kazimierz Rzazewski, and Martin Wilkens. Two cold atoms in a harmonic trap. *Found. Phys.*, 28:549, 1998.

[94] Z. Idziaszek and T. Calarco. Two atoms in an anisotropic harmonic trap. *Phys. Rev. A*, 71:050701(R), 2005.

[95] Zbigniew Idziaszek and Tommaso Calarco. Analytical solutions for the dynamics of two trapped interacting ultracold atoms. *Phys. Rev. A*, 74: 022712, 2006.

[96] Jun-Jun Liang and Chao Zhang. Two ultracold atoms in a completely anisotropic trap. *Phys. Scr.*, 77:025302, 2008.

[97] Shi-Guo Peng, Seyyed S. Bohloul, Xia-Ji Liu, Hui Hu, and Peter D. Drummond. Confinement-induced resonance in quasi-one-dimensional systems under transversely anisotropic confinement. *Phys. Rev. A*, 82: 063633, 2010.

[98] A. J. Moerdijk, B. J. Verhaar, and A. Axelsson. Resonances in ultracold collisions of ^{6}Li, ^{7}Li, and ^{23}Na. *Phys. Rev. A*, 51:4852, 1995.

[99] W. Ketterle and M. W. Zwierlein. Making, probing and understanding ultracold Fermi gases, in Ultracold Fermi Gases. Proceedings of the International School of Physics "Enrico Fermi" Course CLXIV, Varenna, 20 - 30 June 2006. IOS Press, Amsterdam, 2008. Edited by M. Inguscio, W. Ketterle, and C. Salomon.

[100] Sergey Grishkevich, Philipp-Immanuel Schneider, Yulian V. Vanne, and Alejandro Saenz. Mimicking multichannel scattering with single-channel approaches. *Phys. Rev. A*, 81:022719, 2010.

[101] M J Seaton and L Steenman-Clark. Effective potentials for electron-atom scattering below inelastic thresholds. II. Asymptotic forms. *J. Phys. B: At. Mol. Phys.*, 10(13):2639, 1977.

[102] Bo Gao. Universal Properties in Ultracold Ion-Atom Interactions. *Phys. Rev. Lett.*, 104:213201, 2010.

[103] Michał Krych and Zbigniew Idziaszek. Controlled collisions of two ultracold atoms in separate harmonic traps. *Phys. Rev. A*, 80:022710, 2009.

[104] Chris H. Greene, A. R. P. Rau, and U. Fano. General form of the quantum-defect theory. II. *Phys. Rev. A*, 26:2441, 1982.

[105] M J Seaton. Quantum defect theory. *Reports Prog. Phys.*, 46(2):167, 1983.

[106] Frederick H. Mies. A multichannel quantum defect analysis of diatomic predissociation and inelastic atomic scattering. *J. Chem. Phys.*, 80(6): 2514, 1984.

[107] James F. E. Croft, Alisdair O. G. Wallis, Jeremy M. Hutson, and Paul S. Julienne. Multichannel quantum defect theory for cold molecular collisions. *Phys. Rev. A*, 84:042703, 2011.

[108] Zbigniew Idziaszek, Andrea Simoni, Tommaso Calarco and Paul S Julienne. Multichannel quantum-defect theory for ultracold atom-ion collisions. *New J. Phys.*, 13:083005, 2011.

[109] Bo Gao. Quantum-defect theory for $-1/r^4$-type interactions. *Phys. Rev. A*, 88:022701, 2013.

[110] Ming Li, Li You, and Bo Gao. Multichannel quantum-defect theory for ion-atom interactions. *Phys. Rev. A*, 89:052704(R), 2014.

[111] Bo Gao. Angular-momentum-insensitive quantum-defect theory for diatomic systems. *Phys. Rev. A*, 64:010701(R), 2001.

[112] Sergey Grishkevich and Alejandro Saenz. Exact Theoretical Description of Two Ultracold Atoms in 3D Optical Lattices. In *Journal of Physics: Conference Series*, volume 88, page 012042, 2007.

[113] Sergey Grishkevich and Alejandro Saenz. Theoretical description of two ultracold atoms in a single site of a three-dimensional optical lattice using realistic interatomic interaction potentials. *Phys. Rev. A*, 80:013403, 2009.

[114] Bruno Schulz. Ultrakalte dipolare Quantengase in externen Fallen. Master's thesis, Humboldt-Universität zu Berlin, 2015.

[115] David J. Willock. *Molecular Symmetry.* John Wiley & Sons Ltd, 2009.

[116] René Stock, Ivan H. Deutsch, and Eric L. Bolda. Quantum State Control via Trap-Induced Shape Resonance in Ultracold Atomic Collisions. *Phys. Rev. Lett.*, 91:183201, 2003.

[117] Carsten Robens, Jonathan Zopes, Wolfgang Alt, Stefan Brakhane, Dieter Meschede, and Andrea Alberti. Low-Entropy States of Neutral Atoms in Polarization-Synthesized Optical Lattices. *Phys. Rev. Lett.*, 118:065302, 2017.

[118] D. S. Weiss, J. Vala, A. V. Thapliyal, S. Myrgren, U. Vazirani, and K. B. Whaley. Another way to approach zero entropy for a finite system of atoms. *Phys. Rev. A*, 70:040302, 2004.

[119] Moncef Bouledroua. Private Communication. December, 2016.

[120] S. Magnier, S. Rousseau, A.R. Allouche, G. Hadinger and M. Aubert-Frécon. Potential energy curves of 58 states of Li_2^+. *Chem. Phys.*, 246:57, 1999.

[121] Tony C Scott, Monique Aubert-Frécon, Gisèle Hadinger, Dirk Andrae, Johannes Grotendorst, and John D Morgan III. Asymptotically exact calculation of the exchange energies of one-active-electron diatomic ions with the surface integral method. *J. Phys. B: At. Mol. Opt. Phys.*, 37 (22):4451, 2004.

[122] Peng Zhang, Enrico Bodo, and Alexander Dalgarno. Near Resonance Charge Exchange in Ion-Atom Collisions of Lithium Isotopes. *J. Phys. Chem. A*, 113:15085, 2009.

[123] Daniel D. Konowalow and Marcy E. Rosenkrantz. Ab initio calculations of the electronic structure and the vibrational spectra of the $\mathrm{X}^2\Sigma_g^+$, $^2\Sigma_u^+$, $\mathrm{A}^2\Pi_u$ and $^2\Pi_g$ states of Li_2^+. *Chem. Phys. Lett.*, 61:489, 1979.

[124] René Stock and Ivan H. Deutsch. Trap-induced resonances in controlled collisions of cesium atoms. *Phys. Rev. A*, 73:032701, 2006.

[125] Simon Sala, Philipp-Immanuel Schneider, and Alejandro Saenz. Inelastic confinement-induced resonances in low-dimensional quantum systems. *Phys. Rev. Lett.*, 109:073201, 2012.

[126] S. Sala, G. Zürn, T. Lompe, A. N. Wenz, S. Murmann, F. Serwane, S. Jochim, and A. Saenz. Coherent molecule formation in anharmonic potentials near confinement-induced resonances. *Phys. Rev. Lett.*, 110: 203202, 2013.

[127] B. Schulz, S. Sala, and A. Saenz. Resonances in ultracold dipolar atomic and molecular gases. *New J. Phys.*, 17:065002, 2015.

[128] M. Troppenz, S. Sala, P.-I. Schneider, and A. Saenz. Inelastic confinement-induced resonances in quantum dots, 2015. arXiv:1509.01159.

[129] Simon Sala and Alejandro Saenz. Theory of inelastic confinement-induced resonances due to the coupling of center-of-mass and relative motion. *Phys. Rev. A*, 94:022713, 2016.

[130] M. Olshanii. Atomic scattering in the presence of an external confinement and gas of impenetrable Bosons. *Phys. Rev. Lett.*, 81:938, 1998.

[131] Lewi Tonks. The complete equation of state of one, two and three-dimensional gases of hard elastic spheres. *Phys. Rev.*, 50:955, 1936.

[132] M. Girardeau. Relationship between systems of impenetrable bosons and fermions in one dimension. *J. Math. Phys.*, 1:516, 1960.

[133] Belén Paredes, Artur Widera, Valentin Murg, Olaf Mandel, Simon Fölling, Ignacio Cirac, Gora V. Shlyapnikov, Theodor W. Hänsch, and Immanuel Bloch. Tonks-Girardeau gas of ultracold atoms in an optical lattice. *Nature*, 429:277, 2004.

[134] Toshiya Kinoshita, Trevor Wenger, and David S. Weiss. Observation of a One-Dimensional Tonks-Girardeau Gas. *Science*, 305:1125, 2004.

[135] E. Haller, M. Gustavsson, M. J. Mark, J. G. Danzl, R. Hart, G. Pupillo, and H.-C. Nägerl. Realization of an Excited, Strongly Correlated Quantum Gas Phase. *Science*, 325:1224, 2009.

[136] T. Bergeman, M. G. Moore, and M. Olshanii. Atom-atom scattering under cylindrical harmonic confinement: Numerical and analytic studies of the confinement induced resonance. *Phys. Rev. Lett.*, 91:163201, 2003.

[137] D. S. Petrov, M. Holzmann, and G. V. Shlyapnikov. Bose-Einstein condensation in quasi-2d trapped gases. *Phys. Rev. Lett.*, 84:2551, 2000.

[138] K. Günter, T. Stöferle, H. Moritz, M. Köhl, and T. Esslinger. p-wave interactions in low-dimentional Fermionic gases. *Phys. Rev. Lett.*, 95: 230401, 2005.

[139] V. S. Melezhik and A. Negretti. Confinement-induced resonances in ultracold atom-ion systems. *Phys. Rev. A*, 94:022704, 2016.

[140] Elmar Haller, Manfred J. Mark, Russell Hart, Johann G. Danzl, Lukas Reichsöllner, Vladimir Melezhik, Peter Schmelcher, and Hanns-Christoph Nägerl. Confinement-induced resonances in low-dimensional quantum systems. *Phys. Rev. Lett.*, 104:153203, 2010.

[141] Bernd Fröhlich, Michael Feld, Enrico Vogt, Marco Koschorreck, Wilhelm Zwerger, and Michael Köhl. Radio-Frequency Spectroscopy of a Strongly Interacting Two-Dimensional Fermi Gas. *Phys. Rev. Lett.*, 106:105301, 2011.

[142] Pascal Naidon, Eite Tiesinga, William F. Mitchell, and Paul S. Julienne. Effective-range description of a bose gas under strong one- or two-dimensional confinement. *New J. Phys.*, 9:19, 2007.

[143] Simon Johannes Sala. *Ultracold Atoms in Traps: Theoretical Approaches, Resonances, and Quantum Simulations.* PhD thesis, Humboldt-Universität zu Berlin, Mathematisch-Naturwissenschaftliche Fakultät, 2016.

[144] F. Deuretzbacher, K. Plassmeier, D. Pfannkuche, F. Werner, C. Ospelkaus, S. Ospelkaus, K. Sengstock, and K. Bongs. Heteronuclear molecules in an optical lattice: Theory and experiment. *Phys. Rev. A*, 77:032726, 2008.

[145] Bertelsen, Jesper Fevre and Mølmer, Klaus. Association of heteronuclear molecules in a harmonic oscillator well. *Phys. Rev. A*, 76:043615, 2007.

[146] P.-I. Schneider, S. Grishkevich, and A. Saenz. Non-perturbative theoretical description of two atoms in an optical lattice with time-dependent perturbations. *Phys. Rev. A*, 87:053413, 2013.

[147] A. K. Bhatia and A. Temkin. Decomposition of the Schrödinger Equation for Two Identical Particles and a Third Particle of Finite Mass. *Phys. Rev.*, 137:A1335, 1965.

[148] I.S. Gradshteyn and I.M. Ryzhik. *Table of Integrals, Series, and Products.* Academic Press, 2007.

[149] J. Rasch and A. C. H. Yu. Efficient storage scheme for precalculated Wigner $3j$, $6j$ and Gaunt coefficients. *SIAM J. Sci. Comput.*, 25:1416, 2003.

[150] Didier Pinchon and Philip E. Hoggan. New index functions for storing Gaunt coefficients. *Int. J. Quant. Chem.*, 107:2186, 2007.

Erklärung

Hiermit erkläre ich, die Dissertation selbstständig und nur unter Verwendung der angegebenen Hilfen und Hilfsmittel angefertigt zu haben. Ich habe mich nicht anderwärts um einen Doktorgrad in dem Promotionsfach beworben und besitze keinen entsprechenden Doktorgrad. Die Promotionsordnung der Mathematisch-Naturwissenschaftlichen Fakultät, veröffentlicht im Amtlichen Mitteilungsblatt der Humboldt-Universität zu Berlin Nr. 126/2014 am 18.11.2014, habe ich zur Kenntnis genommen.

Berlin, 03. August 2017 ....

Onyango Stephen Okeyo

Acknowledgment

First, I would like to express my deepest gratitude and special appreciation to my supervisor Prof. Dr. Alejandro Saenz who has supported me during the entire study. I would like to thank you for the guidance, constructive criticism, encouragement and the mentorship. You were very patient with me especially at times when my progress was slow. I am also very thankful for the financial support you offered me during the last months of the study. I will forever remain indebted to you for the life-time opportunity.

Second, I am truly grateful to have met Dr. Fabio Revuelta during the first few months of the research. I do not have a better way to express my appreciation to you because words cannot express how grateful I am. Your insightful comments, the tremendous advice, were very helpful during various stages of my research. You are my role model, mentor, and above all, a good friend. Thank you very much.

A heartfelt thanks to all members of AMO group members more so Dr. Simon Sala and Bruno Schulz who introduced me to the codes. Sincere gratitude to Alvaro Magaña and Johann Förster for all technical assistance and of course the friendship. To my Kenyan colleague Eric Jobunga, it was nice to have a friend like you. I can't forget to thank all my Kenyan friends in Berlin. You guys made my stay in Berlin enjoyable.

I am also grateful to Dr. Moncef Bouledroua for supplying me with the numerical potential curves.

Very special thanks to the Kenyan and German governments for the PhD scholarship through the joint collaboration of the National Commission for Science, Technology and Innovation (NACOSTI) and the German Academic Exchange Service (DAAD).

Finally, I would like to thank my family: my parents and siblings, I am very happy for the continuous encouragement and unparalleled love especially during the most difficult and dark moments. A special thanks to my dear wife Susan for persevering years of my absence, you have been a source of strength and inspiration, your constant encouragement gave me hope whenever everything seemed hopeless, and more importantly, you have taken good care of our sons Steve Jnr. and Owen Otieno. Thank you.